AN EXPERIMENTAL STUDY OF PASSIVE FLOW SEPARATION CONTROL BY BACKWARD FACING STEP WITH DIFFERENT ASPECT RATIOS OF NACA 0012 WING

By

MAHBUBUR RAHMAN

MASTER OF SCIENCE IN MECHANICAL ENGINEERING

Department of Mechanical Engineering
BANGLADESH UNIVERSITY OF ENGINEERING & TECHNOLOGY

March 2019

AN EXPERIMENTAL STUDY OF PASSIVE FLOW SEPARATION CONTROL BY BACKWARD FACING STEP WITH DIFFERENT ASPECT RATIOS OF NACA 0012 WING

By

MAHBUBUR RAHMAN

A THESIS SUBMITTED TO THE DEPARTMENT OF MECHANICAL ENGINEERING,
BANGLADESH UNIVERSITY OF ENGINEERING AND TECHNOLOGY (BUET) IN
PARTIAL FULFILLMENT OF THE REQUIREMENTS FOR THE DEGREE OF
MASTER OF SCIENCE IN MECHANICAL ENGINEERING

Supervised by

Dr. Mohammad Ali
Professor, Department of Mechanical Engineering

Department of Mechanical Engineering
BANGLADESH UNIVERSITY OF ENGINEERING & TECHNOLOGY

March 2019

DEDICATION

Dedicate this thesis

To my parents;

To my teachers;

The thesis titled "**An Experimental Study of Passive Flow Separation Control by Backward Facing Step with Different Aspect Ratios of NACA 0012 Wing,**" submitted by **Mahbubur Rahman,** Roll: 0416102076 F, Session: April-2016, has been accepted as satisfactory in partial fulfillment of the requirements for the degree of Master of Science in Mechanical Engineering on 23th March 2019.

BOARD OF EXAMINERS

1. ______________________________
Dr. Mohammad Ali — Chairman (Supervisor)
Professor
Department of Mechanical Engineering
BUET, Dhaka-1000, Bangladesh.

2. ______________________________
Dr. Md. Ashraful Islam — Member (Ex-Officio)
Professor & Head
Department of Mechanical Engineering
BUET, Dhaka-1000, Bangladesh.

3. ______________________________
Dr. Mohammad Arif Hasan Mamun — Member
Professor
Department of Mechanical Engineering
BUET, Dhaka-1000, Bangladesh.

4. ______________________________
Dr. Mohammad Mamun — Member
Professor
Department of Mechanical Engineering
BUET, Dhaka-1000, Bangladesh.

5. ______________________________
Dr. Md. Quamrul Islam — Member (External)
Professor
Military Institute of Science & Technology
Mirpur, Dhaka-1216, Bangladesh.

ABSTRACT

The lifting surface may be considered as a tool which develops a useful reaction force during its motion relative to the fluid. The surfaces of wings and tails of airplanes, propellers and blades of turbo-machinery are some of the examples of the lifting surfaces. The production of the maximum possible lift force and that of the minimum possible drag force in directions perpendicular to the direction of motion depends on the optimum design of lifting surface. Aspect ratio is an important technique for the improvement of aerodynamic characteristics through drag reduction. In that present work, the effect of aspect ratio on the airfoil characteristic of NACA 0012 wing is investigated through experiments as a function of angle of attack and also the passive flow separation is controlled by introducing backward facing step to the optimum airfoil. The ability to manipulate a flow passively or actively is of immense technological importance. An interference drag between wing and body also plays an important role on the performance. The magnitudes of aerodynamic forces on airfoils resulting from the incompressible viscous flow fields are determined experimentally. Three wing models of different aspect ratios such as AR=2, AR=1 and AR=0.5 of symmetrical airfoils type NACA 0012, are tested in this experiment, with different angle of attack ranging from 0° to 20° keeping the surface area alike. The aerodynamic characteristics such as coefficient of lift, coefficient of drag and coefficient of lift to drag ratio and coefficient of performance for different models is determined from the static pressure distribution.

After analyzing the data, it is found that the pressure differences between the upper and lower surfaces are higher for wing model of AR 2 than other two models of AR 0.5 and AR 1.It is observed that the critical angle of attack of all the wing models remain around 12^0 beyond which stall occurs but for optimum wing models with backward facing step stall occurs at 14^0. The experimental results also show that wing model with the aspect ratio 2 yields the optimum performance as its lift to drag coefficient ratio is higher than any other models. It is also experimented that by introducing backward facing step the flow separation is controlled at high angle of attack which is required during takeoff, landing and maneuvering.

ACKNOWLEDGEMENT

At first I would like to express my deepest gratitude to the Almighty for the successful completion of this research. My profound respect and sincere gratitude to my supervisor Dr. Mohammad Ali, Professor, Department of Mechanical Engineering, BUET, Dhaka for his continuous guidance, kind supervision, inspiration, encouragement and valuable counselling in the execution and completion of the entire research work.

I would like to express my sincere thanks to Professor Dr. Md. Ashraful Islam, Head, Department of Mechanical Engineering, BUET, Dhaka for providing necessary lab and workshop facilities for the research.

I am highly indebted to Committee for Advanced Studies and Research (CASR), BUET for approving my thesis proposal at meeting no: 311 and providing full fund for completion of the entire research work.

I am also grateful to Professor Dr. Mohammad Arif Hasan Mamun and Professor Dr. Mohammad Mamun, Department of Mechanical Engineering, BUET, Dhaka for their cooperation and suggestions whenever needed. Their valuable comments and reviews were very helpful in making this a complete work.

I would also like to thank all the staffs of Turbulence Laboratory of Department of Mechanical Engineering, BUET for providing assistance during preparation of the experimental setup.

Finally, I am very grateful to my family members and friends who supported and motivated me regarding this thesis work.

DECLERATION

It is hereby declared that this thesis or any part of it has not been submitted elsewhere for the award of any degree or qualification.

Signature of the Candidate:

Mahbubur Rahman

CONTENTS

LIST OF FIGURES

LIST OF TABLES

NOMENCLATURE

A	Axial Force
b	Wing Span
C	Wing Chord
C_a	Axial Force Coefficient
C_D	Coefficient of Drag
C_{di}	Sectional Induced Drag Coefficient
C_L	Coefficient of Lift
C_{pl}	Lower Surface Pressure Coefficient
C_n	Normal Force Coefficient
C_p	Coefficient of Pressure
C_{pu}	Upper Surface Pressure Coefficient
C_{root}	Root Chord
C_{tip}	Tip Chord
$c(y)$	Chord Distribution
D	Drag Force
D_i	Induced Drag Force
L	Lift Force
C_L/C_D	Lift to Drag Coefficient Ratio
M	Model
N	Normal Force
p	Pressure
P_∞	Free Stream Pressure
P_i	Local Static Surface Pressure
q_∞	Dynamic Pressure
r_0	Radius of Curvature at Airfoil’s Leading Edge
R_N	Reynolds Number
S	Wing Surface Area
t_{max}	Maximum Thickness of Aerofoil

V_∞	Free Stream Velocity of Air
AR	Aspect Ratio
AOA	Angle of Attack
BFS	Backward Facing Step
v	Velocity of Air
w	Downwash
x_c	Distance of Maximum Camber
x_t	Distance from the Leading Edge of Aerofoil
z_c	Maximum Camber
α	Angle of Attack
α_a	Absolute Angle of Attack
α_{Lmax}	Stalling Angle of Attack
α_i	Induced Angle of Attack
α_o	Effective Angle of Attack
τ	Shear Stress
ρ_a	Density of Air
ρ_w	Density of Water
μ_a	Absolute Viscosity of Air
μ_w	Absolute Viscosity of Water
Γ	Circulation
$1/2\ pU_\infty^2$	Free Stream Dynamic Pressure

1

Chapter One

INTRODUCTION

1.1 General

When a fluid flowing past the surface of a body exerts a force on it. Lift is the component of this force that is perpendicular to the oncoming flow direction. It contrasts with the drag force, which is the component of the force parallel to the flow direction. Lift is most commonly associated with the wings. There are several ways to explain how an airfoil generates lift. The lifting surface of an immersed body may be defined as a tool which develops a useful reaction force during its motion relative to the fluid. The surfaces of wings and tails of aero planes, propellers and blades of turbomachinary are some of the examples of the lifting surfaces. The optimum design of lifting surface yields the production of the maximum possible lift force and the production of the minimum possible drag force in directions perpendicular to the direction of motion. Aspect ratio is an important technique for the improvement of aerodynamic characteristics through drag reduction. The lift force depends on the shape of the airfoil. Wing is the primary lifting surface of an aircraft which sustains the weight of the aircraft to make flight in the air while from aerodynamics perspective it is also the main source of the aircraft drag. As a result, the effects of wing shape and size are crucial to aerodynamic characteristics on which the efficiency of aircraft depends. As such, researches on different wing shapes and geometries are still on throughout the world to explore the maximum possible lift and minimum possible drag.

The flow over an airfoil is smooth and attached at low angle of attack (α). When α is increased, the co-efficient of lift is increased as the pressure difference between the suction and pressure surface of the airfoil is enhanced. However, after a particular α, known as stalling angle, the flow will not able to withstand the adverse pressure gradient generated over the suction side of the foil and as a result the boundary layer separation will take place. This phenomenon is known as stalling which results in loss of lift, increased drag, and generation of aerodynamic noise. An aircraft is required to operate at high α during takeoff, landing and maneuvering. Hence flow control over an airfoil at high angle of attack is of strong interest. The nature of separated flows due to their instabilities is very complex. To simplify these flow characteristics, researchers conducted experiments on various geometries, which include rib, fence, bluff body with a splitter plate, suddenly expanding pipes, forward and backward-facing steps, cavities and bluff bodies with blunt leading edges. These geometries simplify the flow characteristics to a certain extent by controlling the separation or the reattachment point or both, which are otherwise unsteady. Because of its single fixed separation point and the wake dynamics unperturbed by the downstream disturbances the backward-facing step is considered by most as the ideal canonical separated flow geometry. The present research is focusing on the aerodynamic performance with passive flow separation control introducing backward facing step for different aspect ratios through experiment by using wind-tunnel.

1.2 Background

Aspect ratio which is proportional to the square of the wingspan, is of particular significance in determining the performance for a given wing area. In aerodynamics, the main source of the airplane drag is related with the wing. There are three sources of drag: (i) profile drag which is related to skin friction caused by flow of air over the aircraft surface (ii) induced drag which is the result of lift generation for finite wingspan and (iii) the compressibility drag caused by high speed aerodynamics. To improve the performance of airfoil either lift coefficient must be increased or drag should be decreased and pressure coefficient must be properly distributed on the airfoil surface [1]. The interest for flow control has increased in the aerospace industry as higher performances are pursued and innovative approaches to drag reduction are introduced. Various methods for boundary layer control have been studied in the past decades in order to provoke or delay separation on airfoils. After the discovery of boundary layer theory by Ludwig Prandtl in the early twentieth century was the beginning to the extensive research on separated flows. Separated flows are common in several engineering applications such as aircraft wings, turbine and compressor blades, diffusers, buildings suddenly expanding pipes, combustors, etc. The characteristics of a separated flow have been studied for decades by experimentalists to understand the physics of the separated shear layers and their instability mechanisms [2]. The instabilities in the free shear layers are the source to distinctly visible large coherent structures. The drag stems from the vortices shed by an aircraft's wings, which causes the local relative wind downward (an effect known as downwash) and generate a component of the local lift force in the direction of the free stream. The strength of this induced drag is proportional to the spacing and radii of these vortices. By designing wings, which force the vortices farther apart and at the same time create vortices with larger core radii, may significantly reduce the amount of drag the aircraft induces. Airplanes which experience less drag require less power and therefore less fuel to fly an arbitrary distance, thus making flight more efficient and less costly. So, reduction of drag and flow separation control of a wing plays an important role to make the flight safe, smooth, effective and less costly.

1.3 Motivation of the Research Work

Literature review as discussed in chapter-2 reveals that several researches on airfoil to control flow separation have been carried out both numerically and experimentally. Still the aerodynamic performances of symmetric airfoil (NACA 0012) with passive flow separation control for different aspect ratios are yet to be explored experimentally. For this, an effort has been taken to investigate the aerodynamic performance with passive flow separation control for different aspect ratios through experiment by using wind-tunnel.

1.4 Scope and Objectives of the Research

The proposed experimental investigation is carried out in the wind tunnel to make a comparative study among three different aspect ratios (AR 2, AR 1 and AR 0.5) of NACA 0012 wing. After analyzing the results, the optimum configuration will be found out. Then the passive flow separation will be controlled on the optimum airfoil wing introducing backward facing step. At the end, the aerodynamic characteristics of airfoils with passive flow separation control will be analyzed. So, the specific objectives are as follows:

i) To analyze the pressure distribution over the surfaces of different airfoil wings with different aspect ratios of NACA 0012 at different angle of attack (AOA).

ii) To determine the aerodynamic characteristics (Coefficient of Pressure-C_P, Coefficient of lift-C_L, Coefficient of Drag-C_D, Coefficient of Lift to Drag Ratio- C_L / C_D and Coefficient of Performance- $C_L^{1.5}/C_D$) from static pressure distributions of the wing models.

iii) To control passive flow separation on the optimum airfoil wing introducing backward facing step.

iv) To analyze and compare all the above characteristics with the variation of AOA.

1.5 Organization of the Thesis

The dissertation is divided into seven chapters as follows:

a. The first chapter covers the background information along with scope and objectives of the Research.
b. The second chapter reviews the available literature related to the present research work.
c. The third chapter presents the overview of the aerodynamics of wing and backward facing step flow.
d. The fourth chapter describes theory of calculations and mathematical modeling in details.
e. The fifth chapter illustrates the details of experimental set up and procedures.
f. The sixth chapter presents the experimental results and discussion on the important aspects of the results.
g. Finally, the seventh chapter concludes the overall research and recommends few scopes for further research related to the present outcome.

2

Chapter Two

LITERATURE REVIEW

2.1 Literature Survey

Flow separation control is an important technique for the improvement of aerodynamic characteristics through drag reduction. The maximum possible lift force and minimum possible drag force can be obtained by the optimum design of the lifting surface. An interference drag between wing and body also plays an important role on the performance. For a given wing area, the aspect ratio, which is proportional to the square of the wingspan, is of particular significance in determining the performance. Makwana et al. [1] did numerical solution of flow over airfoil where they focused on different technique to reduce flow separation and also gave some idea about different model of CFD. They concluded that to improve the performance of airfoil either lift coefficient must be increased or drag should be decreased and pressure coefficient must be properly distributed on the airfoil surface. Flow characteristics behind a backward-facing step was studied by Jagannath [2]. There designed a new axisymmetric model. An extensive review was made to study the wake characteristics of a backward-facing step. He suggested that the wake of a separated shear layer to be dependent on parameters such as: expansion ratio, aspect ratio, free stream turbulence intensity, boundary layer state and thickness at separation. The individual and combined effects of these parameters on the reattachment length are investigated and discussed in details. Due to unexpected flow separation the aerodynamic performance of wings at low Reynolds number regime is typically low. Yousefi et al. [3] did numerical study of flow separation control by tangential and perpendicular blowing on the NACA 0012 airfoil. The results showed that in tangential blowing by changing blowing amplitude and coefficient the lift to drag ratio can be increased. Best result was achieved at 0.5 blowing amplitude and 0.0875 blowing coefficient. In perpendicular blowing lower blowing amplitude and coefficient give somewhat good result than baseline case. Aram et al. [4] conducted a computational study to explore the effect of synthetic jet orientation on boundary layer separation control. A variety of flow statistics were computed and those indicated that despite the smaller overall blockage represented by the stream wise oriented slot, it was more effective in increasing the momentum of the boundary layer. In general, boundary layer modification can be achieved by preventing or provoking separation, delaying or advancing transitions, suppressing or enhancing turbulence which may lead to drag reduction, lift enhancement, noise suppression, mixing augmentation etc. [5].

In a turbulent backward facing step flow coherent structures are generated by active and passive separation control devices. Xingyu [6] used three types of flow control devices in his experiments to investigate coherent structures in a turbulent backward facing step (BFS) flow that were implemented independently on the backward facing step in order to control the turbulent flow separation downstream of the step. Experimental results showed that the three types of flow control devices were able to reduce the reattachment length by generating quasi-periodic coherent motions in the separated shear layer. These coherent structures lead to an increase in Reynolds shear stress and played an important role in the momentum transfer in the turbulent shear flow. Shan et al. [7] numerically studied the flow separation and transition around a NACA 0012 airfoil using the direct numerical simulation (DNS). The details regarding flow separation, vortex shedding and boundary layer reattachment was captured there. Moreover, several three-dimensional CFD studies [8–12] have been carried out to simplify the simulation of flow fields around airfoils by neglecting active or passive flow control techniques. In addition, flow control methods such as suction, blowing, and the use of synthetic jets have been investigated experimentally [13–16] over thick and NACA airfoils under different flow conditions. Different studies have demonstrated that suction slot can modify the pressure distribution over an airfoil surface and have a substantial effect on lift and drag coefficients [17]. Huang et al. [18] studied the suction and blowing flow control techniques on a NACA0012 airfoil. The combination of jet location and angle of attack showed a remarkable difference concerning lift coefficient as perpendicular suction at the leading edge increased in comparison to the case in other suction situations. Moreover, the tangential blowing at downstream locations was found to lead to the maximum increase in the lift coefficient value.

Ara [19] did an experiment on curved trailing edge tapered wing platform and also did the experiment by adding winglet at the wing tip of the reference wing. The results showed that lift to drag ratios increased and induced drag decreased for wing models with winglets compared to wing models without winglet. Performance of aerodynamic characteristics depends greatly on aspect ratio of the wing. For higher aspect ratio less wing tip vortices are produced on the tip of the wing. Kopac et al. [20] investigated the effect of aspect ratio on the airfoil performance for airfoil about axially symmetric wings as function of angle of attack. There the magnitudes of aerodynamic forces and moments of airfoils resulting from the incompressible viscous flow fields were determined experimentally. The TE54 wind tunnel used for the experiments was an open conduit and had a 300×300 mm x-section with a closed test chamber. There different type of airfoils were tested under the airflow speed of 33.76 m/s and it was concluded that the airfoil with the aspect ratio of 2.761 yields the optimum performance. Rosas et al. [21] numerically studied flow separation control through oscillatory fluid injection, in which lift coefficient increased. Akcayoz et al. [21] examined the optimization of synthetic jet parameters on a NACA0015 airfoil in different angles of attack to increase the lift to drag ratio. Their results revealed that the optimum jet location moved toward the leading edge and the optimum jet angle incremented as the angle of attack increased. Many flow control studies by CFD approaches [23-26] had been conducted to investigate the effects of blowing and suction jets on the aerodynamic performance of airfoils. Hua et al. [27] focused on numerical investigation of subsonic flow separation over a NACA0012 airfoil with a 6°angle of attack and flow separation control with vortex generators. The numerical simulations of three cases including an uncontrolled baseline case, a controlled case with passive vortex generator, and a controlled case with active vortex generator were carried out. The numerical simulation was solved by the three-dimensional Navier-Stokes equations for compressible flow using a fully implicit LU-SGS method. A fourth-order finite difference scheme was also used to compute the spatial derivatives. The immersed boundary method was used to model both the passive and active vortex generators. The study showed that the introduction of the passive vortex generator did not alter the frequency of separation. But in the case with active control, the frequency of the sinusoidal forcing was chosen close to the natural frequency of separation. They concluded that the passive vortex generators could partially eliminate the separation by reattaching the separated shear layer to the airfoil over a significant extent. The size of the averaged separation zone had been reduced by more than 80%.Patel et al. [28] had obtained the drag and lift forces using CFD. Kevadiya [29] investigated NACA 4412 airfoil at various angles of attack from 0° to 12° using CFD analysis. The effect of transonic flow over an airfoil was studied by Novel et al. [30] where a comparative analysis had been done to analyze the variation of the angle of attack and Mach number.

So, it is understood that several researches on airfoil to control flow separation have been carried out both numerically and experimentally. Still the aerodynamic performances of symmetric airfoil (NACA 0012) with passive flow separation control for different aspect ratios are yet to be explored experimentally. For this, an effort has been taken to investigate the aerodynamic performance with passive flow separation control for different aspect ratios through experiment by using wind-tunnel.

3

Chapter Three

AN OVERVIEW OF WING AERODYNAMICS AND BACKWARD FACING STEP FLOW

3.1 Geometric Features of Wing

The wing is the principal structural unit of the airplane. It is an important component of an aircraft that generates lift when comes into contact with moving air molecules i.e. wind. It may be considered as the most fundamental component of an aircraft, since a fixed-wing aircraft is not able to fly without it. The main function of the wing of an aircraft is to generate lift force to make the flight possible in the air. This will be generated by a special wing cross section which is called airfoil. Wing is a three-dimensional component, while the airfoil is two-dimensional section as shown in figure 3.1. The wing may have a constant or a non-constant cross-section across the wing [30]. Airfoils are basically replicas of wings that is much smaller in size. With the drag and lift values that are taken with airfoils, coefficients are calculated and since coefficients do not depend on wing size, larger wings can be produced.

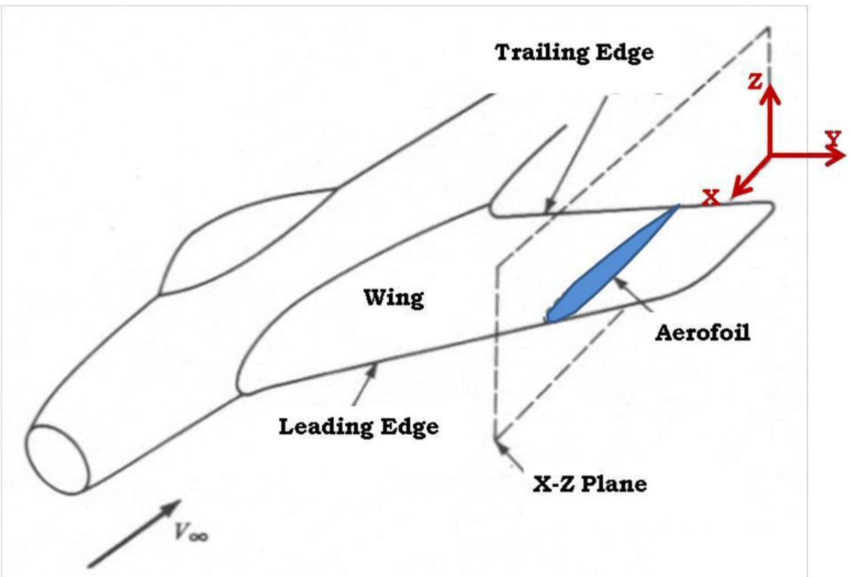

Figure 3.1: Wing and Aerofoil with Nomenclature [32]

Wing has several functions beyond that of providing lift. For a wing to produce "lift", it must be oriented at a suitable angle of attack relative to the flow of air past the wing. In aerodynamics, angle of attack (AOA) specifies the angle between the chord line of the wing of a fixed-wing aircraft and the vector representing the relative motion between the aircraft and the atmosphere. The wing has a finite length called its wing span. If the wing is sliced with a plane parallel to the x-z plane of the aircraft, the intersection of the wing surfaces with that plane is called an airfoil. The wing is a 3D object, but it is usually treated as a set of two 2D geometric features; planform (x-y plane) and airfoil (x-z plane) as shown in figure 3.1.

3.2 Geometric Parameters of Wing

Aircraft wing can be defined by several geometric parameters such as span (b), wing surface area or planform (S), root chord (C_{root}), tip chord (C_{tip}) etc. as shown in figure 3.2. Other important parameters are discussed below:

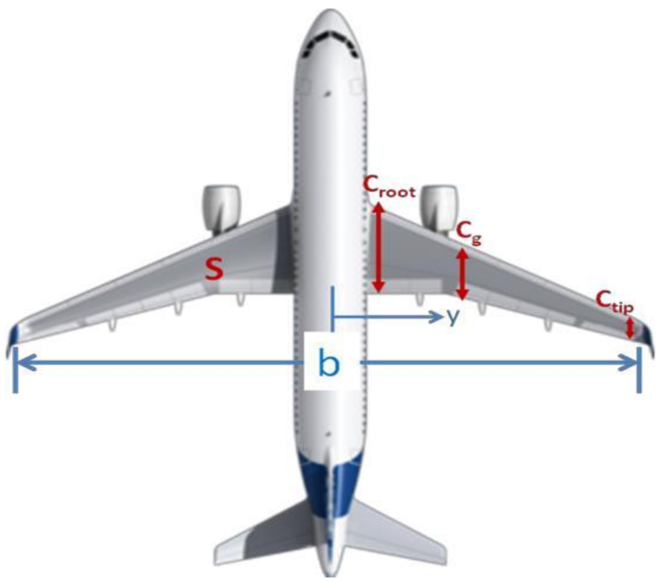

Figure 3.2: Wing Geometric Parameters [31, 32]

3.2.1 Mean Geometric Chord (C_g)

The mean geometric chord is the chord of a rectangular wing having the same span and the same area as the original wing. It can be found for any general wing in the following way:

$$C_g = \frac{\int_0^{\frac{b}{2}} c(y)dy}{\int_0^{b/2} dy} = \frac{2}{b}\int_0^{b/2} c(y)dy = \frac{S}{b} \tag{3.1}$$

3.2.2 Mean aerodynamic chord (C_{MAC})

The MAC is a two-dimensional representation of the whole wing. The pressure distribution over the entire wing can be reduced to a single lift force on and a moment around the aerodynamic center of the MAC. Therefore, not only the length but also the position of MAC is often important. In particular, the position of center of gravity (CG) of an aircraft is usually measured relative to the MAC, as the percentage of the distance from the leading edge of MAC to CG with respect to MAC itself. The mean aerodynamic chord is (loosely) the chord of a rectangular wing with the span, (not area) that has the same aerodynamic properties with regarding the pitching moment characteristics as the original wing. It can be found for any general wing in the following way:

$$C_{MAC} = \frac{\int_0^{b/2}[c(y)]^2 dy}{\int_0^{b/2} c(y)dy} = \frac{2}{S}\int_0^{b/2}[c(y)]^2 dy \tag{3.2}$$

3.2.3 Aspect ratio (AR)

Aspect ratio is a measure of how long and slender a wing is from tip to tip. The Aspect Ratio of a wing is defined to be the square of the span divided by the wing area and is given the symbol AR. For a rectangular wing, this reduces to the ratio of the span to the chord length. A square wing would have an aspect ratio of 1.Figure 3.3

shows the aspect ratio of general and rectangular airfoil. Aspect ratio can be calculated in following ways:

$$AR = s^2 / A = s^2 / (s * c) = s / c \tag{3.3}$$

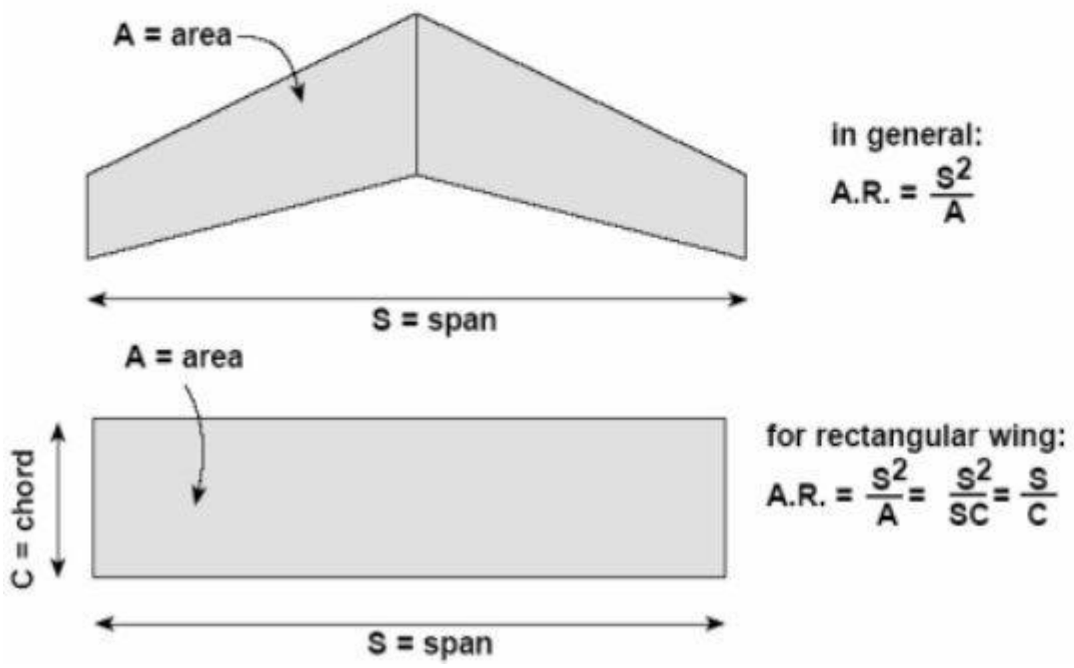

Figure 3.3: Wing Geometry showing Aspect Ratio [32]

3.2.4 Taper ratio (λ)

It is the ratio of the tip chord to the root chord and is expressed as follows and shown if figure 3.5:

$$\textbf{Taper ratio } (\lambda) = C_t/C_r \tag{3.4}$$

3.3 General Features of an Aerofoil

The history of the development of airfoil shapes is long and involves numerous contributions by scientists from all over the world. By the beginning of the twentieth century the methods of classical hydrodynamics had been successfully applied to airfoils, and it became possible to predict the lifting characteristics of certain airfoils shapes mathematically. In 1929, the National Advisory Committee for Aeronautics

(NACA) began studying the characteristics of systematic series of airfoil in an effort to determine exact characteristics.

3.3.1 Terminologies

The airfoils were composed of a thickness envelope wrapped around a mean chamber line as shown by figure 3.4.

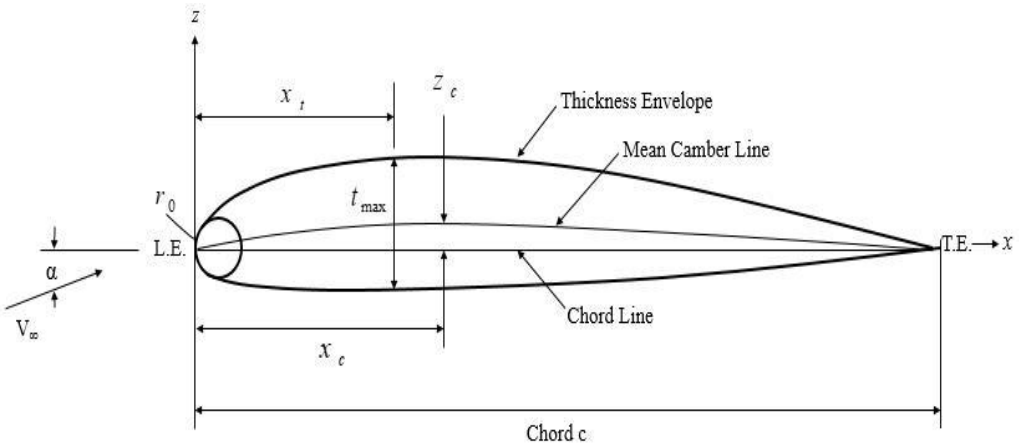

Figure 3.4: Airfoil Nomenclature [32]

The cross-sectional shape obtained by the intersection of the wing with the perpendicular plane is called an airfoil. The major design feature of an airfoil is the mean cambered line, which is the locus of points halfway between the upper and lower surfaces as measured perpendicular to the mean cambered line itself. The most forward and rearward points of the mean cambered line are the leading and trailing edges respectively. The straight line connecting the leading and trailing edges is the chord line of the airfoil and the precise distance from the leading to the trailing edge measured along the chord line is simply designated the chord of the airfoil, given by the symbol C. The camber is the maximum distance between the mean camber line and the chord line, measured perpendicular to the chord line. The camber, the shape of the mean camber line and to a lesser extent, the thickness distribution of the airfoil essentially controls the lift and moment characteristics of the airfoil. For symmetrical airfoil the mean camber line coincides with chord line. The various families of airfoils are designed to show the effects of varying the geometrical variables on their aerodynamic characteristics such as lift, drag and moment, as functions of the geometric angle of attack. The geometric angle of attack α is defined as the angle between the flight path and the chord line of the airfoil. The geometrical variables include the maximum chamber $\boldsymbol{z_c}$ of the mean chamber line and its distance x_c behind the leading edge, the maximum thickness $t_{\max}$ and its distance x_t behind the leading edge, the radius of curvature r_0 of the surface at the leading edge and the trailing edge angle between the upper and lower surfaces at the trailing edge. Theoretical studies and wind tunnel experiments show the effects of these variables in a way to facilitate the choice of shapes for specific applications. The lifting characteristics of an airfoil below stall conditions are negligibly influenced by viscosity and the resultant of the pressure forces on the airfoil is only slightly altered by the thickness envelope provided that the ratio of maximum thickness to chord ($t_{max/C}$) and the maximum mean chamber $\boldsymbol{z_c}$ remain small and the airfoil is operating at a small angle of attack. These conditions are usually met during standard operations of airfoils. In a real fluid, lift is within 10% of theory for inviscid fluids up to an angle of attack of α of 12^0 to 15° depending on the geometric factors. At low angles the streamlines follow the surface smoothly, although particularly on the upper surface the boundary layer causes some deviation. At angles of attack greater than α, called the stalling angle, the flow separates on the upper surface and large vortices are formed. At these angles, the flow becomes unsteady and there is a dramatic decrease in lift, accompanied by an increase in drag and large changes in the moment exerted on the airfoil by the altered pressure distribution.

The lift force increases almost linearly with angle of attack until a maximum value is reached, whereupon the wing is said to stall. The variation of the drag force with angle of attack is approximately parabolic. It is desirable for the wing to have the maximum lift and smallest possible drag i.e. the maximum possible lift to drag ratio. The variation of all these aerodynamic characteristics (lift force, drag force and lift to drag ratio) with angle of attack for a typical aircraft are shown in figure 3.5. From the figure we can see that, when the angle of attack is increased, the L/D ratio rapidly increases from zero to the maximum value. After reaching the maximum value, as the angle of attack is increased further, the L/D ratio decreases until the stalling angle is reached and keeps decreasing even beyond that angle. The reason for this characteristics is that when the angle of attack is increased, both C_L and C_D increase but C_L increases more than C_D. The greater the lift/drag ratio will be obtained at small angle between C_L axis and the straight line.

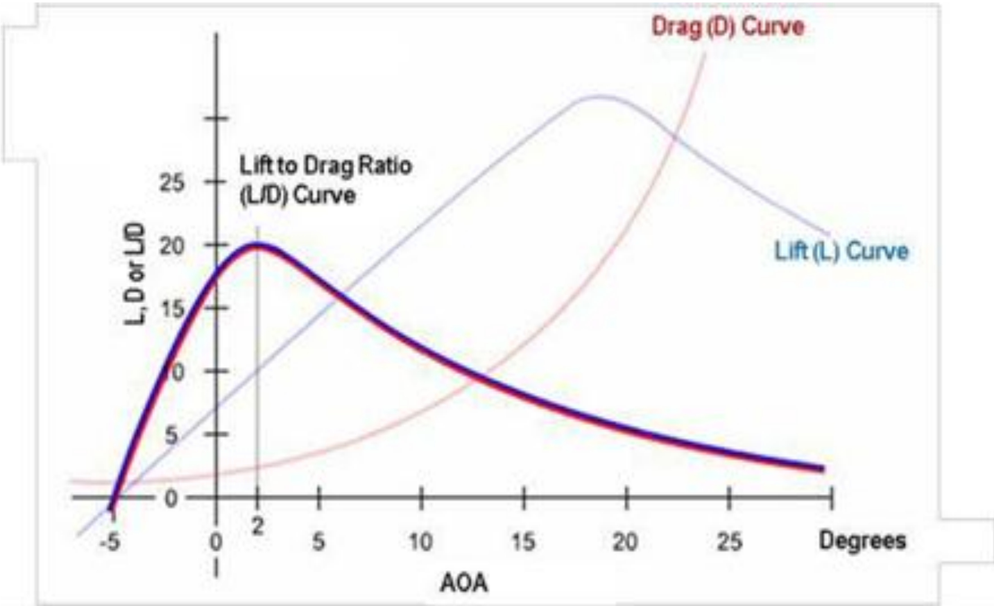

Figure 3.5: Variation of Aerodynamic Characteristics with Angle of Attack [32]

3.3.2 Airfoil Pressure Distribution

A typical pressure distribution of an airfoil is shown in figure 3.6, the arrows representing pressure vectors. In a perfect fluid, the total force on the airfoil is the lift ρV_∞ acting normal to V_∞. Its magnitude can be represented as the resultant of two components, one normal to the chord line of magnitude ρV_∞ Cos α, given by the integral over the chord of the pressure difference between points y_l and y_u on the lower and upper surfaces, and the other parallel to the chord line of magnitude ρV_∞ Sin α, representing the leading edge suction. In a real fluid, viscous effects alter the pressure distribution and friction drag is generated, though at low angles of attack the theoretical pressure distribution can be taken as a valid approximation.

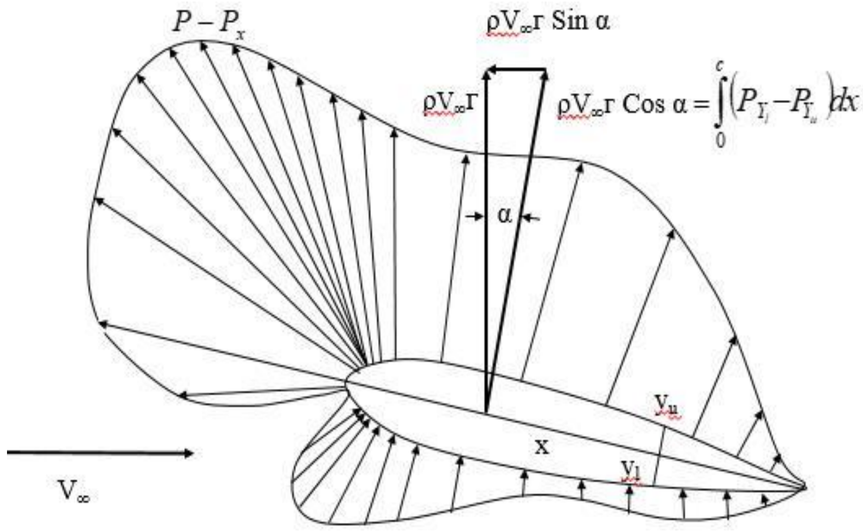

Figure 3.6: Airfoil Pressure Distribution [32]

3.4. Aerodynamic Characteristics of Aerofoils

3.4.1. Aerodynamic forces Developed by Aerofoil

The static pressure on the top of the surface and on the bottom of the surface will vary when an airfoil-shaped body moved through the air. In a positive cambered airfoil the lower surface static pressure is higher than ambient pressure and upper surface static pressure is less than the ambient pressure. The pressure differences between the upper and lower surfaces will be higher as the angle of attack increases as shown in figure 3.7.

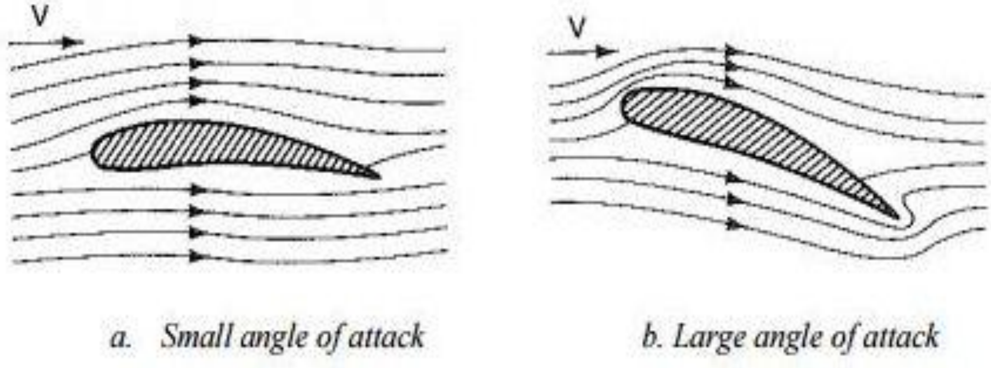

Figure 3.7: Flow around an airfoil [34,40]

The force divided by the area is called pressure, so the aerodynamaic force generated by an airfoil in a flow field may be calculated by multiplication of total pressure by area.The total pressure is simply determined by the integration of pressure over the entire surface.The magnitude,location and direction of this aerodynamic force are functions of airfoil geometry, angle of attack,flow properties and arispeed relative to airfoil.The location of this resultant force out of integration is called centre of pressure.The location of this centre depends on aircraft speed aand the airfoils angle of attack.Thus, the pressure and shear distributiuons over the airfoil generate an aerodynamic force.This resultant force is replaced with two aerdynamic forces as shown in figure 3.8.The aerodynamic force can be resolved into two forces, perpendicular (lift) and parallel(drag) relative to the wind.

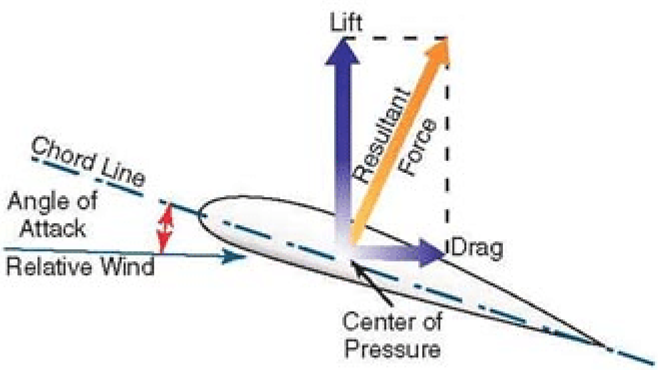

Figure 3.8 : Aerodynamic Forces Acting on Aerofoil [37]

3.4.2. Lift and Drag Coefficient of Airfoil

The lift and drag generated by an airfoil are usually measured in a wind tunnel and published as coefficient which are dimensionless. These are mainly the variations of non-dimensional lift and drag relative to angle of attack [33, 45]. Two aerodynamic forces (lift and drag) are usually non-dimensional by dividing them to appropriate parameters as follows:

$$\text{Lift Coefficient, } C_L = \frac{L}{\frac{1}{2}\rho V_\infty^2 S} \quad (3.5)$$

$$\text{Drag Coefficient, } C_D = \frac{D}{\frac{1}{2}\rho V_\infty^2 S} \quad (3.6)$$

Where, L and D are the lift force and drag force respectively.

S is the Planform area=Chord x Span.

V_∞ is the free stream air velocity.

$\frac{1}{2}\rho V_\infty^2$ is the dynamic pressure and ρ is the density of air.

Another important parameter, the lift-to-drag ratio (L/D) is the amount of lift generated by an airfoil, divided by the drag it creates by moving through the air. An airplane has a high L/D if it produces a large amount of lift or a small amount of drag. A higher or more favorable L/D is typically one of the major goals in aircraft design.

$$Ratio = \frac{Lift}{Drag} = \frac{L}{D} \tag{3.7}$$

Thus, the performance and characteristics of an airfoil may be evaluated by looking at the following graphs:

a. The variations of lift coefficient (C_L) with angle of attack (α).

b. The variations of drag coefficient (C_D) with angle of attack (α).

c. The variations of lift coefficient (C_L) with drag coefficient(C_D)

d. The variations of lift-to-drag ratio (L/D) with angle of attack (α)

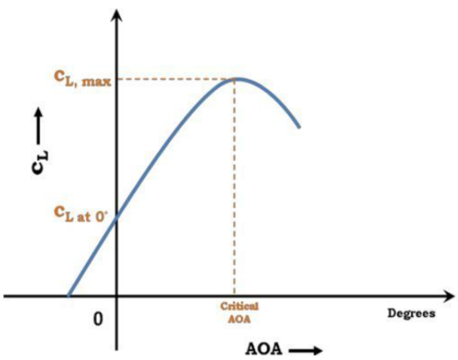

α

a. C_L vs α graph

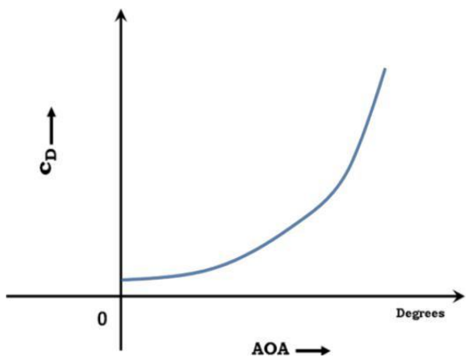

α

b. C_D vs α graph

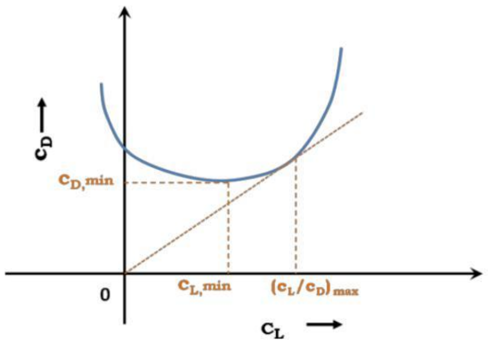

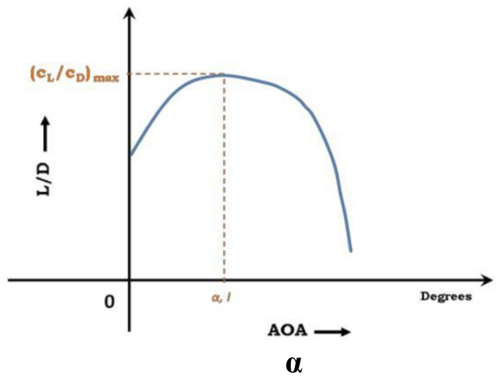

c. C_D vs C_L graph

d. L/D vs α graph

Figure 3.9: Graphs of Different Parameters of Aerofoil [33-34]

3.4.3. Aerofoil Data Sources

Proper airfoil selections are possible from the previously designed and published airfoil sections. Two reliable airfoil resources are NACA and Eppler. The details of Eppler airfoils have been published in [35]. NACA airfoils have been published in a book published by Abbott and Von Doenhoff [36]. Eppler airfoil names begin with the letter "E" followed by three numbers. In general, the Eppler airfoils are for very low Reynolds number, Wortman airfoils for low (sailplane-ish) Reynolds number, and the NASA Low-Speed airfoils (e.g. LS (1)-0413) and Mid Speed Airfoils e.g. MS (1)-0313) are for "moderate" Reynolds numbers [35].

3.4.4. NACA Aerofoils

The NACA airfoils are airfoil shapes for aircraft wings developed by the National Advisory Committee for Aeronautics (NACA). Airfoils are described and can be distinguished between each other by the numbers that follow the acronym NACA. There are six NACA families which are 4- Digit, 5-Digit, 6-Series, 7-Series, 8-Series and 16-Series. In NACA Four Digit Series, there are four digits that follow the acronym NACA and these 4 digits show 3 different properties of the airfoil. The first family of airfoils designed in the above-mentioned way is known as the NACA Four-Digit aerofoils. The explanation of the 4-digit NACA aerofoil is as follows [35, 46]:

a. The first digit specifies the maximum camber in percentage of the chord.

b. The second digit indicates the position of the maximum camber in tenths of chord.

c. The last two digits provide the maximum thickness of the airfoil in percentage of chord.

For NACA 0012

Chord of airfoil, c = 1

For symmetric airfoil mean chamber line coincide with chord line so for NACA 0012 there is no chamber

Maximum wing thickness, t = last two digit × %c

=12 × 1/100

=0.12

By applying C++ Programming Language, the surface profile of the airfoil was generated by using basic equation of airfoil

One of the most reliable resources and widely used data base is the airfoils developed by National Advisory Committee for Aeronautics, NACA (predecessor of NASA) in 1930s and 1940s.The formula for the shape of a NACA 00xx foil, with "xx" being replaced by the percentage of thickness to chord [32], is:

$$y_t = \frac{t}{0.2}c\left[0.2969\sqrt{\frac{x}{c}} - 0.1260\left(\frac{x}{c}\right) - 0.3516\left(\frac{x}{c}\right)^2 + 0.2843\left(\frac{x}{c}\right)^3 - 0.1015\left(\frac{x}{c}\right)^4\right], \quad [3.8]$$

Where,

c= is the chord length,

x =is the position along the chord from 0 to c,

y =is the half thickness at a given value of x (centerline to surface), and

t= is the maximum thickness as a fraction of the chord (so 100 t gives the last two digits in the NACA 4-digit denomination).

In this equation, at (x/c) = 1 (the trailing edge of the airfoil), the thickness is not quite zero. If a zero-thickness trailing edge is required, for example for computational work, one of the coefficients should be modified such that they sum to zero. Modifying the last coefficient (i.e. to -0.1036) will result in the smallest change to the overall shape of the airfoil. The leading edge approximates a cylinder with a radius [32] of:

$$r = 1.1019\, t^2.$$

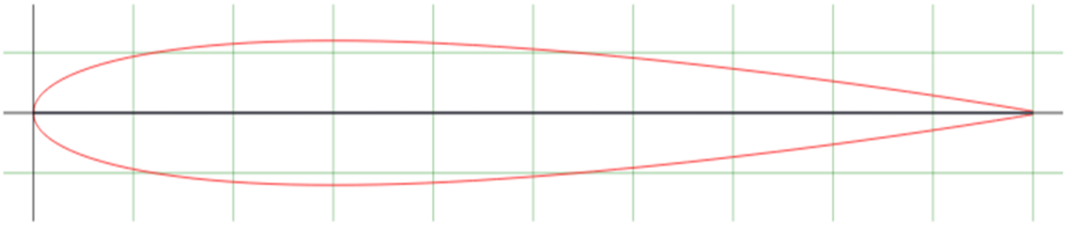

Figure 3.10 Profile of NACA 0012 airfoil [37]

3.5. General Features of the Backward-Facing Step Flow

In the aerospace industry the importance for flow control has greatly enhanced as greater aerodynamic characteristics are pursued and innovative approaches to drag reduction are introduced. In the past decades many strategies for controlling boundary layer separation have been studied in order to delay separation on airfoils. Separated flows are commonly happen in several engineering applications such as aircraft wings, turbine and compressor blades, combustors, suddenly expanding pipes etc. The nature of separated flows as a result of their instabilities are very complicated. To modify these flow characteristics, researchers conducted experiments on numerous geometries that include rib, fence, bluff body with a splitter plate, suddenly expanding pipes, forward and backward-facing steps, cavities and bluff bodies with blunt leading edges. These geometries modify the flow characteristics to a particular extent by dominant the separation or the reattachment purpose or each, that are otherwise unsteady due to its single fixed separation point and also the wake dynamics composed by the downstream disturbances the backward-facing step is taken into account by most as the ideal canonical separated flow geometry. An illustration of the wake characteristics behind a backward-facing step is shown in figure 3.11.

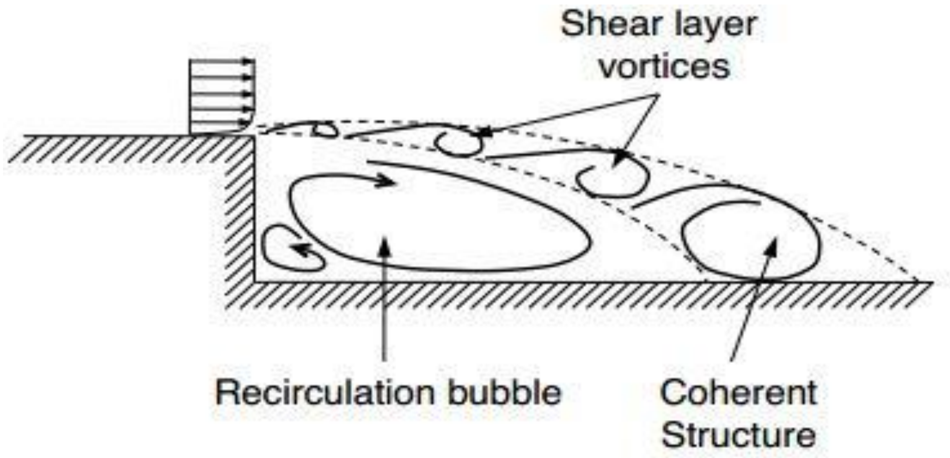

Figure 3.11: Backward-facing step flow features [2]

The wake of a backward-facing step has mainly divided into two regions: the free shear layer and the low velocity recirculating bubble region. The vortices in the shear layer roll up and pair with the adjacent vortices to form larger coherent structure, due to instabilities of the separated flows [2]. These vortices entrain fluid from the region below and trigger the recirculation. The wake of the step the free shear layer reattaches at the bottom wall as a result of adverse pressure gradient. The common characteristics of a backward facing step flow begins with an upstream boundary layer separating at the step edge due to the adverse pressure gradient that develops into a thin shear layer. As the flow goes to downstream, the shear layer grows in size with the amalgamation of the turbulent structures contained within. This region where the shear layer develops and grows is referred to as the shear layer region and is shown in figure 3.11. The turbulent structures in the shear layer entrain irrotational fluid from the non-turbulent region outside the shear layer. This flow entrainment causes the formation of a low velocity recirculation in the region, which is located between the shear layer and the adjacent wall. Due to the favorable pressure gradient created by the fluid entrained, the shear layer eventually curves down towards the wall and impinges at a location known as the reattachment point. The reattachment points spread within a certain span along the stream wise distance, which is referred to as the reattachment zone. These three regions in a whole comprise the important features of a BFS flow that can be modified or controlled to achieve desirable outcome such as, enhanced mixing characteristics and reduced drag, noise and vibrations.

4

Chapter Four

MATHEMATICAL MODELING

4.1 Determination of Pressure Coefficient

The wind tunnel has a reference pressure tap located upstream of the test section and the pressure there is:

$$P_\infty = \rho_{water} g(h_{atm} - h_\infty) \qquad (4.1)$$

From the Bernoulli relation, the corresponding velocity along a horizontal stream line is:

$$V_\infty = \sqrt{\frac{2\rho_{water}\, g(h_{atm} - h_\infty)}{\rho_{air}}} \qquad (4.2)$$

The 32 pressure taps provide pressure values determined from the manometer as:

$$P_i = \rho_{water} g(h_{atm} - h_\infty) \qquad (4.3)$$

The pressure coefficient (C_p) is a dimensionless number which describes the relative pressures throughout a flow field in fluid dynamics. It is used in aerodynamics and hydrodynamics. Every point in a fluid flow field has its own unique pressure coefficient. It is very common to find pressures given in terms of C_P rather than the pressure itself. Figure 4.1 shows the pressure distribution at any point over the surface in terms of the pressure coefficient, C_P, which is defined as follows:

$$C_p = \frac{P_{Local} - P_\infty}{\frac{1}{2}\rho V\infty^2} \qquad (4.4)$$

Where, $½\rho V_\infty{}^2$ is the free stream dynamic pressure head

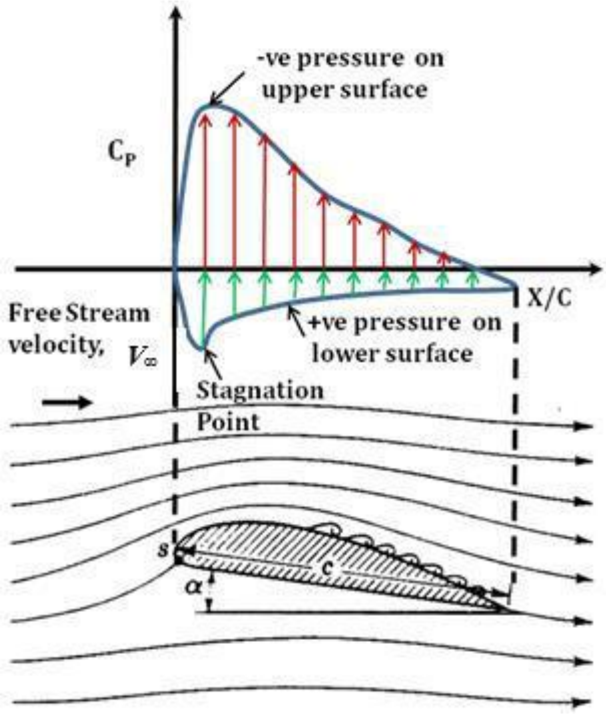

Figure 4.1: Pressure Distribution over an Airfoils Surface in terms of C_P [31, 32]

Thus, surface pressure coefficient, C_p can be calculated from the static pressure by the following formula [31, 32].

$$C_{p,i} = \frac{P_i - P_\infty}{\frac{1}{2}\rho V_\infty^2} \tag{4.5}$$

Where, P_i is the surface static pressure at any designated point i.

Values of C_p at any point over the aero foil surface can be approximated from the corresponding boundary values by using the first order Lagrange interpolation and extrapolation:

$$C_p(x) = \frac{(x - x_1)}{(x_0 - x_1)} C_{p,0} - \frac{(x - x_1)}{(x_0 - x_1)} C_{p,1} \tag{4.6}$$

4.2 Estimation of Aerodynamic Force Coefficients from C_P

The aerodynamic forces and moments on the body are due to only two basic sources such as the pressure distribution over the body surface and the Shear stress distribution over the body surface [34]. No matter how complex the body shape may be, the aerodynamic forces and moments on the body are due entirely to the above two basic sources. The *only* mechanisms nature has for communicating a force to a body moving through a fluid are pressure and shear stress distributions on the body surface. Both pressure p and shear stress τ have dimensions of force per unit area (pounds per square foot or newton's per square meter). As sketched in figure 4.2, p acts normal to the surface, and τ acts tangential to the surface. Shear stress is due to the "tugging action" on the surface, which is caused by friction between the body and the air.

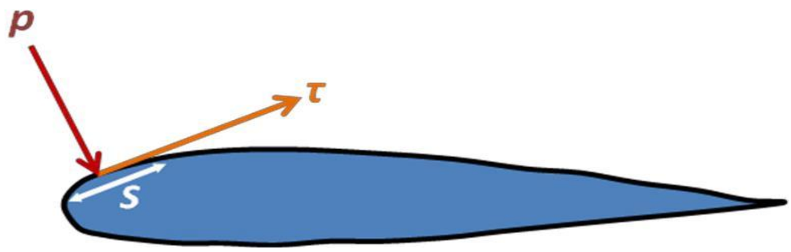

Figure 4.2: Illustration of Pressure and shear Stress on Aerofoil Surface [35]

The net effect of the p and τ distributions integrated over the complete body surface is a resultant aerodynamic force R on the body. In turn, the resultant R can be split into components, two sets of which are shown in figure 4.3. In figure 4.3, U_∞ is the relative wind, defined as the flow velocity far ahead of the body. The flow far away from the body is called the free stream, and hence U_∞ is also called the free stream velocity. In figure 4.3, by definition,

L = lift = component of R perpendicular to U_∞

D = drag = component of R parallel to U_∞

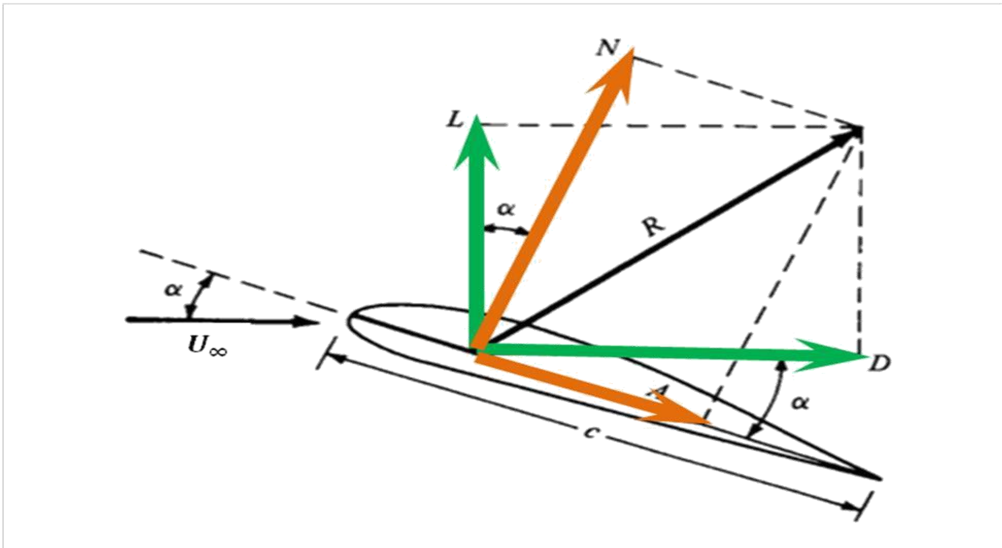

Figure 4.3: Resultant Aerodynamic Force and its Components [33, 44]

The chord c is the linear distance from the leading edge to the trailing edge of the body. Sometimes, R is split into components perpendicular and parallel to the chord, as also shown in figure 4.3. By definition,

N = normal force = component of R perpendicular to c
A = axial force = component of R parallel to c

The angle of attack α is defined as the angle between c and U. Hence, α is also the angle between L and N and between D and A. The geometrical relation between these two sets of components is found from figure 4.3 as:

$$L = N\cos\propto - A\sin\propto \qquad (4.7)$$

$$D = N\sin\propto + A\cos\propto \qquad (4.8)$$

The integration of the pressure and shear stress distributions can be done to obtain the aerodynamic forces and moments [32, 47]. Let us consider the two-dimensional body sketched in figure 4.4. The chord line is drawn horizontally, and hence the relative wind is inclined relative to the horizontal by the angle of attack α. A xy coordinate system is oriented parallel and perpendicular, respectively, to the chord. The distance from the leading edge measured along the body surface to an arbitrary point A on the upper surface is s_u; similarly, the distance to an arbitrary point B on the lower surface is S_l. The pressure and shear stress on the upper surface are denoted by P_u and τ_u, respectively; both P_u and τ_u, are functions of S_u. Similarly, P_l and τ_l are the corresponding quantities on the lower surface and are functions of S_l.

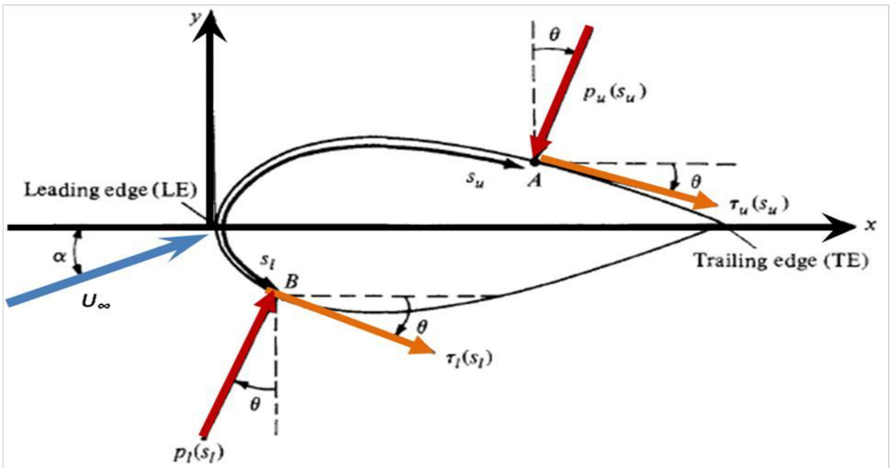

Figure 4.4: Nomenclature for Integration of *p* and *τ* Distribution [32, 47]

At a given point, the pressure is normal to the surface and is oriented at an angle θ relative to the perpendicular; shear stress is tangential to the surface and is oriented at the same angle θ relative to the horizontal. In figure 4.4, the sign convention for θ is positive when measured clockwise from the vertical line to the direction of p and from the horizontal line to the direction of τ.

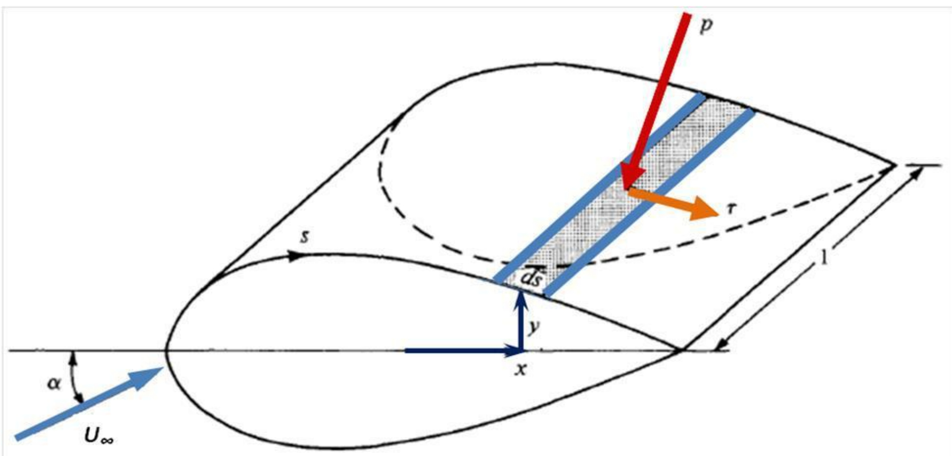

Figure 4.5: Aerodynamic Force on an Element of the Body Surface [32, 47]

Now let us consider the two-dimensional shape in figure 4.5 as a cross section of an infinitely long cylinder of uniform section. A unit span of such a cylinder is shown in figure 4.5, let us consider an elemental surface area *dS* of this cylinder, where *dS* = *(ds)(l)* as shown by the shaded area. We are interested in the contribution to the total normal force *N′* and the total axial force *A′* due to the pressure and shear stress on the elemental area *dS*. The primes on *N′* and *A′* denote force per unit span. Examining both figures 4.4 and 4.5, it is seen that the elemental normal and axial forces acting on the elemental surface *d*S on the *upper* body surface are

$$dN'_u = -p_u d_{S_u} \cos\theta - \tau_u d_{S_u} \sin\theta \qquad (4.9)$$

$$dA'_u = -p_u d_{S_u} \sin\theta + \tau_u d_{S_u} \cos\theta \qquad (4.10)$$

On the lower body surface, we have

$$dN'_l = -p_l d_{S_l} \cos\theta - \tau_l d_{S_l} \sin\theta \qquad (4.11)$$

$$dA'_l = p_l d_{S_l} \sin\theta + \tau_l d_{S_l} \cos\theta \qquad (4.12)$$

In these equations, the positive clockwise convention for θ must be followed. For example, consider again figure 4.4, near the leading edge of the body, where the slope of the upper body surface is positive, τ is inclined upward, and hence it gives a positive contribution to *N'*. For an upward inclined τ, θ would be counterclockwise, hence negative. Therefore, in Equation (4.9), *Sin* θ would be negative, making the shear stress term (the last term) a positive value, as it should be in this instance.

The total normal and axial forces per unit span are obtained by integrating Equations (4.9) to (4.12) from the leading edge (LE) to the trailing edge (TE):

$$N' = -\int_{LE}^{TE} (p_u \cos\theta + \tau_u \sin\theta) d_{S_u} + \int_{LE}^{TE} (p_l \cos\theta - \tau_l \sin\theta) d_{S_l} \qquad (4.13)$$

$$A' = \int_{LE}^{TE} (-p_u \sin\theta + \tau_u \cos\theta) d_{S_u} + \int_{LE}^{TE} (p_l \sin\theta - \tau_l \cos\theta) d_{S_l} \qquad (4.14)$$

In turn, the total lift and drag per unit span can be obtained by inserting Equations (4.13) and (4.14) into (4.7) and (4.8).

There are quantities of an even more fundamental nature than the aerodynamic forces themselves. These are dimensionless force coefficients. We have already defined a dimensional quantity called the free stream dynamic pressure as $q_\infty = ½\rho V_\infty^2$. In addition, let s be a reference area and l be a reference length. The dimensionless force coefficients are defined as follows:

Lift coefficient: $$C_L = \frac{L}{½\rho V\infty^2\, S} \qquad (4.15)$$

Drag coefficient: $$C_D = \frac{D}{½\rho V\infty^2\, S} \qquad (4.16)$$

Normal force coefficient: $$C_N = \frac{N}{½\rho V\infty^2\, S} \qquad (4.17)$$

Axial force coefficient: $$C_A = \frac{A}{½\rho V\infty^2\, S} \qquad (4.18)$$

In the above coefficients, the reference area S and reference length l are chosen to pertain to the given geometric body shape; for different shapes, S and l may be different things. For example, for an airplane wing, S is the planform area, and l is the mean chord length, as illustrated in figure 4.6.

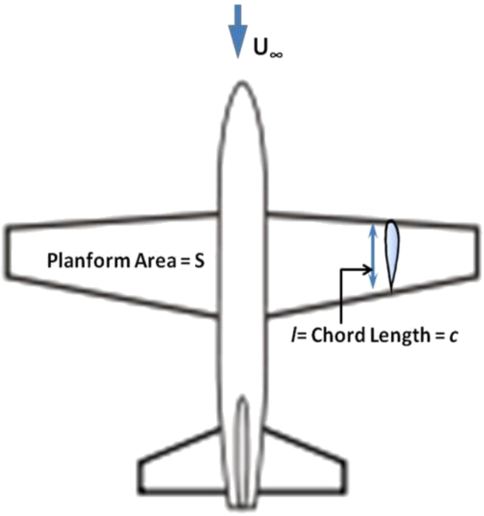

Figure 4.6: Reference Area and Length for Airplane [33]

The symbols in capital letters listed above, i.e., C_L, C_D, C_N, and C_A , denote the force coefficients for a complete three-dimensional body such as an airplane or a finite wing. In contrast, for a two-dimensional body, the forces are per unit span. For these two-dimensional bodies, it is conventional to denote the aerodynamic coefficients by lowercase letters as follows:

$$c_l = \frac{L'}{q_\infty c} \qquad \text{and} \qquad c_d = \frac{D'}{q_\infty c}$$

Where, the reference area S = *c(1)* = c.

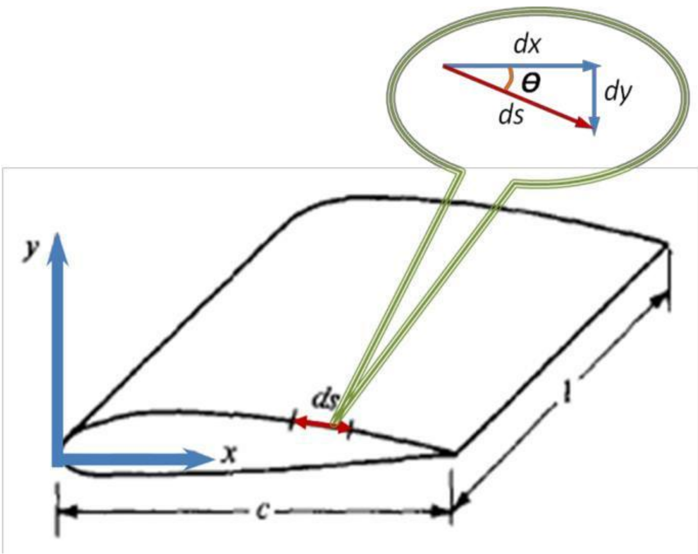

Figure 4.7: Geometrical Relationship of Differential Lengths [32, 47]

The most useful forms of Equations (4.13) and (4.14) are in terms of the dimensionless coefficients introduced above. From the geometry shown in figure 4.7,

$$dx = ds \, Cos\, \theta$$

$$dy = -ds \, Sin\, \theta$$

$$S = c(1)=c$$

Substituting the above expressions of *dx*, *dy and S* into Equations (4.13) and (4.14), dividing by q_∞, we obtain the following integral forms for the force and moment coefficients:

$$C_n = \frac{1}{c}\int_0^c \left(c_{p,l} - c_{p,u}\right)dx + \frac{1}{c}\int_0^c \left(c_{f,u}\frac{dy_u}{dx} + c_{f,l}\frac{dy_l}{dx}\right)dx \qquad (4.19)$$

$$C_a = \frac{1}{c}\int_0^c \left(c_{p,u}\frac{dy_u}{dx} - c_{p,l}\frac{dy_l}{dx}\right)dx + \frac{1}{c}\int_0^c \left(c_{f,u} + c_{f,l}\right)dx \qquad (4.20)$$

Here, y_u is directed above the x axis, and hence is positive, whereas y_l is directed below the x axis, and hence is negative. Also, dy/dx on both the upper and lower surfaces follow the usual rule from calculus, i.e., positive for those portions of the body with a positive slope and negative for those portions with a negative slope. When shear stress due to viscous effect is neglected, an integration of a pressure distribution over an airfoil chord for both upper and lower surfaces is known to provide normal and axial force acting on an airfoil section [31, 37] as follows:

$$C_n = \frac{1}{c}\int_0^c \left(c_{p,l} - c_{p,u}\right)dx \qquad (4.21)$$

$$C_a = \frac{1}{c}\int_0^c \left(c_{p,u}\frac{dy_u}{dx} - c_{p,l}\frac{dy_l}{dx}\right)dx \qquad (4.22)$$

The known pressure coefficients from the experiment can be calculated for the normal and axial force by using a numerical integration of the above equations in the Trapezoidal approximating forms.

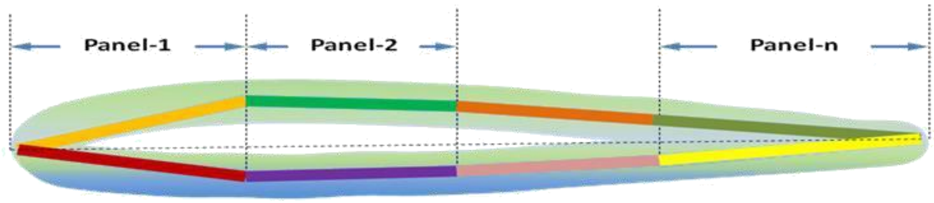

Figure 4.8: Paneling of the Wing Surface [32, 47]

As shown in figure 4.8, both the surfaces of the wing section can be divided into small panels corresponding to a total of gaps between each pressure tap location [48]. When *n* is a number of panels, the equations can be converted as follows:

$$C_n = \sum_{i=1}^{n} \left[(C_{p,l,i} - C_{p,u,i}) \Delta \left(\frac{x_i}{c} \right) \right] \quad (4.23)$$

$$C_a = \sum_{i=1}^{n} \left[\left(C_{p,u,i} \frac{\Delta y_{u,i}}{\Delta x_i} - C_{p,l,i} \frac{\Delta y_{l,i}}{\Delta x_i} \right) \Delta \left(\frac{x_i}{c} \right) \right] \quad (4.24)$$

The interpolated and extrapolated pressure coefficients would be applied to Equation (4.23) and (4.24) in order to get the normal and axial force at a section of interest. Lift and drag coefficient can be obtained from:

$$C_l = C_n \cos \propto - C_a \sin \propto \quad (4.25)$$

$$C_d = C_n \sin \propto - C_a \cos \propto \quad (4.26)$$

The over-all value of the coefficients for the whole wing can be found out by averaging the same values of each segments of the wing along the span.

5

Chapter Five

EXPERIMENTAL SETUP AND METHODOLOGY

5.1 Design and Construction

The wing models are manufactured with extreme precision for taking data. To obtain that objective wing models of different aspect ratios (AR 0.5, AR 1, AR 2) and wing model of AR 2 with backward facing step are designed in Solid works as shown in Figure 5.1,5.2,5.3 and then the aerofoil shapes are cut to get precise size and shape. Finally, wooden wing models are prepared from those designs. From the surface pressure distribution of the wing the aerodynamic characteristics (C_L, C_D and C_L/ C_D) can be calculated as discussed in the previous chapter. Wooden wing models without and with backward facing step wing model are prepared with a specific aerofoil, appropriate fixture is made to set the models in the wind tunnel and a multi-tube manometer is fabricated to take the pressure readings from the surfaces of the wing models.

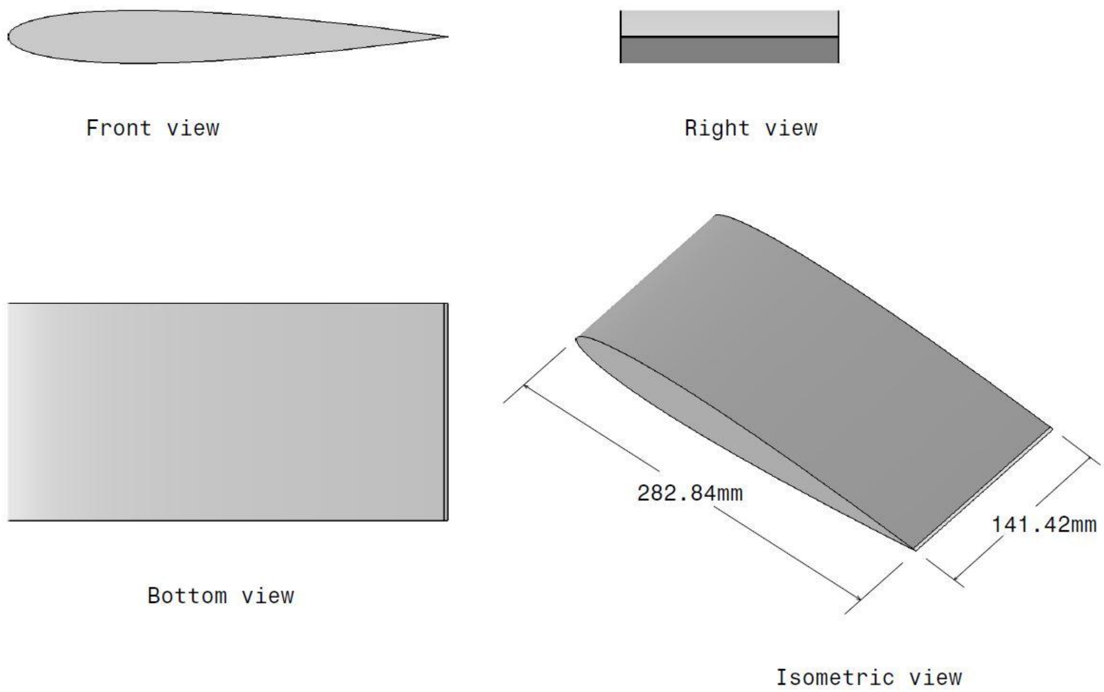

Figure 5.1: Designed wing model of AR 0.5

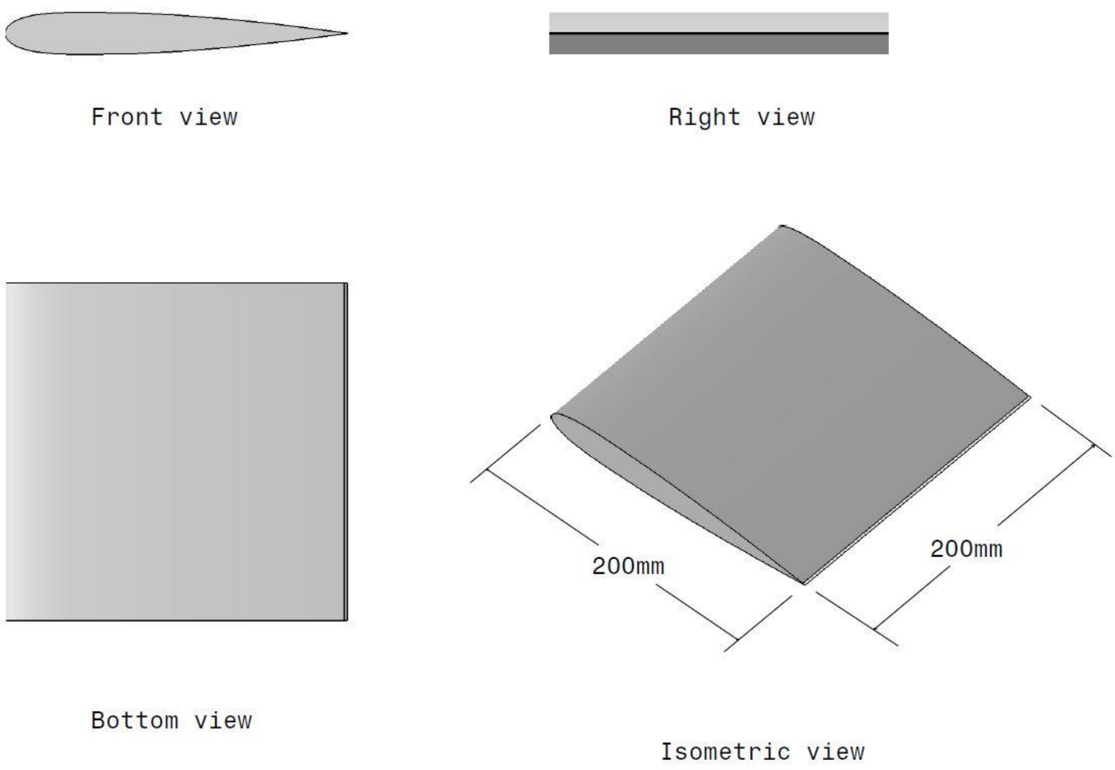

Figure 5.2: Designed wing model of AR 1

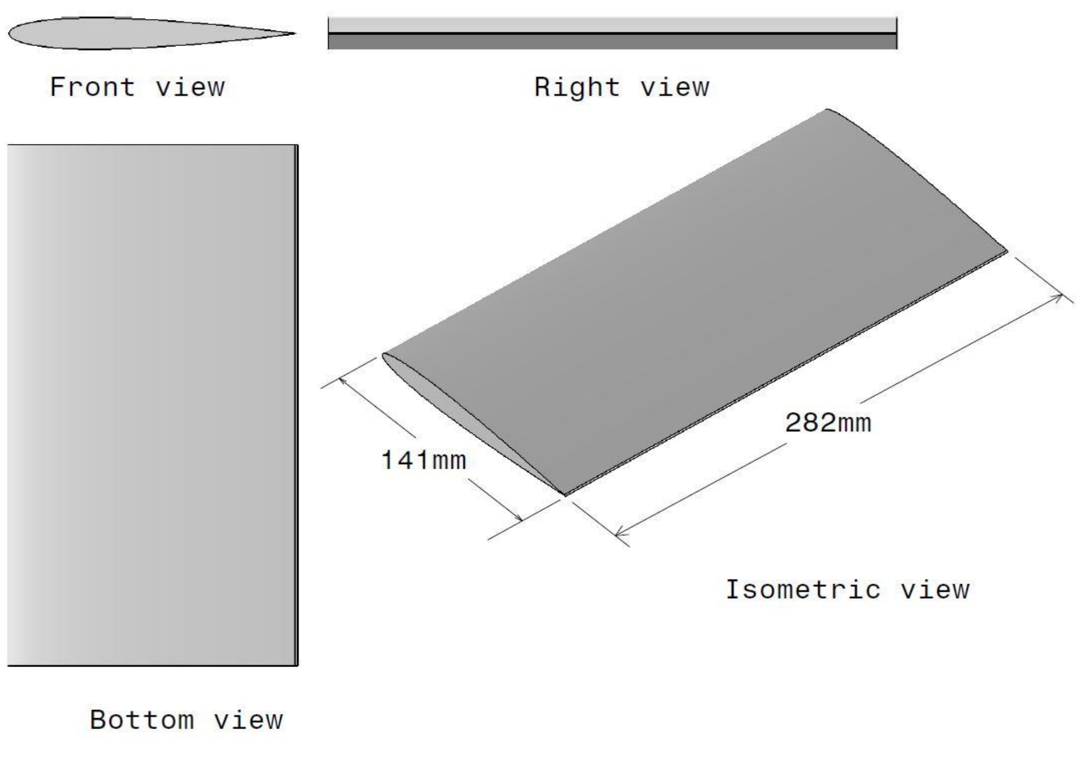

Figure 5.3: Designed wing model of AR 2

5.1.1 Wing Models

NACA 0012 wooden wing models of different aspect ratios are prepared having the equal surface area (40000 mm^2) as shown in figure 5.4, 5.5 and 5.6. Each model is provided with 32 pressure tapings along the span and chord (16 at upper surface and 16 at lower surface). The wings are divided into four equal segments (A, B, C and D) along the span as shown in figure 5.4, 5.5 and 5.6. For wing model of AR 2, the chord length and span length are 141.42 mm and 282.84 mm as shown if figure 5.4, for wing model of AR 1, the chord length at the root and the span length are 200 mm and 200 mm respectively as shown in figure 5.5 and for wing model of AR 0.5, the chord length and span length are 282.84 mm and 141.42 mm respectively as shown in figure 5.6. Four pressure tapping points at upper surface and four pressure tapping points at lower surface are made at 20%, 40%, 60% and 80% of the average chord length of each segment of all the wing models.

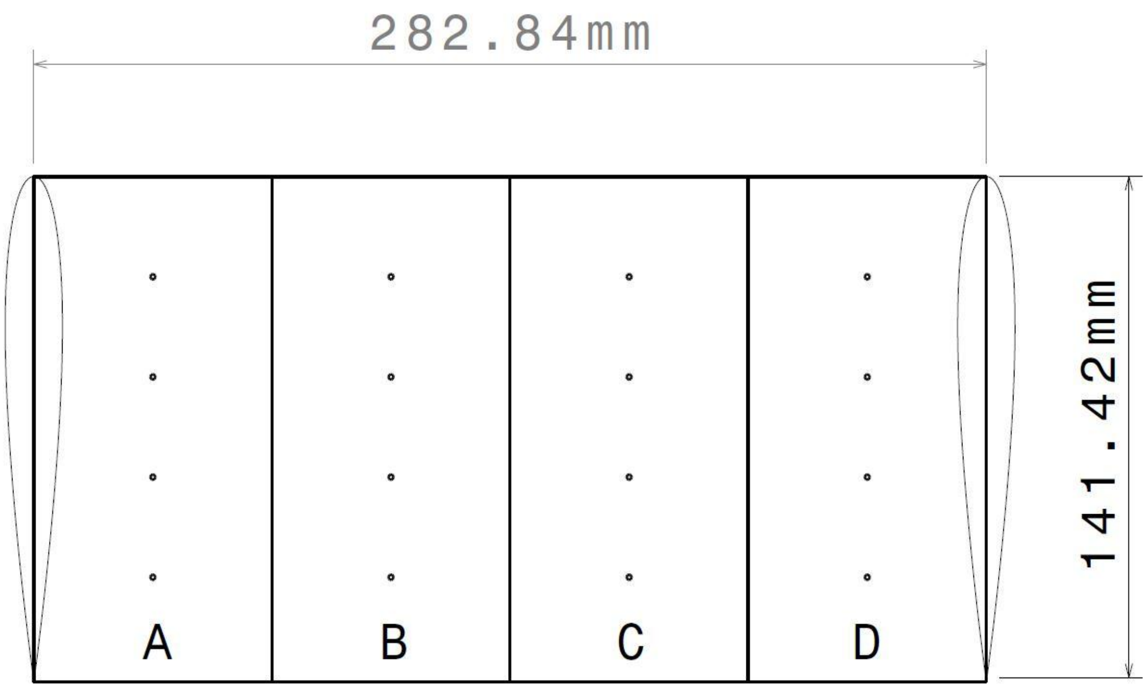

Figure 5.4: Segments representation of wing model of AR 2

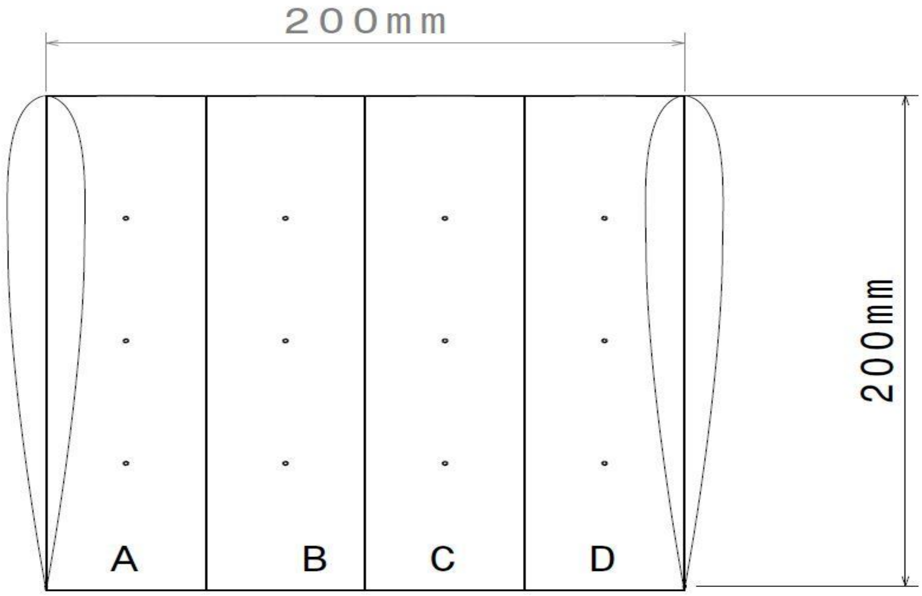

Figure 5.5: Segments representation of wing model of AR 1

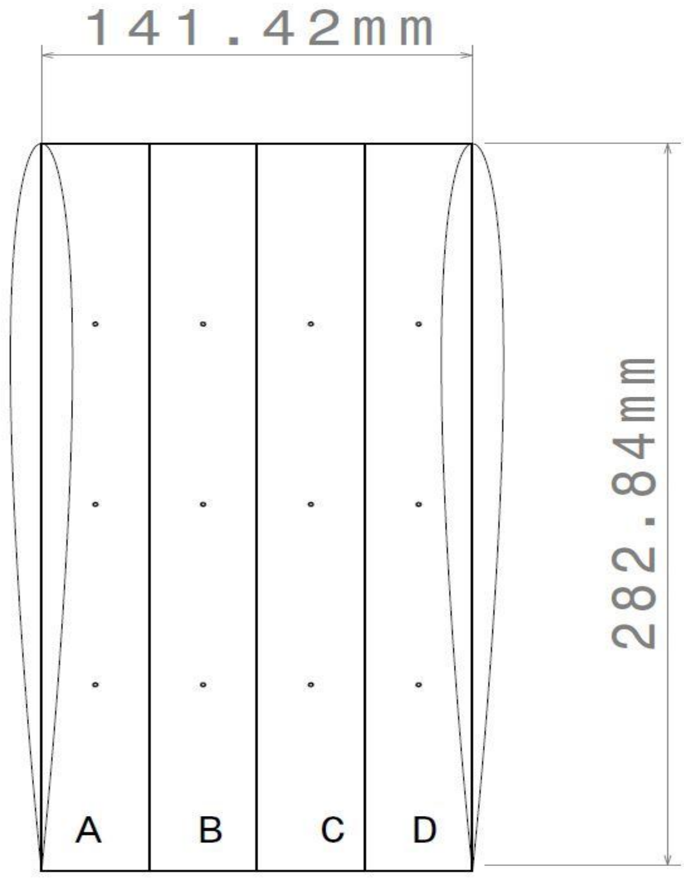

Figure 5.6: Segments representation of wing model of AR 0.5

The optimum wing model of AR 2 is shown in figure 5.7 with backward facing step. Figure 5.7 also shows the dimensions of the backward facing step.

Figure 5.7: Wing model of AR 2 with backward facing step

5.1.2 Pressure Measuring Device

The arrangement of multi-tube manometer for measuring the pressures is shown in figure 5.8. The multi-tube manometer mainly consists of a water tank and 36 manometer glass tubes (in this experiment, 32 glass tubes are used) connected to the tapping points in wing model surfaces. A water tank is used to store the distilled water. Each limb is fitted with a scale graduated in mm to measure the difference of water height. The static pressure is calculated from the difference in water height in glass tube.

Figure 5. 8: Multi-tube Manometer

5.2 Experimental Setup

5.2.1 Wind Tunnel

All the models will be tested at air speed of 135km/h (0.11 Mach) i.e. at Reynolds number 2.92 x 10^5 in the closed-circuit wind tunnel available at the turbulence laboratory, Department of Mechanical Engineering, BUET. The wind tunnel is having the experimental space of 700 mm x 700 mm and the wind speed is created by two 700 mm counter rotating fans. The fans are powered by 400V-3φ-50Hz power supply through a speed controller so that the wind speed in the tunnel can be varied from 30 km/h (0.025 Mach) to 165 km/h(0.137 Mach). At the discharge of the fans there is a silencer to reduce the sound level. From the silencer air flow passes through the flow controlling butterfly valve, diffuser and the plenum chamber to stabilize the flow. The details of wind tunnel are shown in figure 5.9.To perform the experiment in the open-air condition the diffuser at the end of the test section is taken out and the discharge side of the test section is fitted with a 700 mm×700 mm discharge duct. A 1000 mm×1000 mm to 762 mm×762 mm bell mouth entry is added at the return duct to have smooth entry. For this, a 406 mm open flow field created between the discharge duct and bell mouth entry become the experimental space as shown in figure 5.10 where desired velocity is obtained. A fixture is fabricated and fixed in the test section of the wind tunnel. The fixture facilitates the wing models to rotate and fixes at any angle of attack. The wing models are tested at angle of attack from 0˚ to 20˚ with a step of 2˚. Each model is rotated and fixed at the desired angle by seeing the preset scales (in degrees).

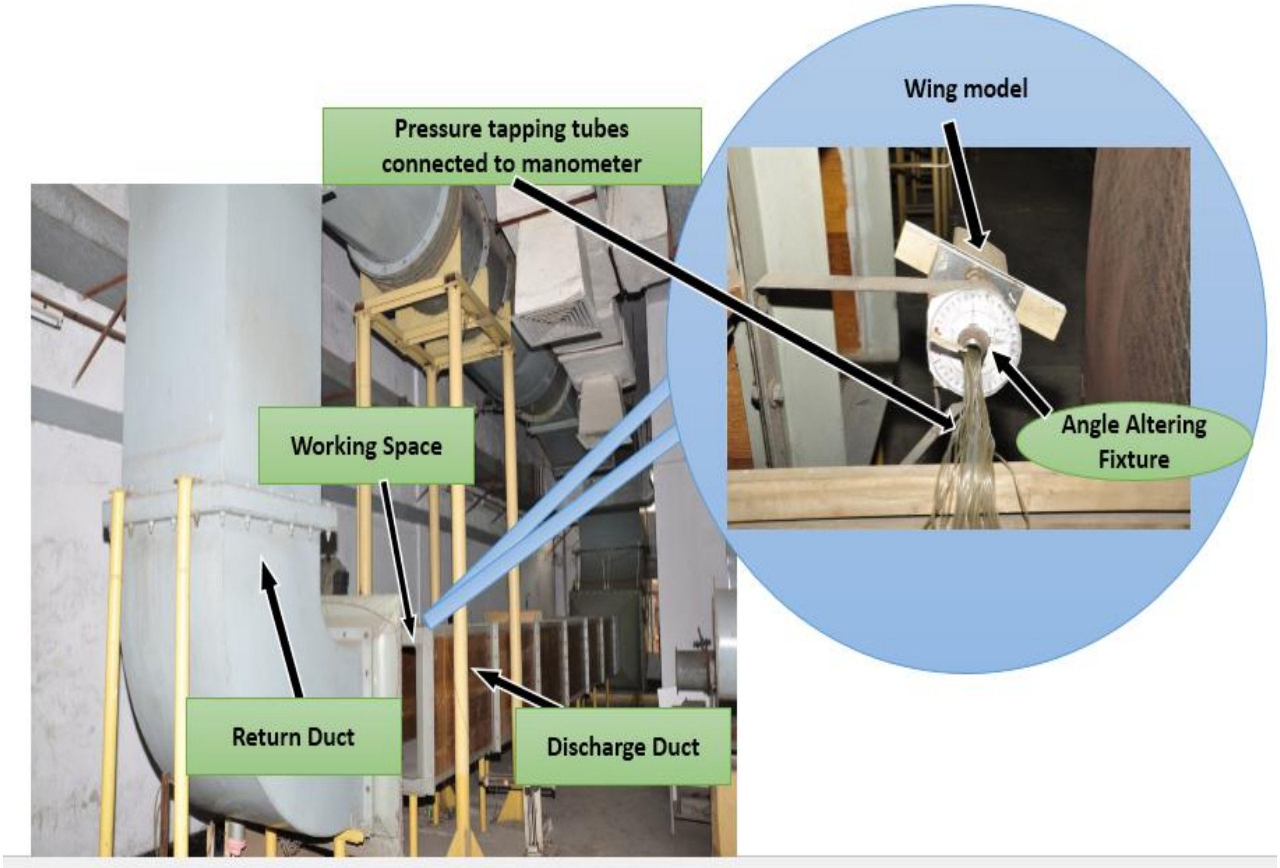

Figure 5. 9: Photograph of Experimental Set-up.

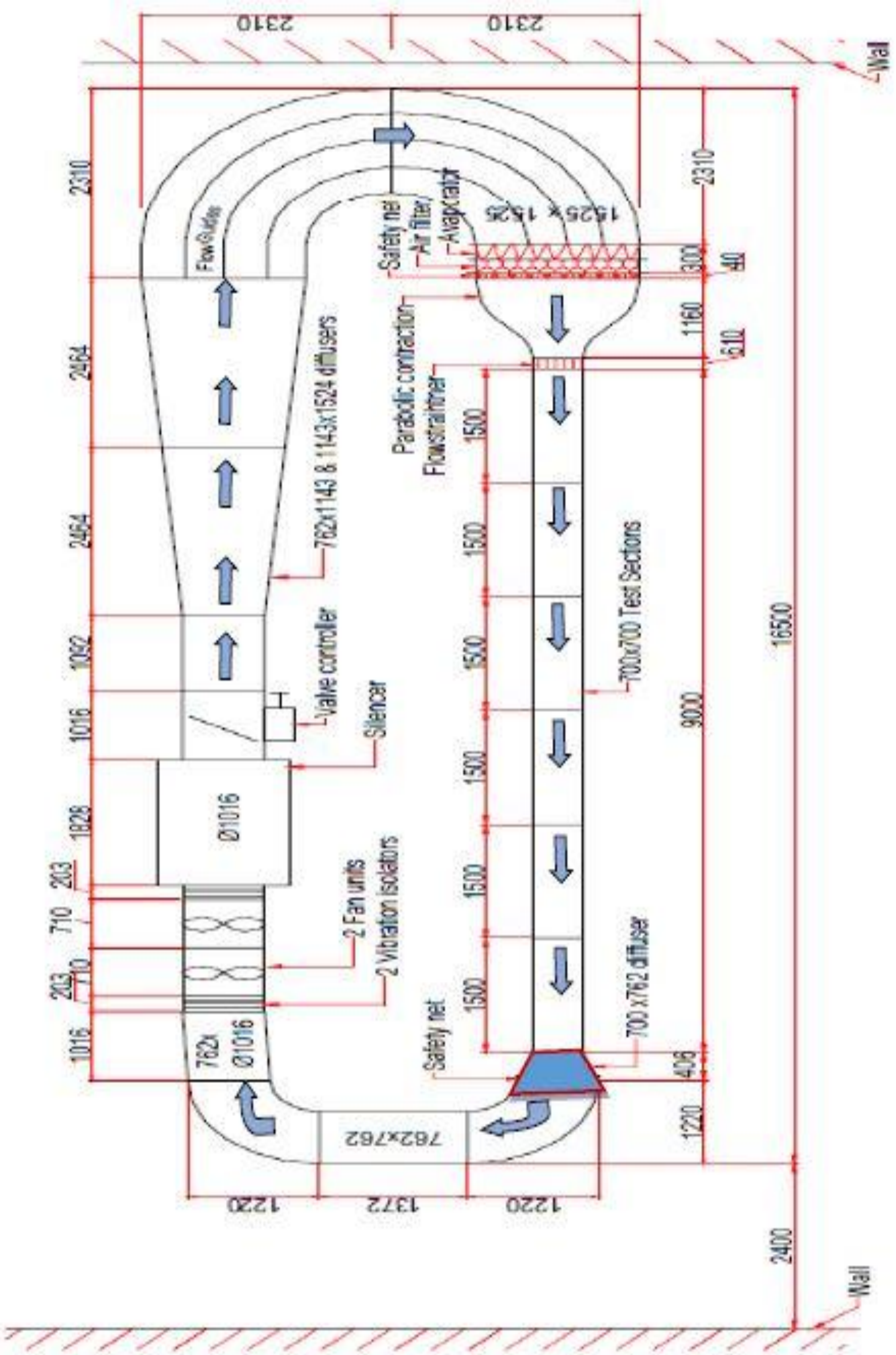

Figure 5. 10: Schematic Diagram of the Wind Tunnel at BUET's Turbulence Lab [31]

5.2.2 Experimental Parameters

All the experimental data are taken at room temperature of 30˚C and at air speed of 37.5 m/s (135 km/h) and the air flow is considered incompressible throughout the experiment. The Reynold number and Mach number are 2.92 X 10^5 and 0.11 respectively. The density of both air and water corresponding to room temperature is 1.164 kg/m^3 and 995.65 kg/m^3 respectively.

5.3 Methodology

At first the wing models of aspect ratio 0.5 has placed in an open space between the test section elements of a 700mm×700mm wind tunnel as shown in figure 5.9.Then the fixture for altering angle of attack has been positioned at 0˚ angle of attack. The 32 pressure tapping tubes were connected to the manometer. The wind tunnel has started and the air velocity increases with the help of a simple knob attached to the frequency inverter. When the manometer water level is at balanced condition then the experimental data are measured. The free stream pressure is calculated by equation 4.1.In this equation the difference of heights are measured from the manometer by using pitot tube. Then the free stream velocity is calculated by using equation 4.2.From the static pressure heights at different points the pressure values for each 32 pressure taps (16 at upper surface and 16 at lower surface) are calculated by equation 4.3.For angle of attack 0˚, from 32 pressure values 32 pressure coefficients are obtained by using equation 4.4 for the four segments of the wing model (A, B, C, D). Each segments contains 8 pressure values and 8 corresponding pressure coefficients (4 at upper surface and 4 at lower surface).To perform experiment on one wing model at one angle of attack it is required more than 2 hours. This same procedure has been done for angle of attack 2˚, 4˚, 6˚, 8˚, 10˚, 12˚, 14˚, 16˚, 18˚ and 20˚. Measuring one wing model data from the wing tunnel testing it is required more than 20 hours. Similar strategy has also performed for other two wing models of AR 1 and AR 2 respectively.

After determining the pressure coefficients at different angles of attack for wing models of different aspect ratios (AR 05, AR 1 and AR 2) the values are analyzed by plotting Cp versus %C. For each wing models at four segments it contains 4 graphs at each angle of attack. So total 44 pressure coefficient distribution graphs are obtained for one wing models. All the pressure coefficients for different wing models of aspect ratios are analyzed to observe the pressure coefficient characteristics. After that from equation (4.23) to (4.26), C_L and C_D of all the wing models of different aspect ratios at every angle of attack are calculated. The coefficient of lift to drag ratio (C_L/C_D) and coefficient of performance (($C_L^{1.5} / C_D$) at different angle of attack for all the wing models are calculated from the value of C_L and C_D at respective angle of attack. The lift characteristics, drag characteristics, coefficient of lift to drag ratio (C_L/C_D) and coefficient of performance ($C_L^{1.5} /C_D$) of the wing models are analyzed and compared with each other to find the optimum wing model. Then similar analysis has been done on the optimum wing model to control the flow separation introducing backward facing step.

6

Chapter Six

RESULTS AND DISCUSSIONS

6.1 Introduction

The pressure coefficients of both upper and lower surfaces of different wing models for different aspect ratios are measured through the wind tunnel testing to analyze aerodynamic characteristics. All the wing models are divided into four segments (A, B, C and D). The pressure coefficients are plotted along chord wise positions (% C) at different angles of attack for each of the four segments (A, B, C and D). The pressure coefficients of the optimum wing with backward facing step are also measured and plotted. Surface pressure distribution of all the wing models are discussed and compared. The data taken from the pressure distribution are used to calculate normal and axial forces on the wing models. These normal and axial forces are used to determine coefficient of lift (C_L), coefficient of drag (C_D), coefficient of lift to drag ratio (C_L / C_D) and coefficient of performance ($C_L^{1.5} / C_D$) [20] of individual wing. Then the effect of angle of attack on C_L, C_D, (C_L / C_D) and ($C_L^{1.5} / C_D$) are studied and used in comparison. From the analysis of coefficient of lift to drag ratio (C_L / C_D) and coefficient of performance ($C_L^{1.5} /C_D$) the optimum wing is found. The passive flow separation of the optimum wing is controlled by introducing backward facing step. Calculated values of pressure coefficients of different wing models from 0˚ to 20˚ angles of attack are shown in Appendix-I. Calculated values of pressure coefficients of optimum wing model with BFS from 0˚ to 20˚ angles of attack are also shown in Appendix-I. The details of uncertainty analysis and data validation are shown in Appendix-II.

6.2 Surface Pressure Distributions

The pressure distributions of both upper and lower surfaces along the chord length of four segments (Segment- A, B, C and D) of three experimental wing models at 0^0, 2^0, 4^0, 6^0, 8^0,10^0,12^0, 14^0, 16^0, 18^0 and 20^0 angle of attack (AOA) are shown in Fig. 6.1 to 6.44. In the figures, the horizontal axis represents the percentage of the chord length (%C) and the vertical axis represents the surface pressure coefficient (Cp). The vertical axis above the zero line (horizontal axis) denotes the negative pressure coefficients or suction pressure coefficients and the vertical axis below the zero line denotes the positive pressure coefficients. All the graphs are discussed in details in the subsequent sub-paragraphs.

6.2.1 Pressure Distributions at 0˚ AOA

Figures 6.1, 6.2, 6.3 and 6.4 represent the surface pressure distribution in terms of pressure coefficient of four segments (A, B, C and D) for AR 0.5, AR 1.0 and AR 2 at 0˚ AOA. In the figures, both upper and lower surface pressure coefficient, Cpu and Cpl are plotted along the chord length (C).

The surface pressure coefficients of segment A at 0˚ are shown in Figure 6.1. It is observed from the graph that the pressure on the wing near the root is negative pressure which is very low for all wing models. Near the leading edge both the upper and the lower surfaces of all the wing models are experiencing the same negative pressure. But after 25% C towards the trailing edge both the upper and lower surfaces pressure coefficients are increasing. It is also observed that both the lower and upper surfaces pressure increase slowly from 20% to 40% C and then increases sharply up to 80% C for all wing models. For all the wing models of different aspect ratios the pressure difference between the upper and lower surfaces are negligible because of symmetricity of the wing models.

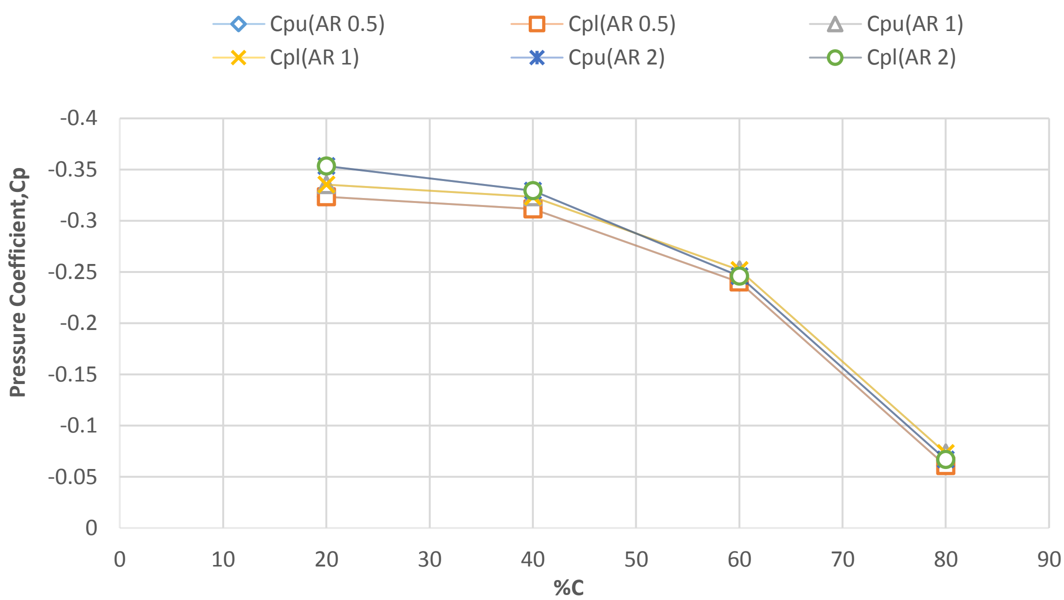

Figure 6.1: Pressure coefficient (C_P) distribution of segment A at 0^0 AOA

Figure 6.2 illustrates the surface pressure coefficients of segment B at 0˚ AOA. It is seen from the graph that the pressure on the wing near the root is negative pressure which is very low for all wing models. Near the leading edge both the upper and the lower surfaces of all the wing models are experiencing the same negative pressure because of symmetricity. But after 25% C towards the trailing edge both the upper and lower surfaces pressure coefficients are increasing. It is also observed that both the lower and upper surfaces pressure increases slowly from 20% to 40% C and then increases sharply up to 80% C for all wing models. Among all the wings of different aspect ratios, the wing model of aspect ratio 2 shows the greatest pressure differences. For all the wing model of different aspect ratios the pressure difference between the upper and lower surfaces are negligible and it is almost same for all the wing models.

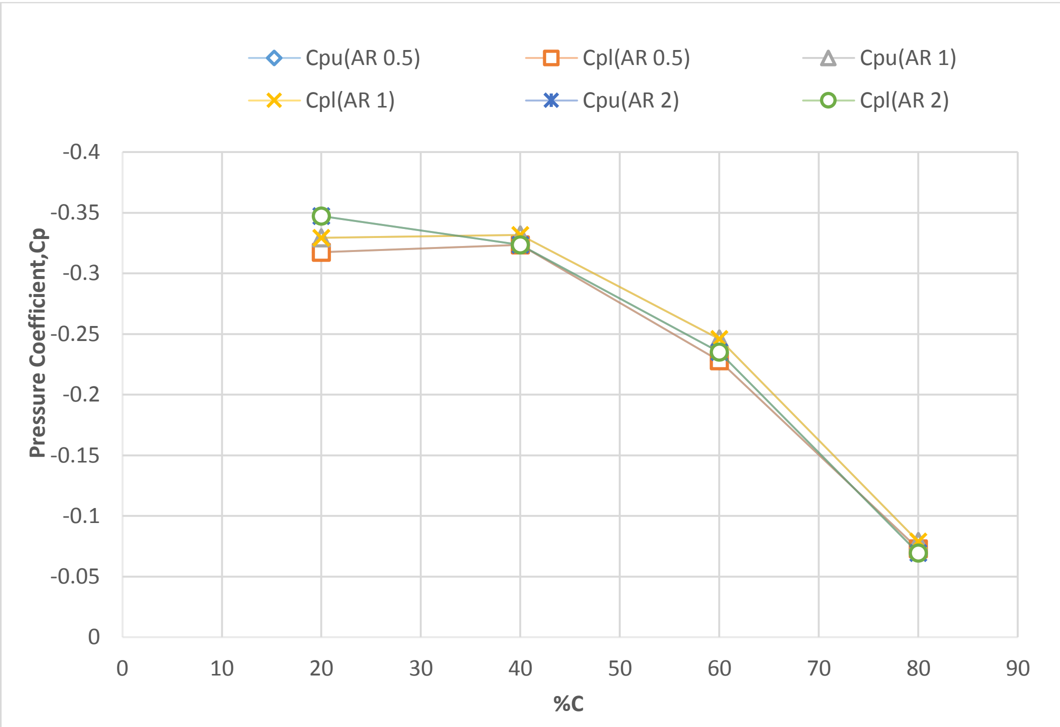

Figure 6.2: Pressure coefficient (C_p) distribution of segment B at 0^0 AOA

Figure 6.3 shows the upper and lower surface pressure distribution of segment C at 0˚ AOA. The pressure on the wing near the root is negative pressure for all the wing models. Near the leading edge both the upper and the lower surfaces of all the wing models are experiencing the same negative pressure because of symmetricity. But after 25% C towards the trailing edge both the upper and lower surfaces pressure coefficients are increasing. It is also observed that both the lower and upper surfaces pressure increase slowly from 20% to 40% C and then increases sharply up to 80% C for all wing models. From the graph it is seen that the wing model of aspect ratio 2 shows the greatest pressure differences. For all the wing model of different aspect ratios the pressure difference between the upper and lower surfaces are negligible and it is almost same for all the wing models because of symmetricity of the wing models.

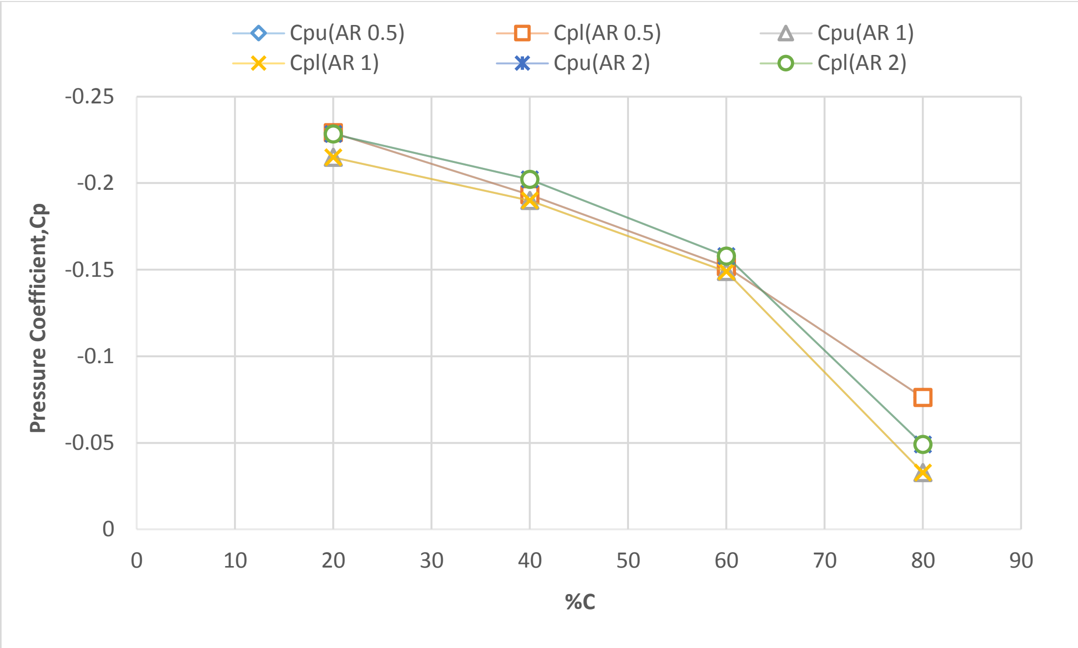

Figure 6.3: Pressure coefficient (C_P) distribution of segment C at 0^0 AOA

The surface pressure coefficients of segment D at 0˚ AOA are shown in Figure 6.4. It is observed from the graph that the pressure on the wing near the root at 20%C is negative pressure which is very low for all wing models. The upper and lower surfaces of all the wing models of different aspect ratios are experiencing the same negative pressure near the leading edge. But after 25% C towards the trailing edge both the upper and lower surfaces pressure coefficients are increasing. Both the lower and upper surfaces pressure of the different wing models increases slowly from 20% to 40% C and then increases sharply up to 80% C for all wing models. From the graph, it is seen that the pressure difference between the upper and lower surface is slightly greater for wing of aspect ratio 2 than other two wind models. But for all the wing models of different aspect ratios the pressure difference between the upper and lower surfaces are negligible because of symmetricity of the wing models.

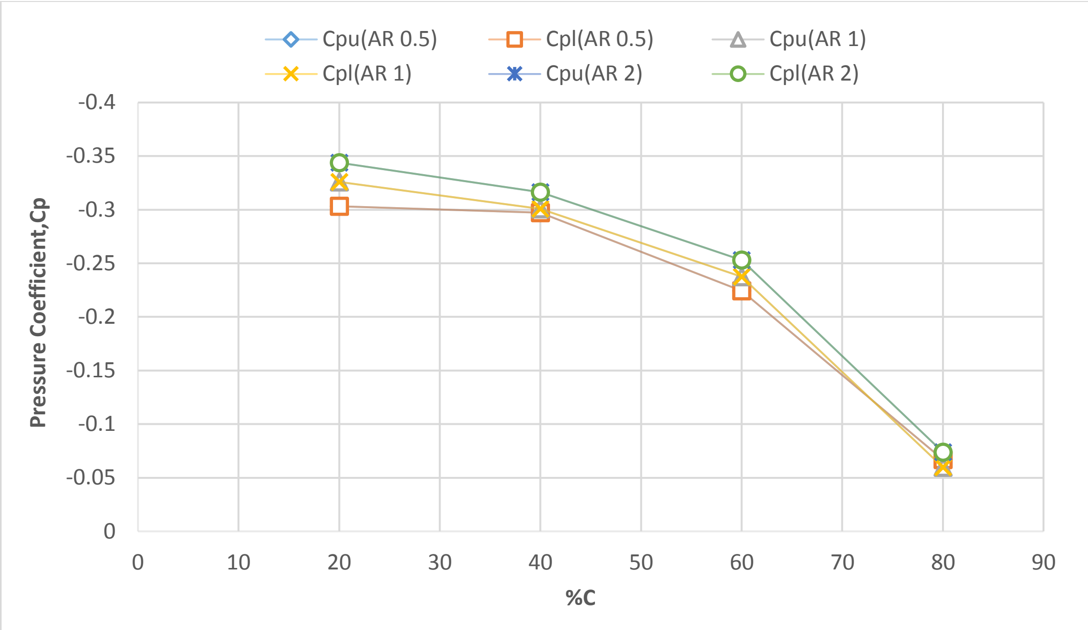

Figure 6.4: Pressure coefficient (C_p) distribution of segment D at 0^0 AOA

6.2.2 Pressure Distributions at 2˚ AOA

Figures 6.5, 6.6, 6.7 and 6.8 represent the surface pressure distribution in terms of pressure coefficient of four segments (A, B, C and D) of wing for different aspect ratios at 2˚AOA. In the figures, both upper and lower surface pressure coefficient, C_{pu} and C_{pl} are plotted along the chord length (C).

In figure 6.5, the surface pressure distributions for segment-A of the wing models at 2˚ AOA are shown. It is observed that upper surfaces of four wing models are having higher negative pressure than the lower surfaces. The upper surface pressures for all wing models increase gradually towards the trailing edge. Among the four wing models, the upper surface pressure is lowest for the wing with AR 2 and highest for wing with AR 0.5. For all the wing of different aspect ratios, the lower surface pressures are almost same. The lower surface pressure for wing of AR 2 is highest among all of the wing models. For all the wing models the lower surface pressure decrease slowly from 20% C to 40% C and then decreases gradually up to the trailing edge. For wing of AR 1 the lower surface pressure is lowest among all of the wing models and it decreases slowly from leading edge to trailing edge. The pressure difference between upper and lower surfaces for wing of AR 2 is highest and then this difference decreases gradually towards the trailing edge. For all the wing models the difference between upper and lower surface becomes maximum at 20% C.

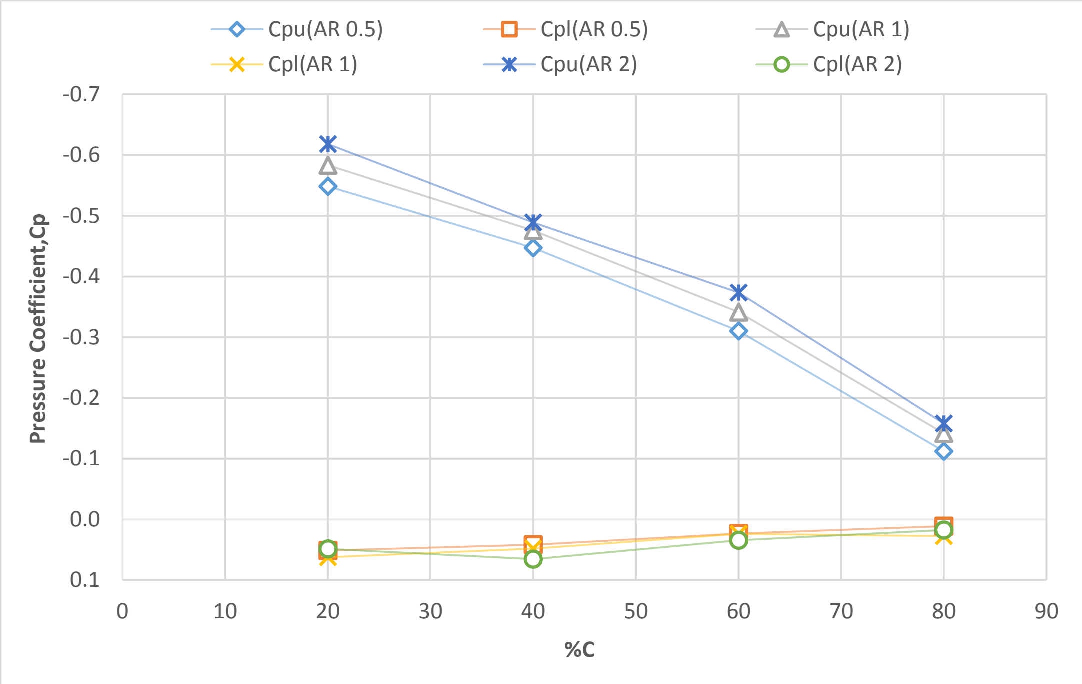

Figure 6.5: Pressure coefficient (C_p) distribution of segment A at 2^0 AOA

In figure 6.6, the surface pressure distributions for segment-B of the wing models at 2˚ AOA are shown. From the figure, it is seen that upper surfaces of four wing models are having higher negative pressure than the lower surfaces. The upper surface pressures for all wing models increase gradually towards the trailing edge from 20%C to 80%C. Among the four wing models, the upper surface pressure is lowest for the wing with AR 2 and highest for wing with AR 0.5. The lower surface pressures are almost same for all the wing of different aspect ratios. The lower surface pressure for wing of AR 2 is highest among all of the wing models and it decreases gradually from 20%C to 80%C. For all the wing models the lower surface pressure decrease slowly from 20% C to 40% C and then decreases gradually up to the trailing edge. For wing of AR 1 the lower surface pressure is lowest up to 40%C among all of the wing models and it decreases slowly from leading edge to trailing edge. From 60%C to 80%C the lower surfaces pressure of all the wing models almost remain same. It is seen that the pressure difference between upper and lower surfaces for wing of AR 2 is highest and then this difference decreases gradually towards the trailing edge. The difference between upper and lower surface becomes maximum at 20% C and it is greater than the previous segment A's pressure differences.

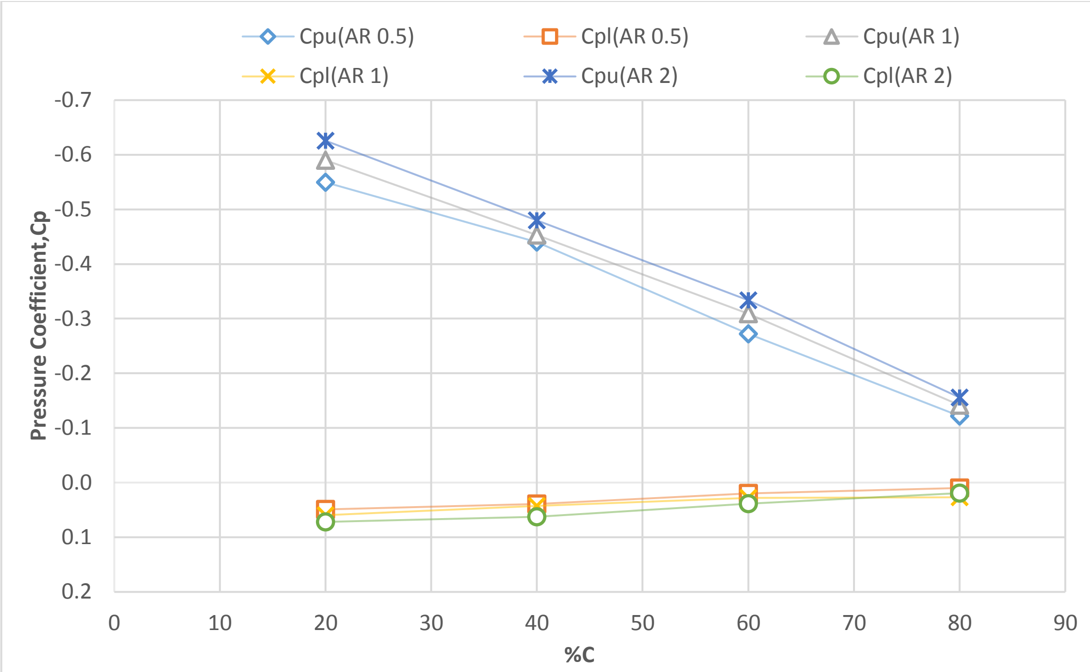

Figure 6.6: Pressure coefficient (C_p) distribution of segment B at 2^0 AOA

In figure 6.7, for segment-C the surface pressure distributions of the wing models at 2° AOA are shown. It is found that upper surfaces of four wing models are having higher negative pressure than the lower surfaces. Among the four wing models, the upper surface pressure is lowest for the wing with AR 2 and highest for wing with AR 0.5. The upper surface pressures for all wing models increase gradually towards the trailing edge from 20%C to 80%C. The lower surface pressures are almost same for all the wing of different aspect ratios. From the figure it is found that the lower surface pressure for wing of AR 2 is highest among all of the wing models and it decreases gradually from 20%C to 80%C. For all the wing models the lower surface pressure decrease slowly from 20% C to 40% C and then decreases gradually up to the trailing edge. For wing of AR 1 the lower surface pressure is lowest up to 40%C among all of the wing models and it decreases slowly from leading edge to trailing edge. The lower surfaces pressure of all the wing models almost remain same from 60%C to 80%C. It is seen that the pressure difference between upper and lower surfaces for wing of AR 2 is highest and then this difference decreases gradually towards the trailing edge. The difference between upper and lower surface becomes maximum at 20% C and it is greater than the previous segment C's pressure differences.

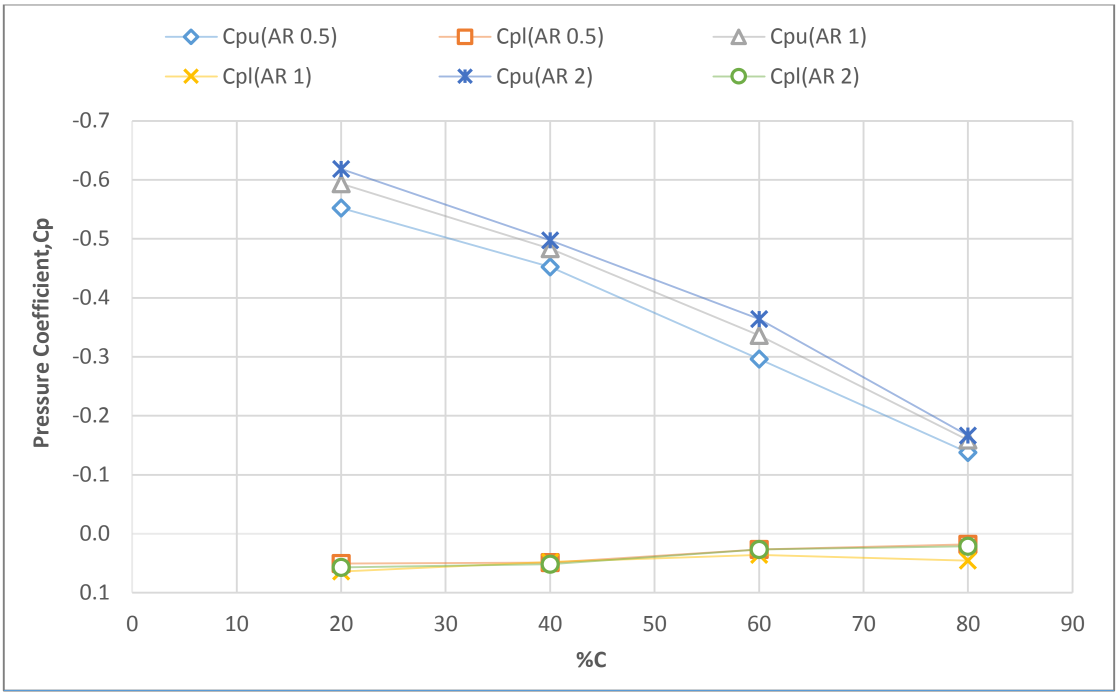

Figure 6.7: Pressure coefficient (C_p) distribution of segment C at 2^0 AOA

Figure 6.8 shows the surface pressure distributions for segment-D of the wing models at 2˚ AOA. From the figure, it is seen that upper surfaces of four wing models are having higher negative pressure than the lower surfaces. The upper surface pressures for all wing models increase gradually towards the trailing edge from 20%C to 80%C. Among the four wing models, the upper surface pressure is lowest for the wing with AR 2 and highest for wing with AR 0.5. The lower surface pressures are almost same for all the wing of different aspect ratios. The lower surface pressure for wing of AR 2 is highest among all of the wing models and it decreases gradually from 20%C to 80%C. For all the wing models the lower surface pressure decrease slowly from 20% C to 40% C and then decreases gradually up to the trailing edge. For wing of AR 1 the lower surface pressure is lowest up to 40%C among all of the wing models and it decreases slowly from leading edge to trailing edge. From 60%C to 80%C the lower surfaces pressure of all the wing models almost remain same. It is seen that the pressure difference between upper and lower surfaces for wing of AR 2 is highest but it is smaller than the previous segment C. Similarly as other's segment the difference between upper and lower surface becomes maximum at 20% C and it is lower than the previous segment C's pressure differences.

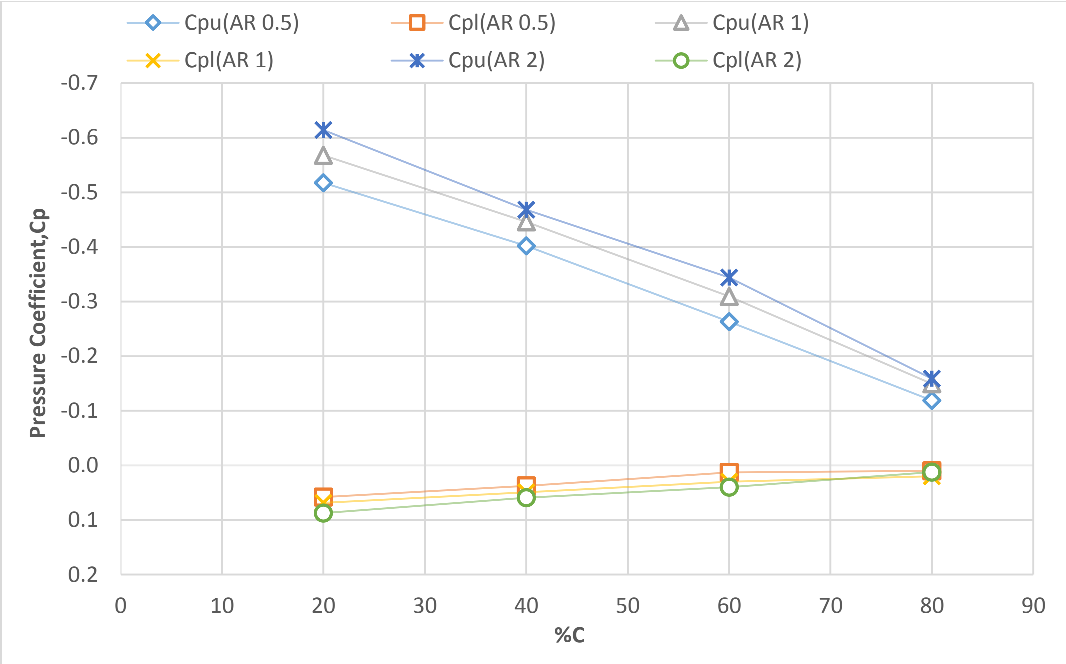

Figure 6.8: Pressure coefficient (C_p) distribution of segment D at 2^0 AOA

6.2.3 Pressure Distributions at 4˚ AOA

Figures 6.9, 6.10, 6.11 and 6.12 represent the surface pressure distribution in terms of pressure coefficient of four segments (A, B, C and D) of wing for different aspect ratios at 4˚ AOA. In the figures, both upper and lower surface pressure coefficient, C_{pu} and C_{pl} are plotted along the chord length (C).

From figure 6.9, it is observed that pressure difference between the upper and lower surface of wing for AR 2 of segment A is highest amongst all the three wing models. The lower surface pressure for all wing models are almost same after 40%C.But it is seen that for wing models of AR 2 the lower surface pressure is higher than other two wing models up to 40%C.After that for all wing models lower surface pressure decrease gradually. It is also observed that the pressure difference between the two surfaces of wing for AR 0.5 is the lowest as it’s the upper surface pressure is lower than that of other wing models.

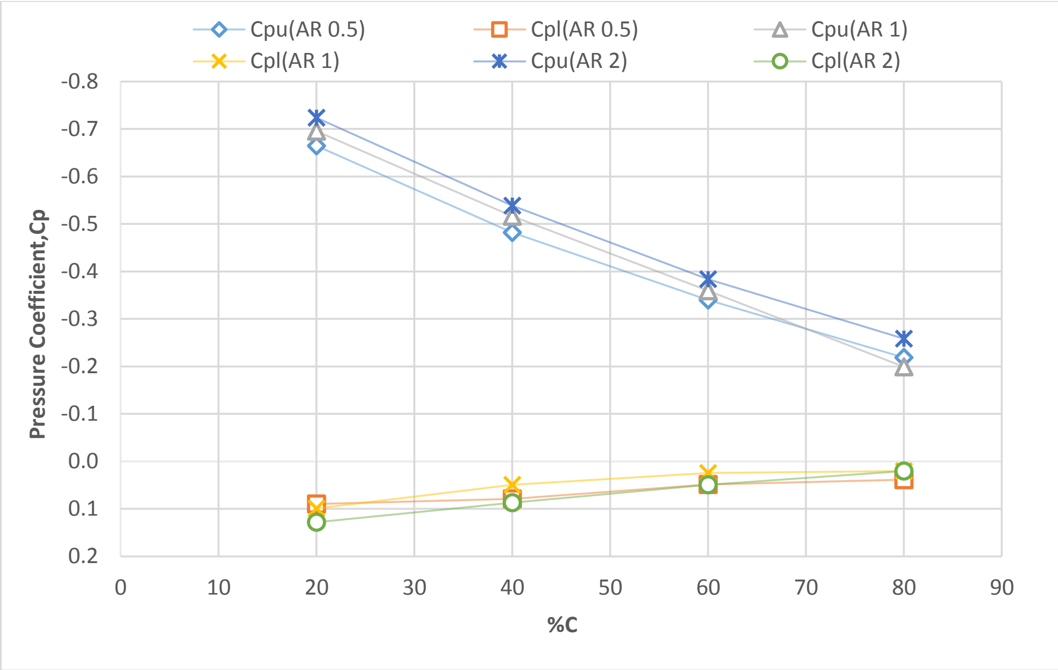

Figure 6.9: Pressure coefficient (C_p) distribution of segment A at 4^0 AOA

In figure 6.10, for segment B it is observed that the upper surface of all wing models is having higher negative pressure than the lower surface of the respective wing model. The difference between upper and lower surface pressure is observed lowest for wing of AR 2. The upper surface pressure for all the wing models increases from leading edge to trailing edge. The upper surface pressure for wing of AR 0.5 is lowest amongst three wing models, highest for wing of AR 2 and in between these two for wing of AR 1. The lower surface for wing of AR 2 is having higher positive pressure than that of other three wing models. The pressure difference between upper and lower surfaces for wing of AR 2 is highest amongst all of the wing models. It also observed that for segment B the pressure difference between upper and lower surfaces are greater than segment A for all wing models.

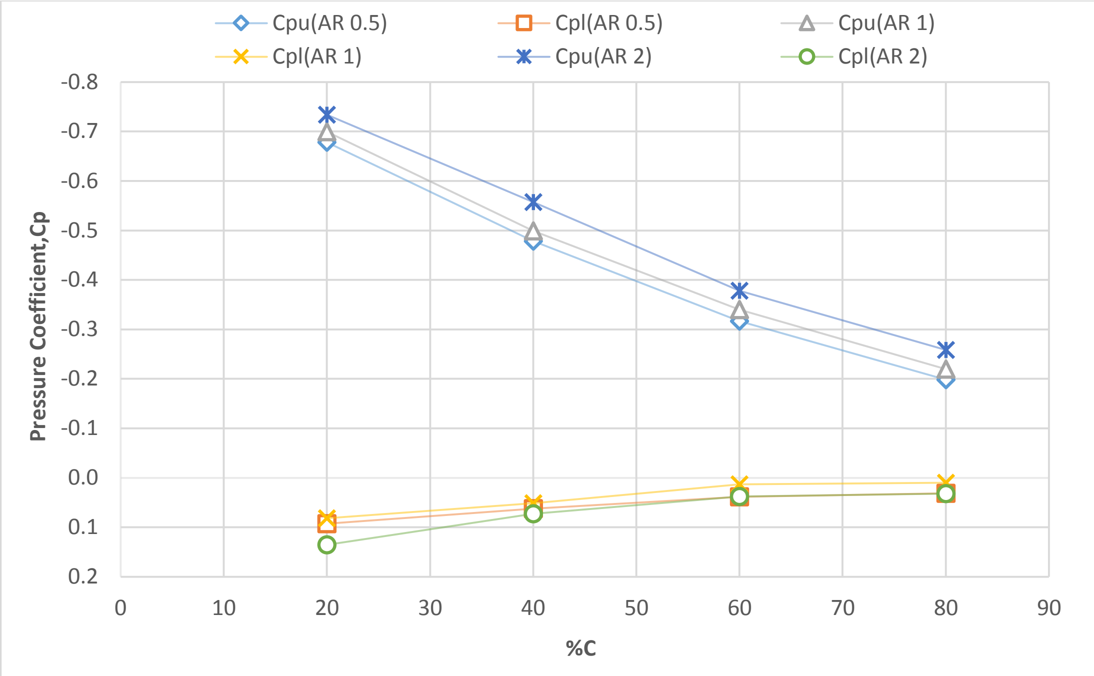

Figure 6.10: Pressure coefficient (C_p) distribution of segment B at 4^0 AOA

Figure 6.11 shows the pressure distribution for segment-C of wing models. From the figure, it is observed that the upper surface suction pressure is lowest for wing of AR 1 and highest for the wing of AR 2. The lower surface pressures of all the wing models remain at the positive pressure side throughout the chord length and are close to each other but highest value is obtained for wing of AR 2. As a result, the pressure difference between the upper and lower surface of the wing of AR 2 is highest. It is also observed that the pressure differences for all wing models of segment C is greater than the differences of segment B.

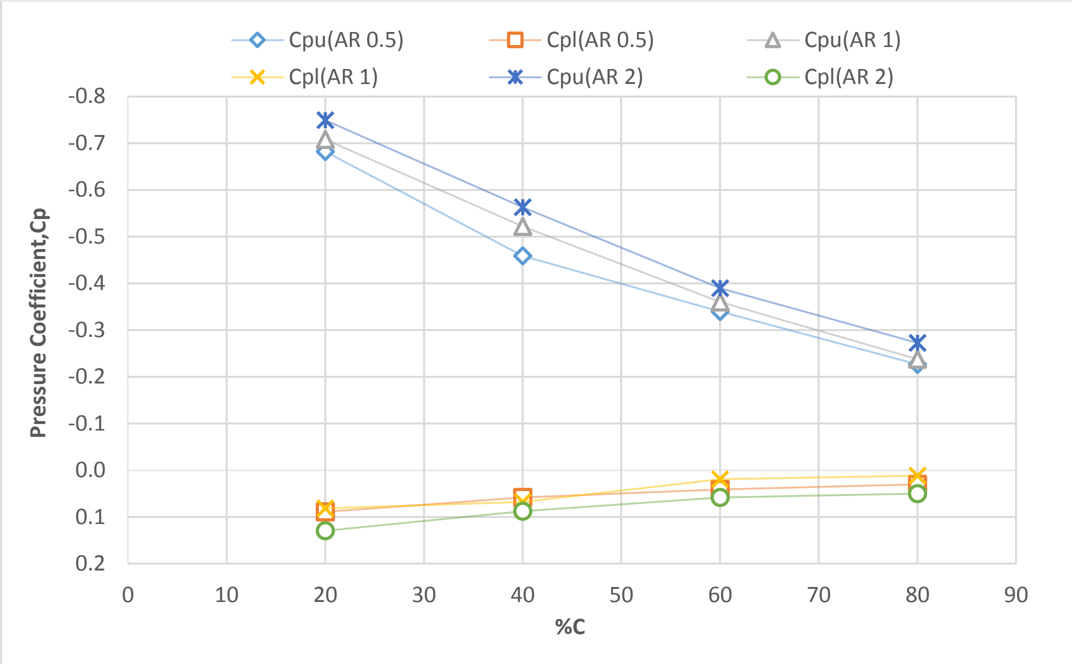

Figure 6.11: Pressure coefficient (C_p) distribution of segment C at 4^0 AOA

In figure 6.12, almost similar type of pressure distribution of wing models for segment D is observed as in segment C. At segment D as well, the difference between upper and lower surface is observed maximum for wing of AR 2. But the pressure difference between two surfaces of respective wing models is higher than that of segment C.

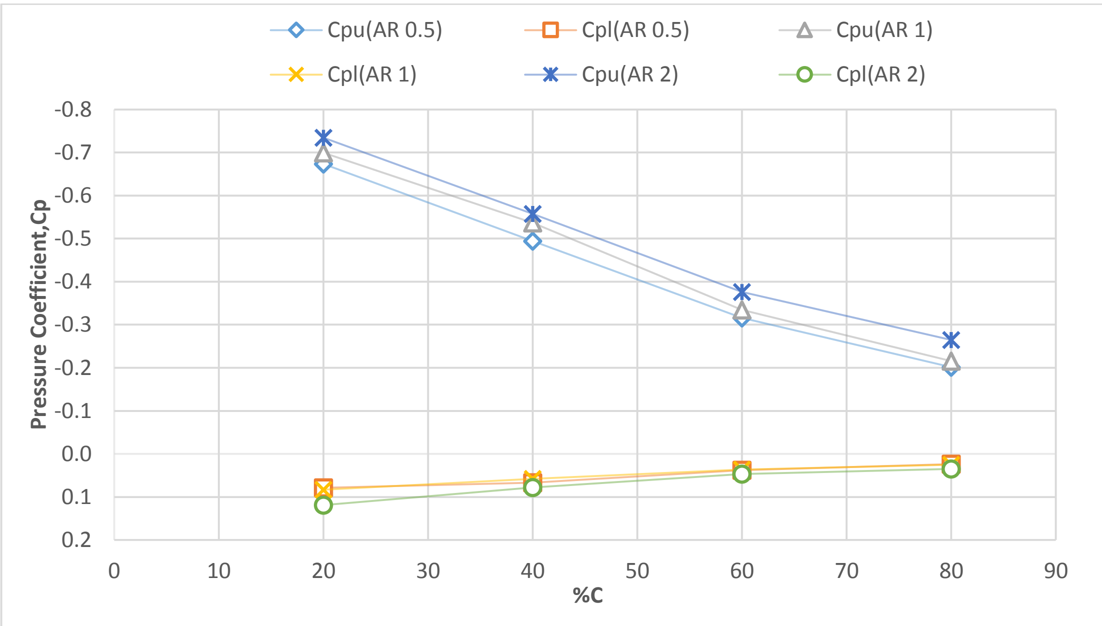

Figure 6.12: Pressure coefficient (C_p) distribution of segment D at 4^0 AOA

6.2.4 Pressure Distributions at 6˚ AOA

Figures 6.13, 6.14, 6.15 and 6.16 represent the surface pressure distribution in terms of pressure coefficient of four segments (A, B, C and D) of wing models with different aspect ratios (0.5, 1, 2) at 8˚ AOA.

The surface pressure distributions for segment-A of wing models of different aspect ratios at 6˚ angle of attack are shown in Figure 6.13. From the figure it is seen that the upper surface of all wing models are having higher negative pressure than the lower surface pressure of the respective wing models. For all wing models, upper surface pressure increases gradually from leading edge to trailing edge. But lower surface pressure decreases slowly from leading edge to trailing edge. The upper surface pressure is observed to be lowest for wing of AR 2 and highest for wing of AR 0.5. But the lower surface pressure is almost same for all of the wing models of different aspect ratios. From the graph it is shown that the lower surface pressure coefficient differs largely up to 40%C and after that their differences become negligible up to 80%C.As a result, the difference between the upper and lower surface pressure of wing of AR-2 becomes highest among three wing models of different aspect ratios. For all wing models, the largest difference between upper and lower surface is observed from 20% C to 40%C.

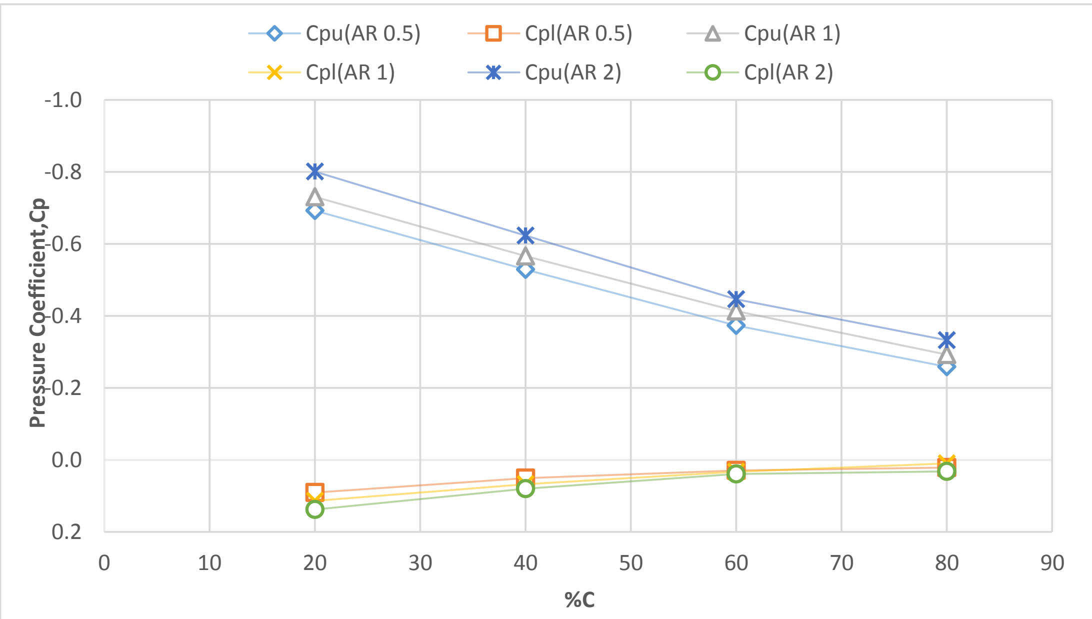

Figure 6.13: Pressure coefficient (C_p) distribution of segment A at 6^0 AOA

In Figure 6.14, the surface pressure distribution of segment B of wing models at 6° AOA is illustrated. It is observed that the upper surface of all wing models are having higher negative pressure than lower surface of the respective wing models. The difference between upper and lower surface pressure is observed lowest for wing of AR 2 and highest for wing of AR 0.5. The upper surface pressures for all wing models increase from 20% C to 80% C. But lower surface pressures decrease from leading edge to trailing edge. It is seen from the graph that the lower surface pressure decreases slowly from 60%C to 80%C. The upper surface pressure for wing of AR 2 is highest and lowest for wing of AR 0.5 among three wing models. Between the wing of AR 1 and wing of AR 2, the upper surface pressure is lower for wing of AR 1. The lower surface pressure for wing of AR 2 is slightly higher than that of other three wing models. The highest pressure difference is also obtained for wing of AR 2 and the difference is highest at 20%C.

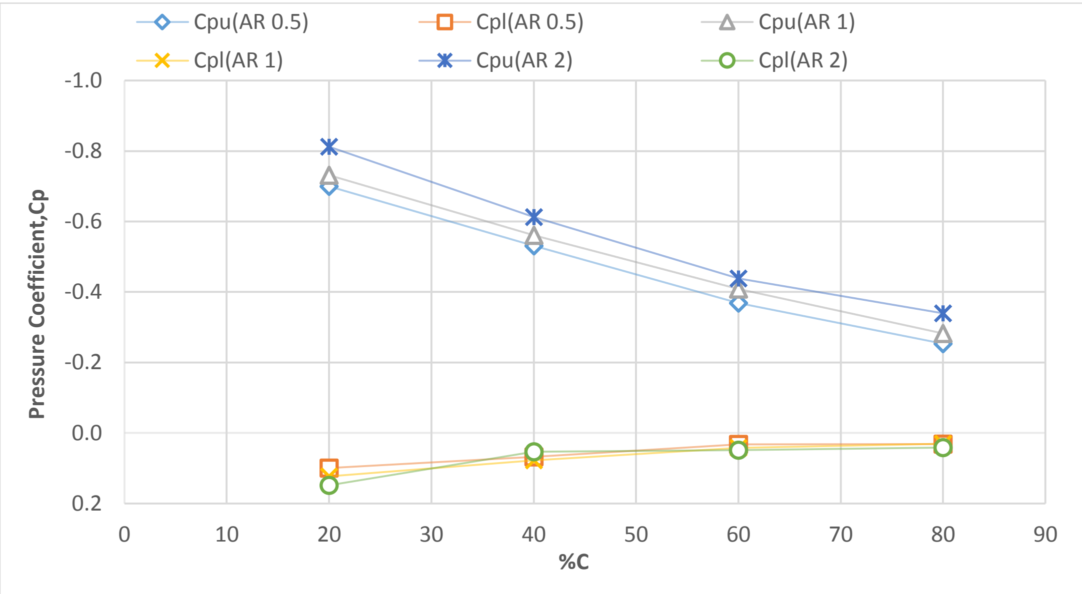

Figure 6.14: Pressure coefficient (C_p) distribution of segment B at 6^0 AOA

Figure 6.15 shows the pressure distribution of segment-C of wing models respectively. From the figure 6.15, it is observed that upper surface pressure of all wing models increases from leading edge to trailing edge in segment-C. But lower surface pressures decrease from leading edge to trailing edge. It is also seen that the upper surface pressure is lowest for wing of AR 2 throughout the chord and highest for wing of AR 0.5. But the lower surface pressure of all the wing models is almost same and is highest for wing of AR 2 amongst three wing models. These differences of pressure coefficient are observed clearly up to 40%C and then it decreases slowly from 40%C to 80%C. As a result, the pressure difference between the upper and lower surface of wing of AR 2 is also at the highest level. Besides, the upper and lower surface pressure differences for wing of AR 2 is higher than other wing models. It is also seen that these differences are greater than the segment-B's differences.

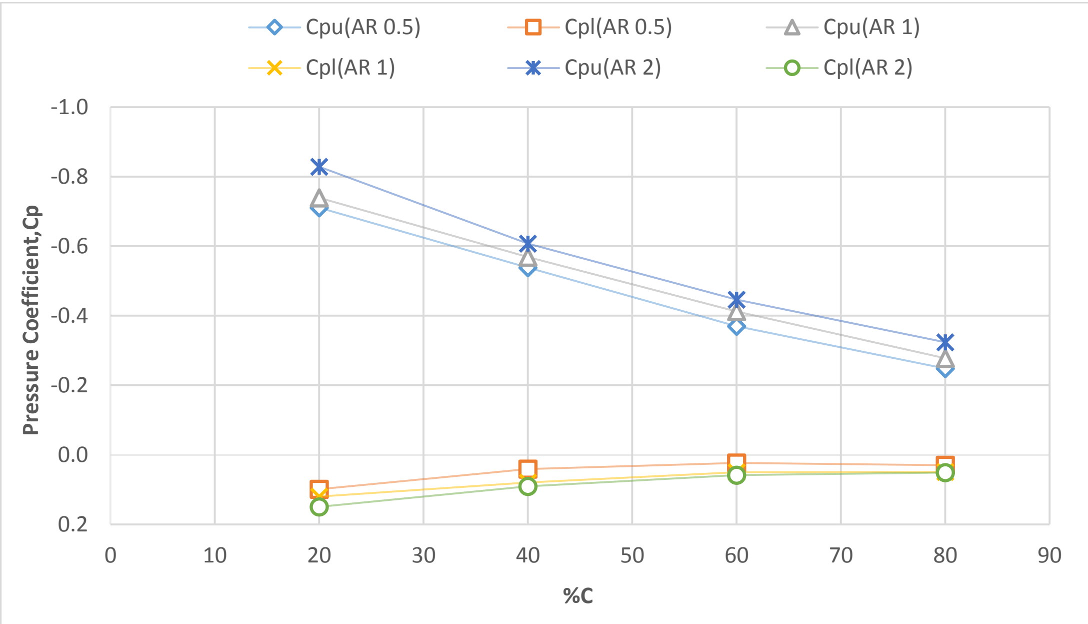

Figure 6.15: Pressure coefficient (C_p) distribution of segment C at 6^0 AOA

The surface pressure distributions for segment-D of wing models of different aspect ratios at 6˚ angle of attack are shown in figure 6.16. From figure, it is observed that the difference between upper and lower surface pressures in segment-D is highest for wing of AR 2. In segment-D, the pressure difference between two surfaces of respective wing models are lower than those of segment-C. The difference between upper and lower surfaces for all wing models become maximum at 20% C and lowest at 80%C.

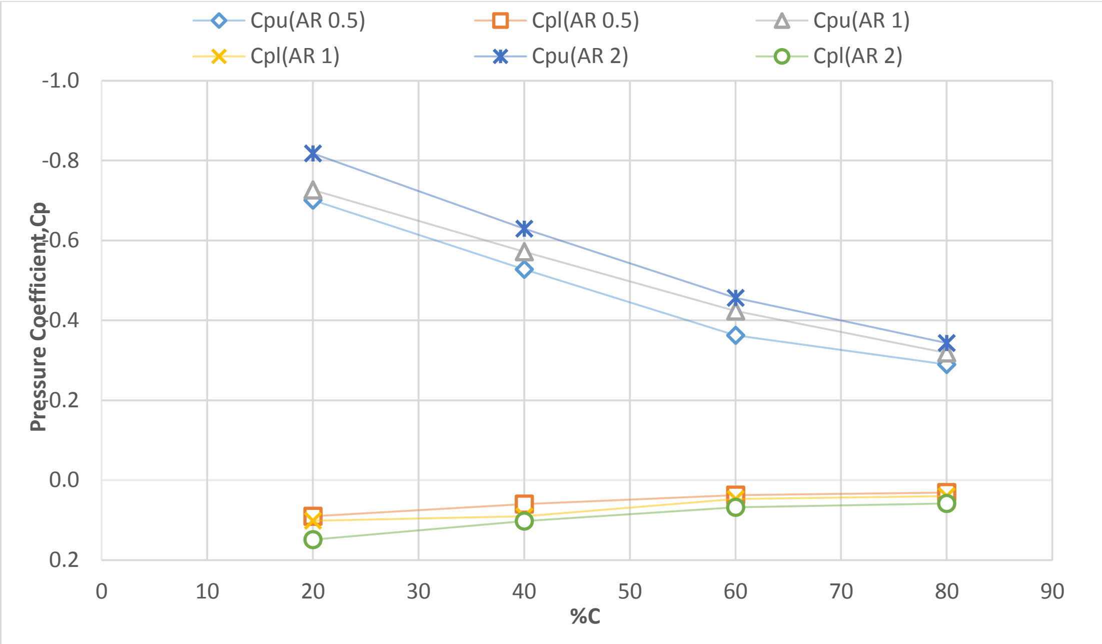

Figure 6.16: Pressure coefficient (C_p) distribution of segment D at 6^0 AOA

6.2.5 Pressure Distributions at 8˚ AOA

Figures 6.17, 6.18, 6.19 and 6.20 represent the surface pressure distribution in terms of pressure coefficient of four segments (A, B, C and D) of wing with different AR at 8˚ AOA.

The surface pressure distributions for segment-A of wing models at 8˚ angle of attack are shown in Figure 6.17. It is noticed that the upper surface of all wing models are having higher negative pressure than the lower surface pressure of the respective wing models. For all wing models, upper surface pressure increases gradually from 20%C to 80%C. But lower surface pressure decreases slowly from leading edge to trailing edge. The upper surface pressure is observed to be highest for wing of AR .5 and lowest for wing of AR 2. But the lower surface pressure is almost same for wing of AR 0.5 and wing of AR 1.The greatest lower surface pressure is obtained for wing of AR 2. As a result, the difference between the upper and lower surface pressure of wing of AR 2 becomes highest among three wing models. For all wing models, the largest difference between upper and lower surface is observed at 20% C. The difference is decreasing gradually from leading edge to trailing edge and it is lowest at 80%C.

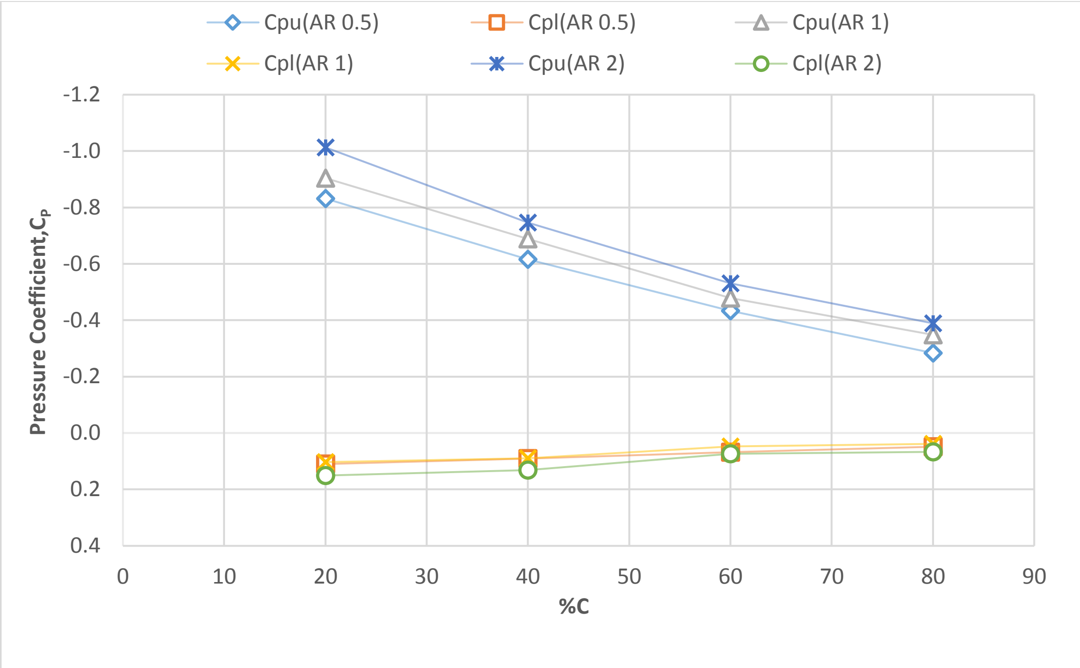

Figure 6.17: Pressure coefficient (C_p) distribution of segment A at 8^0 AOA

The surface pressure distributions for segment-B of wing models at 8˚ angle of attack are shown in figure 6.18.From the graph, it is seen that the upper surface of all wing models are experiencing higher negative pressure than the lower surface pressure of the respective wing models. For all wing models, upper surface pressure increases gradually from leading edge to trailing edge. But lower surface pressure decreases slowly from 20%C to 80%C. The upper surface pressure is observed to be highest for wing of AR 0.5 and lowest for wing of AR 2. But the lower surface pressure is almost same for wing models of AR 1 and AR 0.5. It is seen from the graph that the pressure differences of segment B is greater than the pressure differences of segment A. The greatest lower surface pressure is obtained for wing of AR 2 at 20%C. The difference between the upper and lower surface pressure of wing of AR 2 becomes highest among three wing models. For all the wing models, the lower surface pressure differences are decreasing gradually from leading edge to trailing edge and the lowest pressure difference is obtained at 80%C.

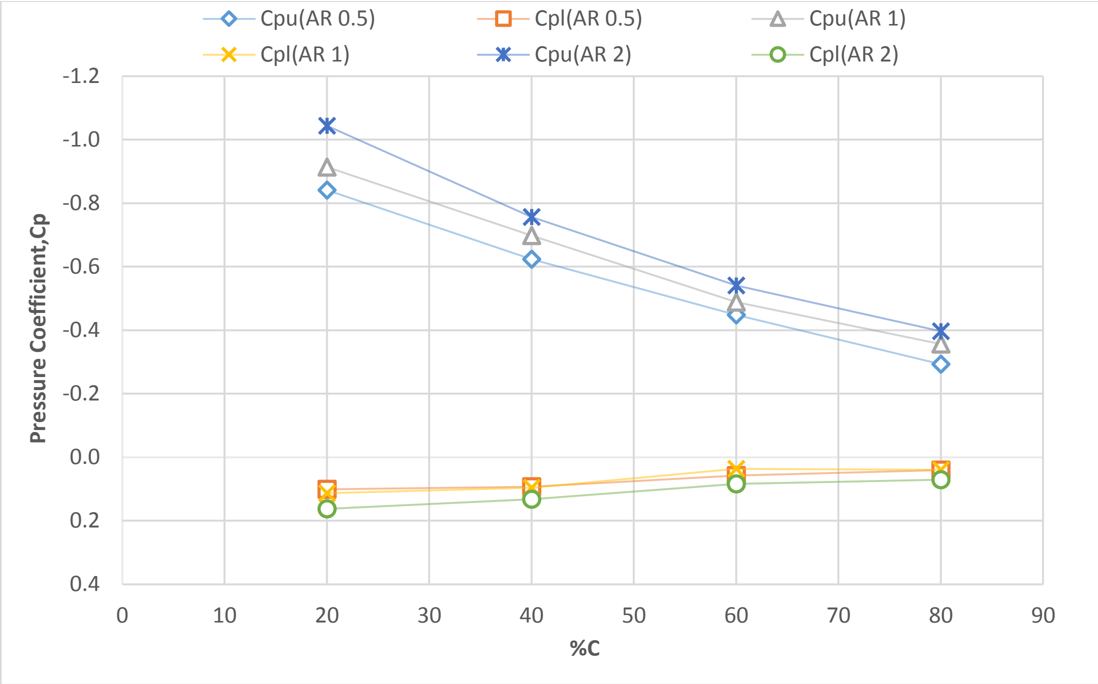

Figure 6.18: Pressure coefficient (C_p) distribution of segment B at 8^0 AOA

Figure 6.19 shows the pressure distribution of segment-C of three wing models respectively. From the figure 6.15, it is observed that upper surface pressure of all wing models increase from leading edge to trailing edge in segment-C. But lower surface pressures decrease from leading edge to trailing edge. It is also seen that the upper surface pressure is lowest for wing of AR 2 and highest for wing of AR 0.5.The lower surface pressure is highest for wing of AR 2. As a result, the pressure difference between the upper and lower surface of wing of AR 2 is also at the highest level. It is observed that the difference between upper and lower surface pressures in segment-C is higher than the pressure difference of segment-B.

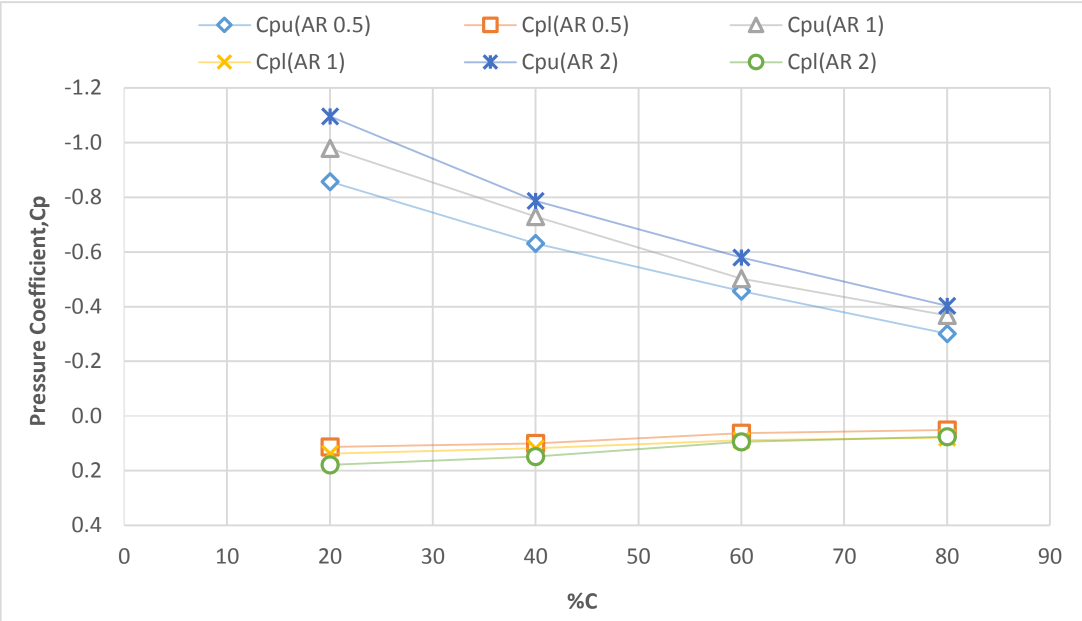

Figure 6.19: Pressure coefficient (C_p) distribution of segment C at 8^0 AOA

From figure 6.20, it is observed that the difference between upper and lower surface pressures in segment-D is highest for wing of AR 2. In segment-D, the pressure difference between two surfaces of respective wing models are lower than those of segment-C. The difference between upper and lower surfaces for all wing models become maximum at 20% C and it is gradually decreasing from leading edge to trailing edge. It is also seen from the graph that the lower surface pressures of all models show no significant differences from 40%C to 80%C.

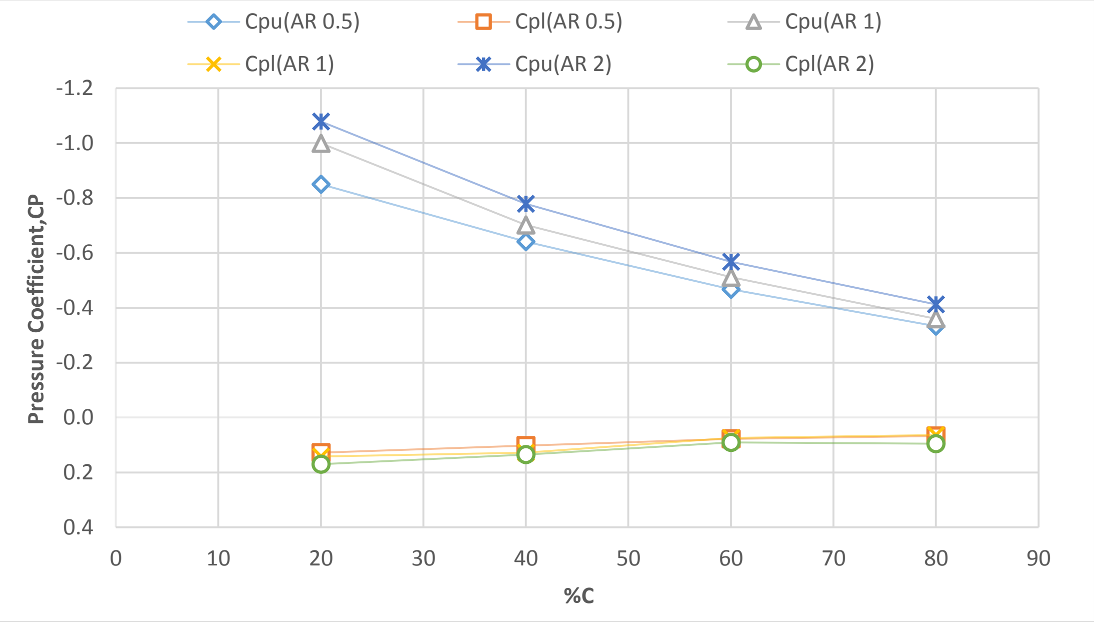

Figure 6.20: Pressure coefficient (C_p) distribution of segment D at 8^0 AOA

6.2.6 Pressure Distributions at 10˚ AOA

Figures 6.21, 6.22, 6.23 and 6.24 represent the surface pressure distribution in terms of pressure coefficient of four segments (A, B, C and D) of wing models with different AR's at 10˚ AOA.

The surface pressure distributions for segment-A of wing models at 10˚ angle of attack are shown in figure 6.21. From the figure, it is observed that upper surfaces of all wing models are having higher negative pressure than the lower surface pressure of the respective wing models. For the wing models of AR 1 and AR 0.5, the lower surface pressure decreases slowly from 20% C to 80% C. The upper surface pressure increases gradually from leading edge to trailing edge. For wing of AR 2 as well, upper surface pressure increases and lower surface pressure decreases from leading edge to the trailing edge. But the upper surface pressure is lowest for wing of AR 0.5 and lower surface pressure is highest for wing of AR 1. As a consequence, the difference between upper and lower surface pressure is observed maximum for wing of AR 2 and the highest difference is achieved at 20%C.

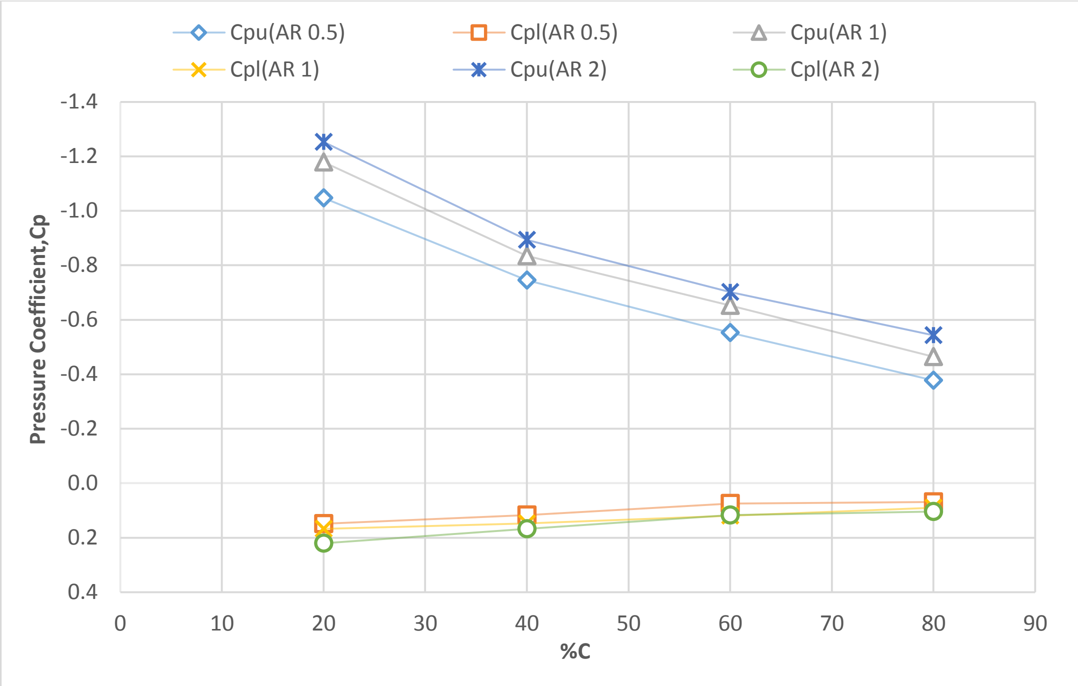

Figure 6.21: Pressure coefficient (C_p) distribution of segment A at 10^0 AOA

From figure 6.22, it is seen that the upper surface pressures of wing models increase from leading edge to trailing edge and the lower surface positive pressures reduce from leading edge to trailing edge in segment-B. The pressure difference between upper and lower surface is thus maximum near the leading edge at 20% C and it is decreasing gradually from 20%C to 80%C.The lower surface pressure is highest for wing of AR 2. Also, the overall pressure difference between upper and lower surface is maximum for wing of AR 2 in segment-B.

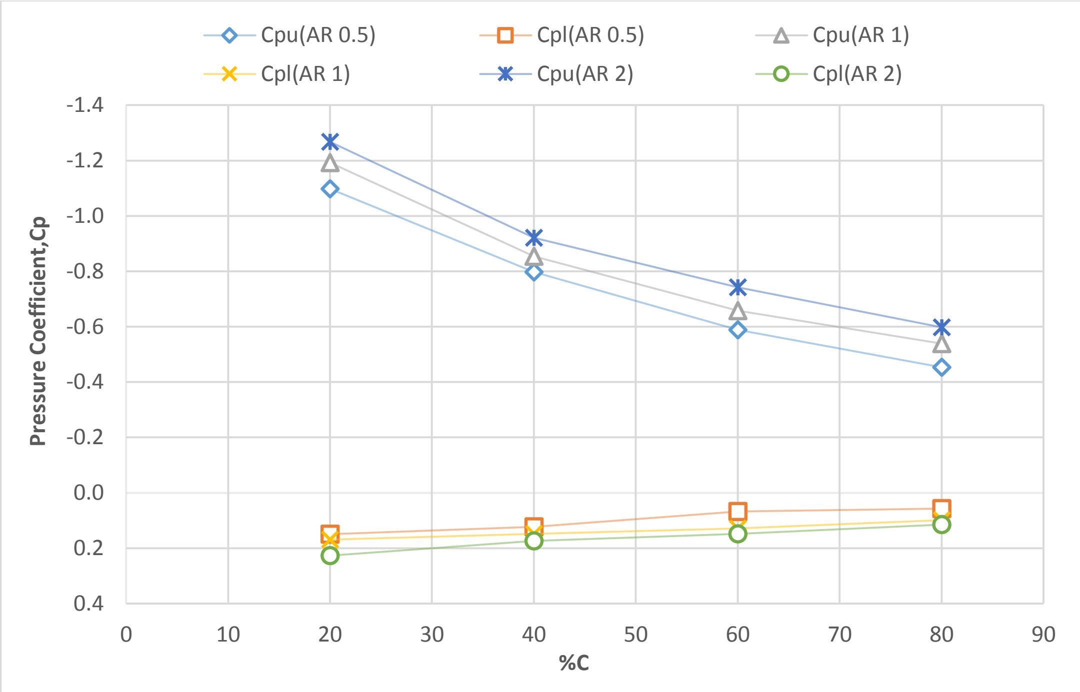

Figure 6.22: Pressure coefficient (C_p) distribution of segment B at 10^0 AOA

Figures 6.23 shows the pressure distribution of segment C of wing models. In segment-C, the difference between upper and lower surface pressure becomes maximum again for wing of AR 2 as shown in Figure 6.19. In this segment as well, the upper surface negative pressure of wing models of AR 0.5 is greater than that of other wing models and lower surface pressure is lower than the other wing models. For segment C, the differences between the upper and lower surface pressures are higher than segment B's pressure differences and is maximum at 20%C. The lower surface pressure is also highest for wing models of AR 2.

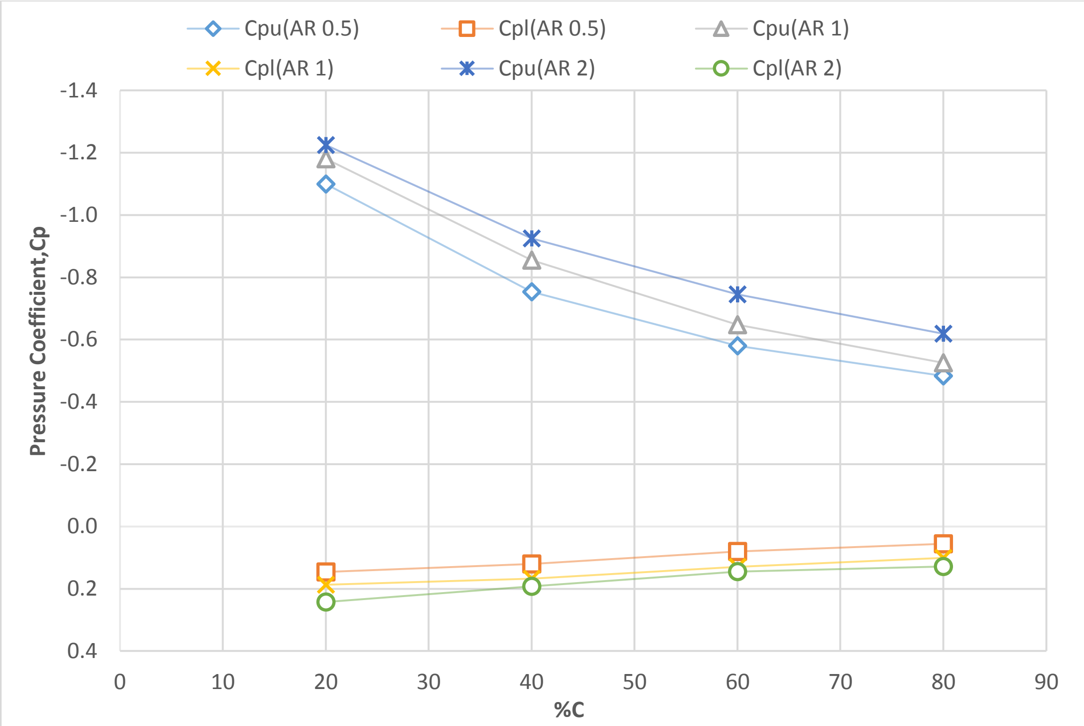

Figure 6.23: Pressure coefficient (C_p) distribution of segment C at 10^0 AOA

In segment-D, overall pressure differences between upper and lower surfaces of wing models seem to be smaller than other segments as shown in figure 6.24. For wing of AR 2, the difference between upper and lower surface pressure is greatest among all wing models in segment D. From Figure 6.20, it is also seen that the upper surface pressure of wing models increases sharply up to 60% C but the lower surface pressure decreases slowly from leading edge to trailing edge. From 60% C to 80% C, the difference between upper and lower surfaces pressure of individual wing model changes very slowly.

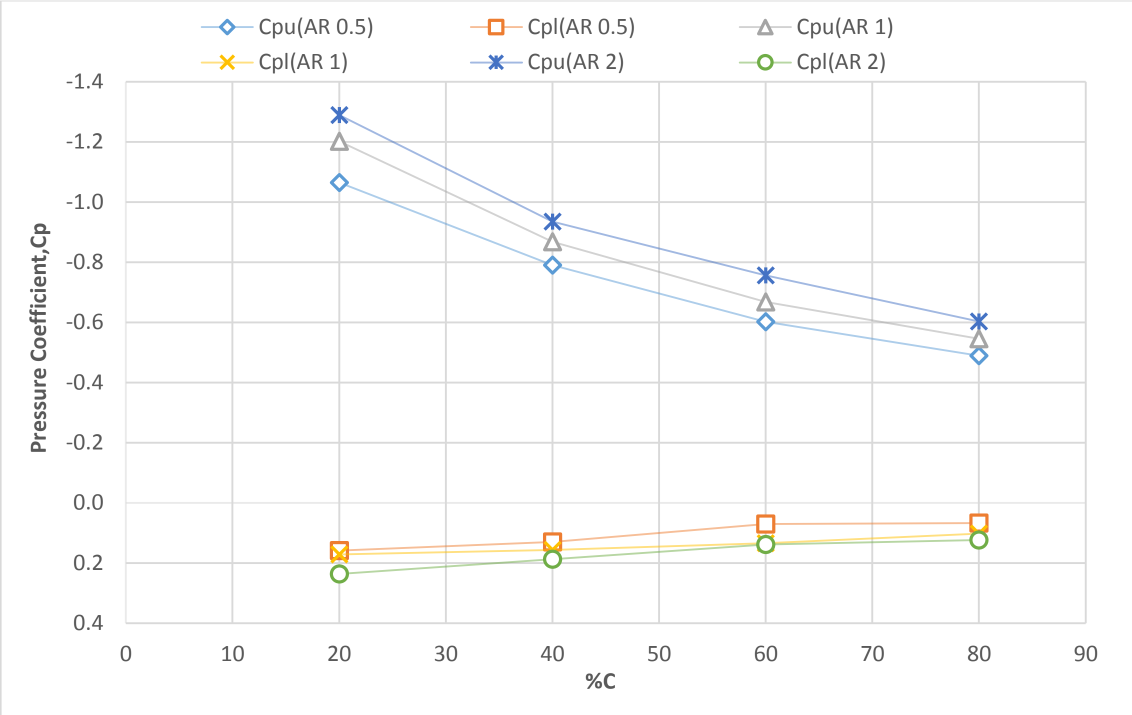

Figure 6.24: Pressure coefficient (C_p) distribution of segment D at 10^0 AOA

6.2.7 Pressure Distributions at 12° AOA

Figures 6.25, 6.26, 6.27 and 6.28 represent the surface pressure distribution in terms of pressure coefficient of four segments (A, B, C and D) of three wing models at 12° AOA.

Pressure distribution along the chord for segment A is shown in figure 6.25. From the graph, it is observed that upper surface pressure of wing models increases from 20% C to 60% C sharply, then increases slowly up to 80% C. The lower surface positive pressure gradually decreases up to from 20% C to 80% C. The largest upper and lower surface pressure difference occurs at 20% of C for all wing models which reduces gradually towards the trailing edge. Wing of AR 2 has the highest surface pressure difference between upper and lower surfaces while wing of AR 0.5 has the lowest pressure difference between upper and lower surfaces. From the graph it is seen that, for AOA 12° the pressure differences between upper and lower surfaces is higher than for AOA 10°.

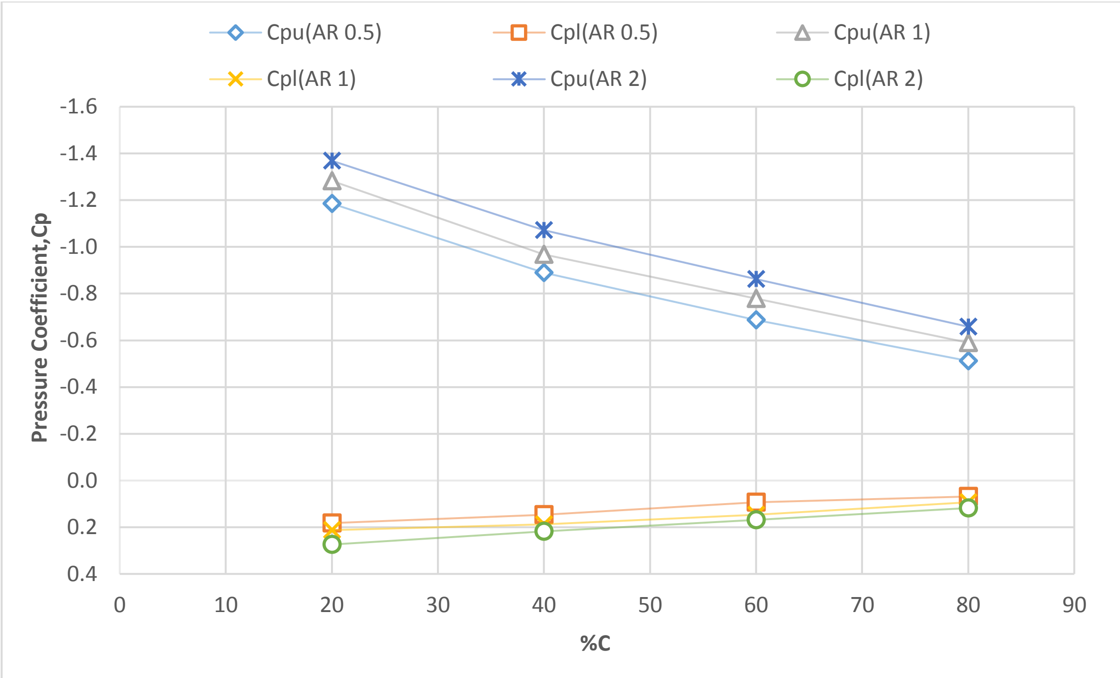

Figure 6.25: Pressure coefficient (C_p) distribution of segment A at 12^0 AOA

Figures 6.26 shows the surface pressure distribution of segment B for wing models at 12˚ angle of attack. In segment B, upper surface pressure increases gradually from leading edge to trailing edge and lower surface pressure decreases gradually from leading edge to trailing edge. The difference between the upper and lower surface pressures of segment B is higher than the difference between the pressures of segment A. The highest-pressure difference is observed near the leading edge at 20 %C and smallest pressure difference is obtained at 80%C.

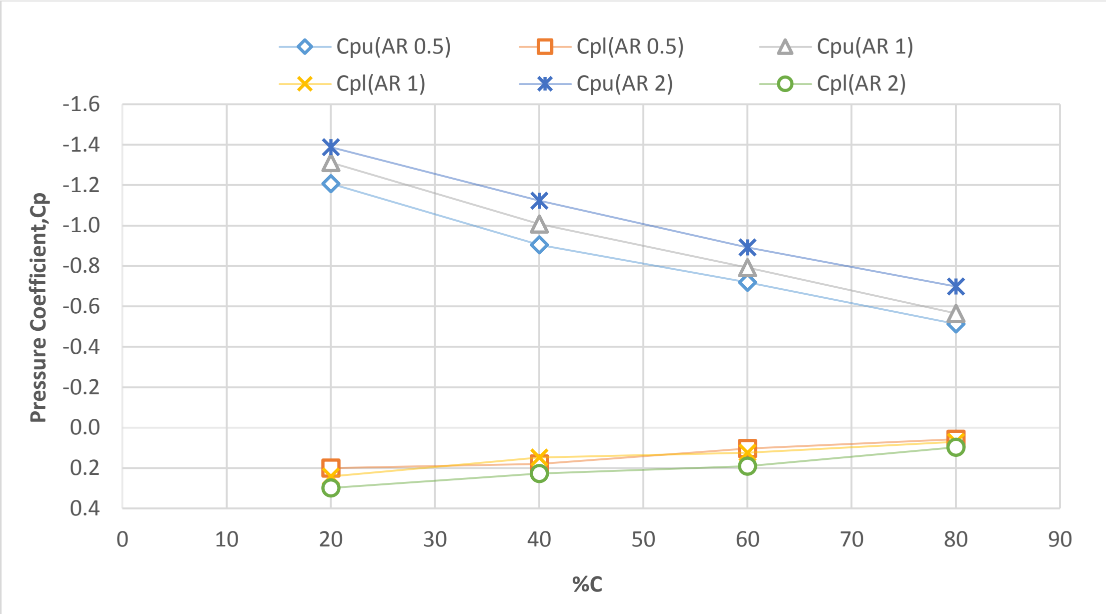

Figure 6.26: Pressure coefficient (C_p) distribution of segment B at 12^0 AOA

In segment C, upper surface pressure increases gradually from 20% C to 80% C for all the wing models. For wing of AR 1 and AR 0.5 the differences between lower surfaces pressure is very small. The lower surface pressure is highest for wing of AR 2.From the graph it is seen that the difference between the upper and lower surface pressures of segment C is lower than the difference between the pressures of segment B. For all the wing models the upper surfaces pressure increases gradually form 20 %C to 80 %C and lower surface pressure decreases gradually from 20 %C to 80%C.

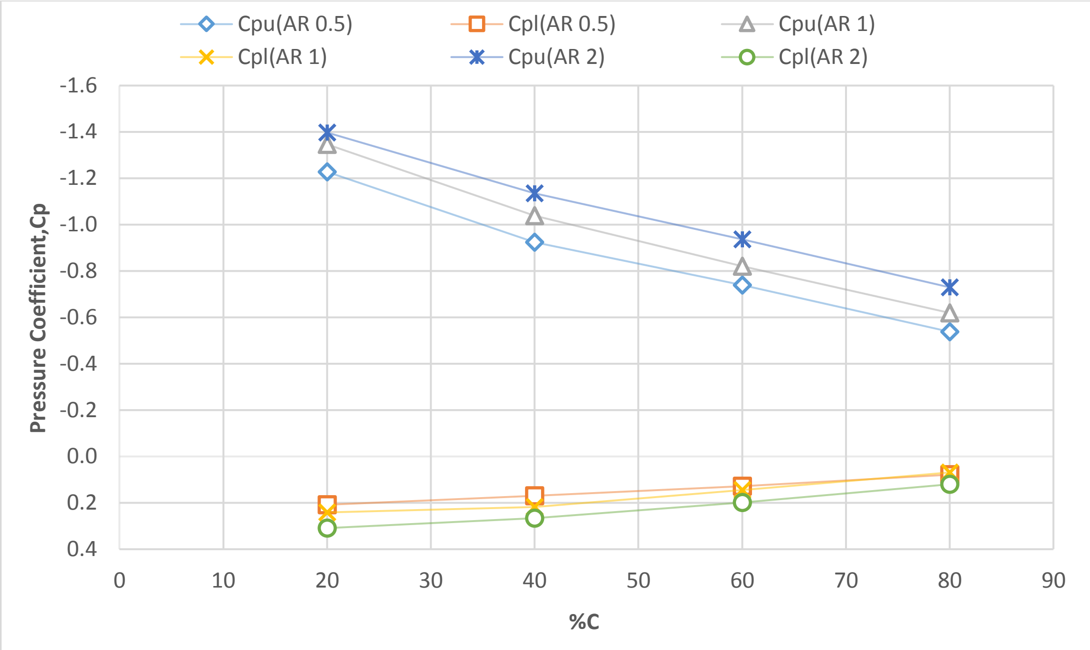

Figure 6.27: Pressure coefficient (C_p) distribution of segment C at 12^0 AOA

In segment D, upper surface pressure increases gradually and lower surface pressure decreases slowly from leading edge to trailing edge. From the figures, it is also observed that overall pressure difference between the upper and lower surface of wing of AR 2 is higher than that of other wing models. The highest pressure difference is achieved at 20 %C and lowest at 80%C.

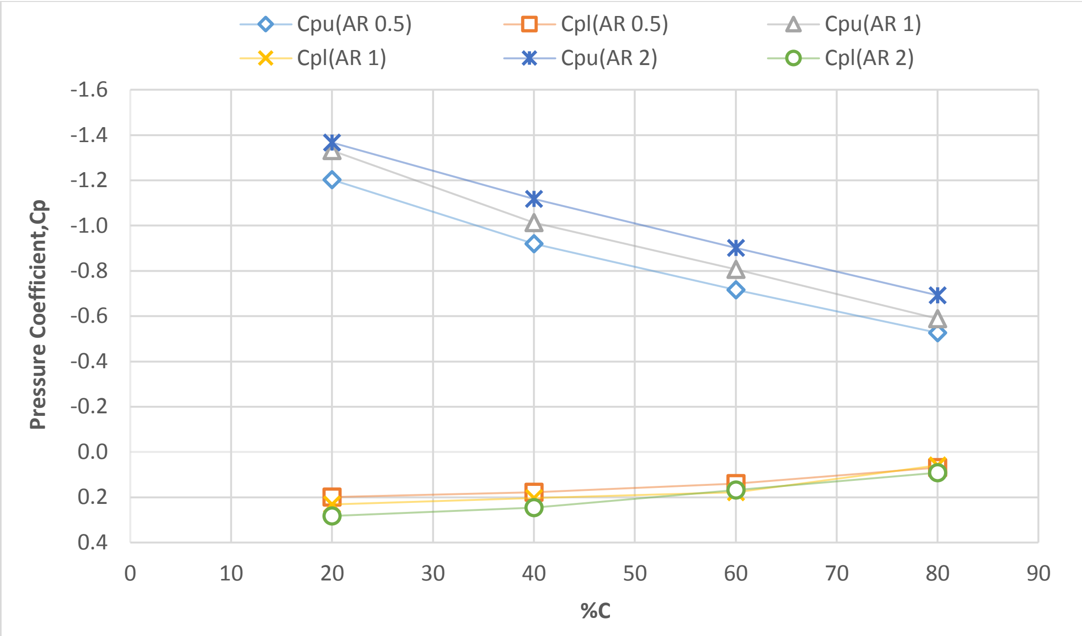

Figure 6.28: Pressure coefficient (C_p) distribution of segment D at 12^0 AOA

6.2.8 Pressure Distributions at 14˚ AOA

The surface pressure distributions along the chord length at 14˚ angle of attack for four segments of wing models are shown in figures 6.29, 6.30, 6.31 and 6.32.

From all the four figures, it is observed that in all segments the upper surface pressures of the wing models are much higher than the upper surface pressure at previous angle of attack (12˚ AOA) as shown in the previous figures. Upper surface pressures of the models tend to increase at a much slower rate compared to the upper surface pressure rise at smaller angle of attack. The surface pressure difference between upper and lower surface of wing models is highest at 20% of C which decreases slowly up to the trailing edge in four segments. In figure 6.29 and figure 6.30 it is observed that, the overall differences between upper and lower surface pressure of wing of AR 2 is observed maximum at segment A and segment B respectively. This phenomenon is also same for segment C and segment D as shown in figure 6.31 and figure 6.32.

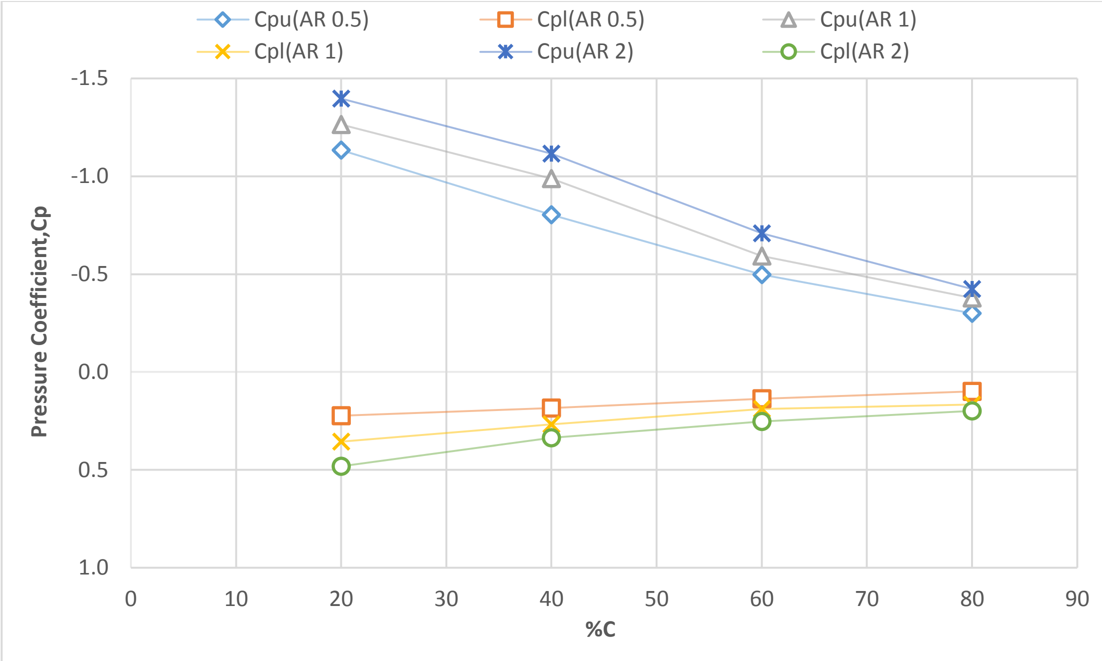

Figure 6.29: Pressure coefficient (C_p) distribution of segment A at 14^0 AOA

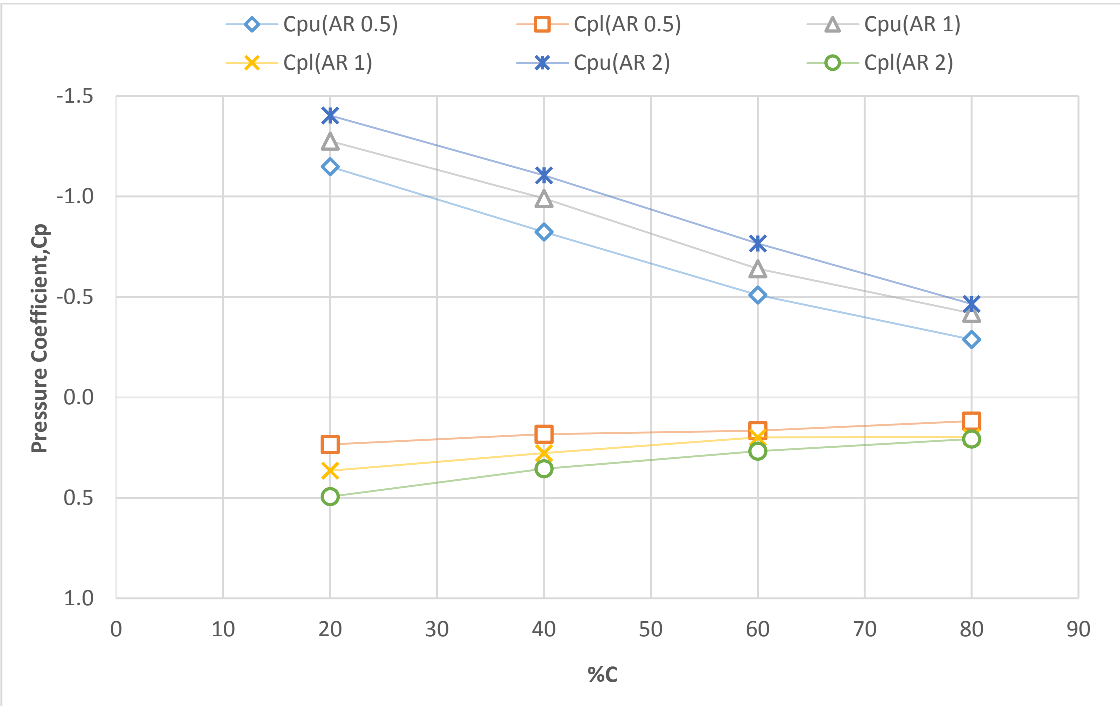

Figure 6.30: Pressure coefficient (C_p) distribution of segment B at 14^0 AOA

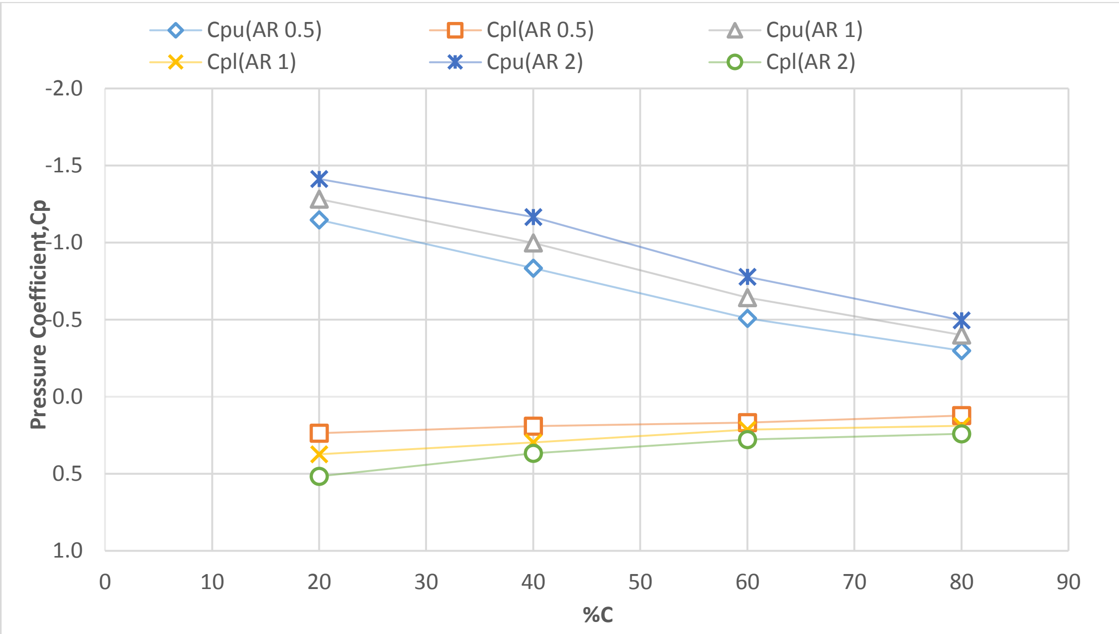

Figure 6.31: Pressure coefficient (C_p) distribution of segment C at 14^0 AOA

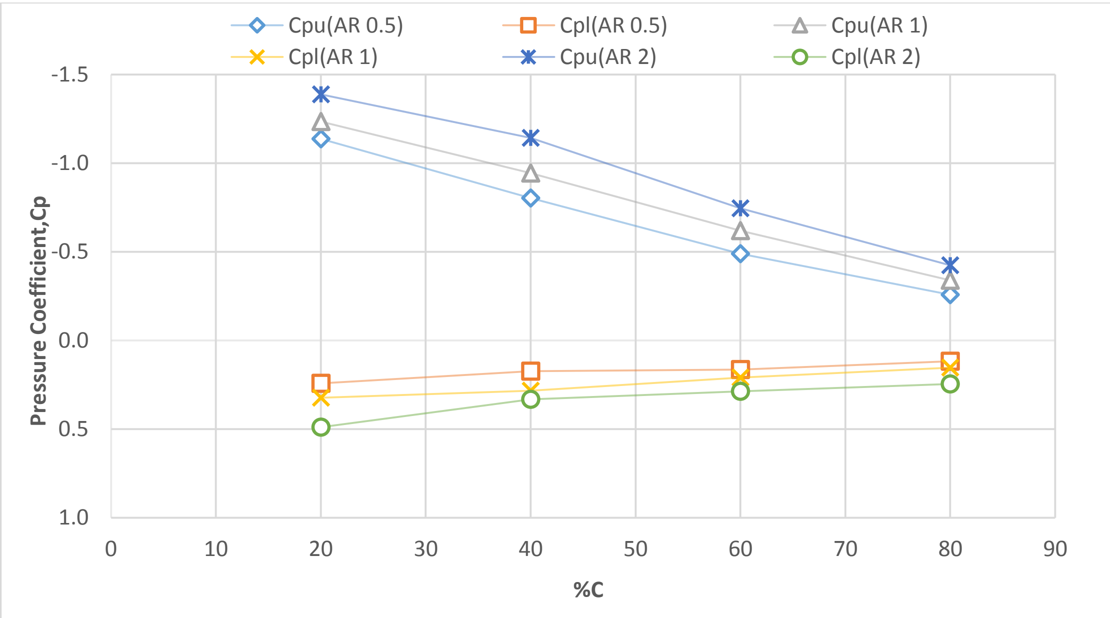

Figure 6.32: Pressure coefficient (C_p) distribution of segment D at 14^0 AOA

From figures 6.29, 6.30, 6.31 and 6.32, it is also observed that pressure difference between upper and lower surfaces of wing models are higher in segment B and segment C compared to the pressure difference of the surfaces in segment A and segment D. Another observation from the figures is that the upper and lower surface pressures of wing models follow almost similar pattern in four segments.

6.2.9 Pressure distribution at 16˚ AOA

Figures 6.33, 6.34, 6.35 and 6.36 represent the surface pressure distribution in terms of pressure coefficient of four segments (A, B, C and D) of wing models at 16˚ AOA. In the figures, both upper and lower surface pressure coefficient, C_{pu} and C_{pl} are plotted along the chord length (C).

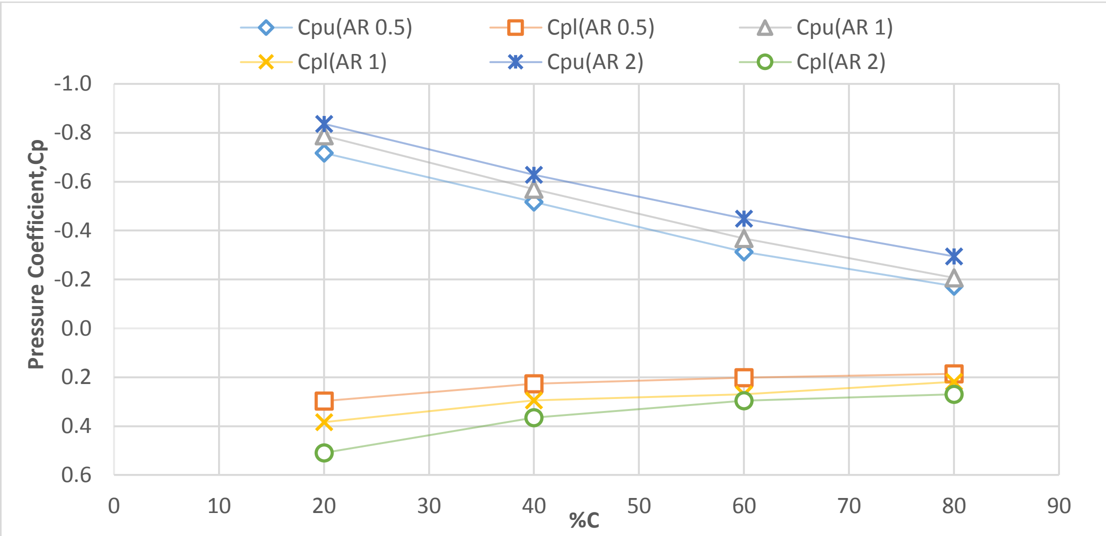

Figure 6.33: Pressure coefficient (C_p) distribution of segment A at 16^0 AOA

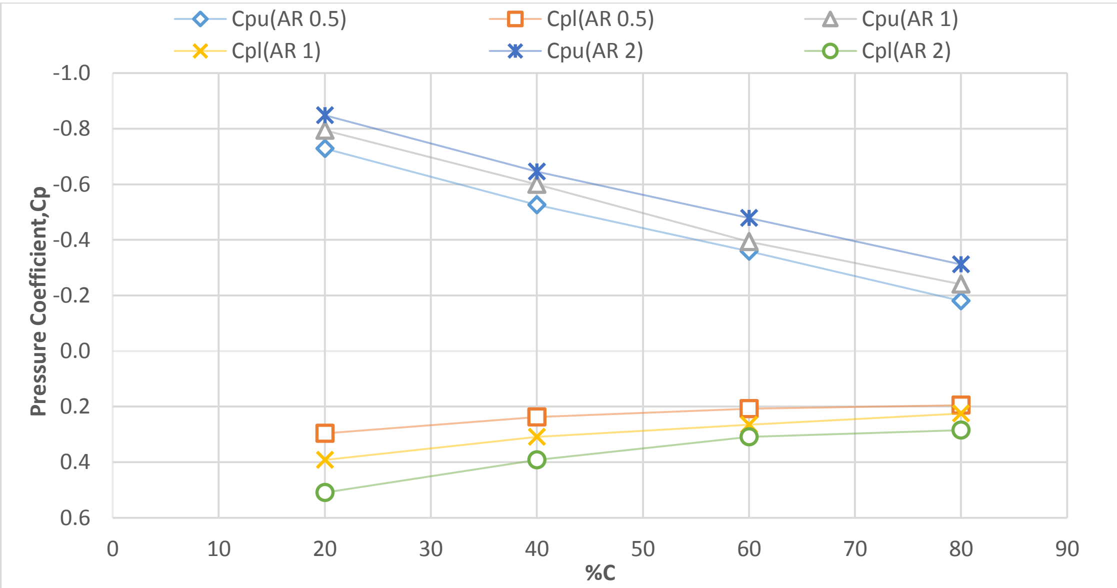

Figure 6.34: Pressure coefficient (C_p) distribution of segment B at 16^0 AOA

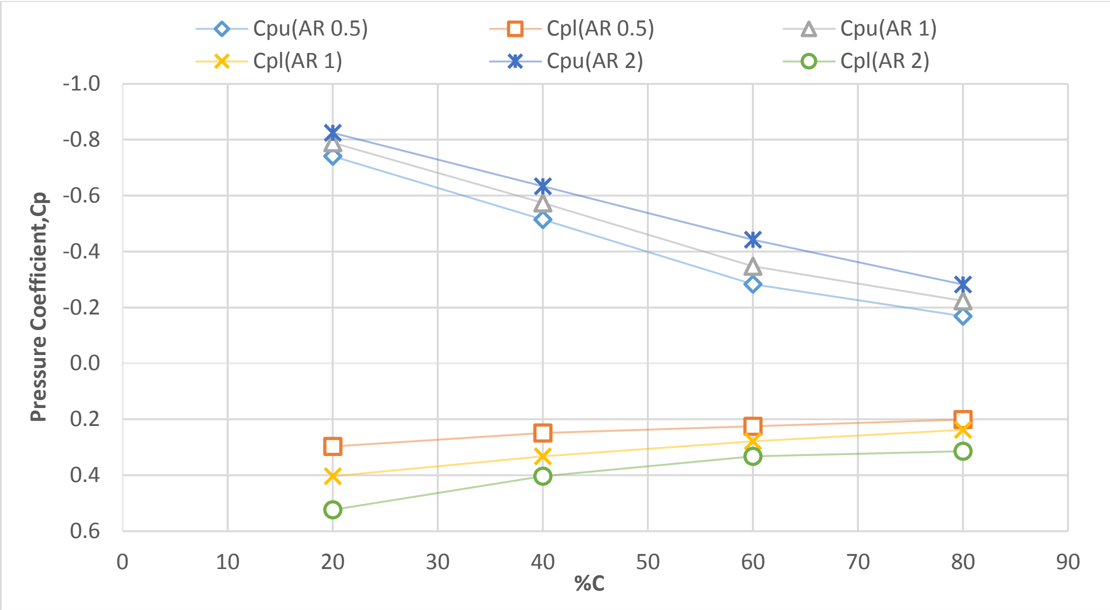

Figure 6.35: Pressure coefficient (C_p) distribution of segment C at 16^0 AOA

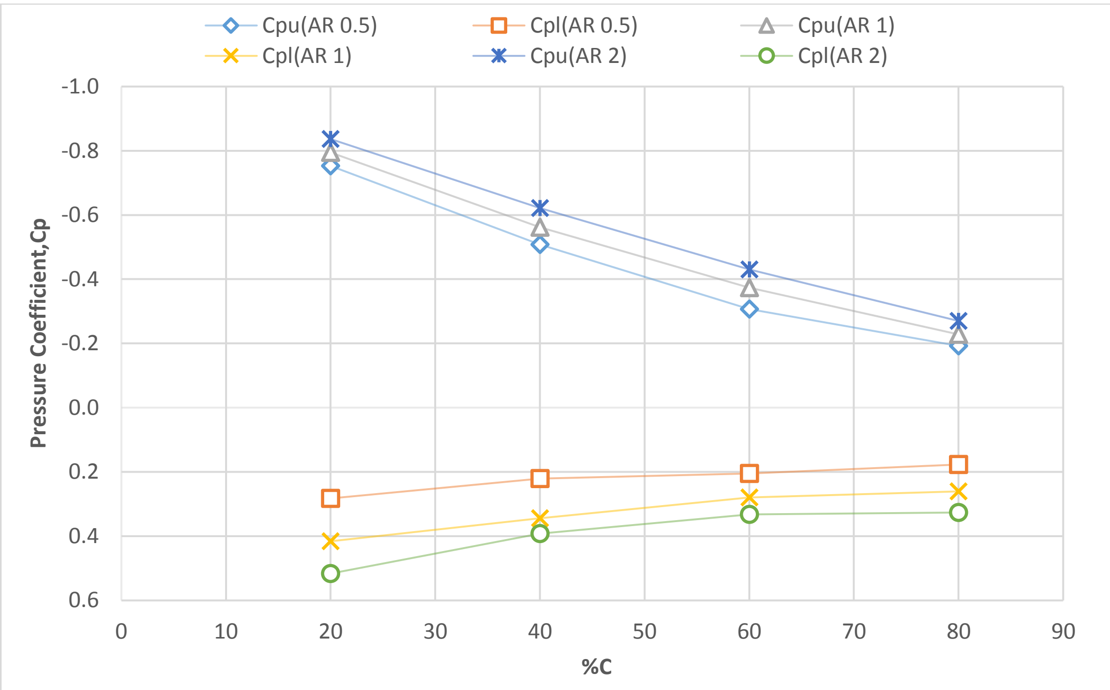

Figure 6.36: Pressure coefficient (C_p) distribution of segment D at 16^0 AOA

In all the four segments at 16° angle of attack, it is observed that the pressure difference between upper and lower surface of all wing models are lower compared to those at previous angle of attack. Among four wing models, wing models of AR 2 is having higher pressure difference between upper and lower surfaces in all segments.

For all four figures the lower surface pressure difference decreases gradually from 20 %C to 80%C and upper surface pressure increases gradually from leading edge to trailing edge. The said difference is highest in both segment B and segment C as shown in Figures 6.34 and 6.35.It is also seen that the lower surface pressure for all the segments is lowest for wing models of AR 0.5 and highest for wing models of AR 2.

6.2.10 Pressure Distributions at 18˚ AOA

The surface pressure distributions along the chord length at 18˚ angle of attack for four segments of wing models are shown in Figures 6.37, 6.38, 6.39 and 6.40.

From all the four figures, it is observed that in all segments the upper surface pressures of the wing models are much higher than the upper surface pressure at previous angle of attack (16˚ AOA) as shown in the previous figures. The surface pressure difference between upper and lower surface of wing models is highest at 20% of C which decreases slowly up to the trailing edge in four segments. In figure 6.37 and figure 6.38 it is observed that, the overall differences between upper and lower surface pressure of wing of AR 2 is observed maximum at segment A and segment B respectively. This phenomenon is also same for segment C and segment D as shown in figure 6.39 and figure 6.40.

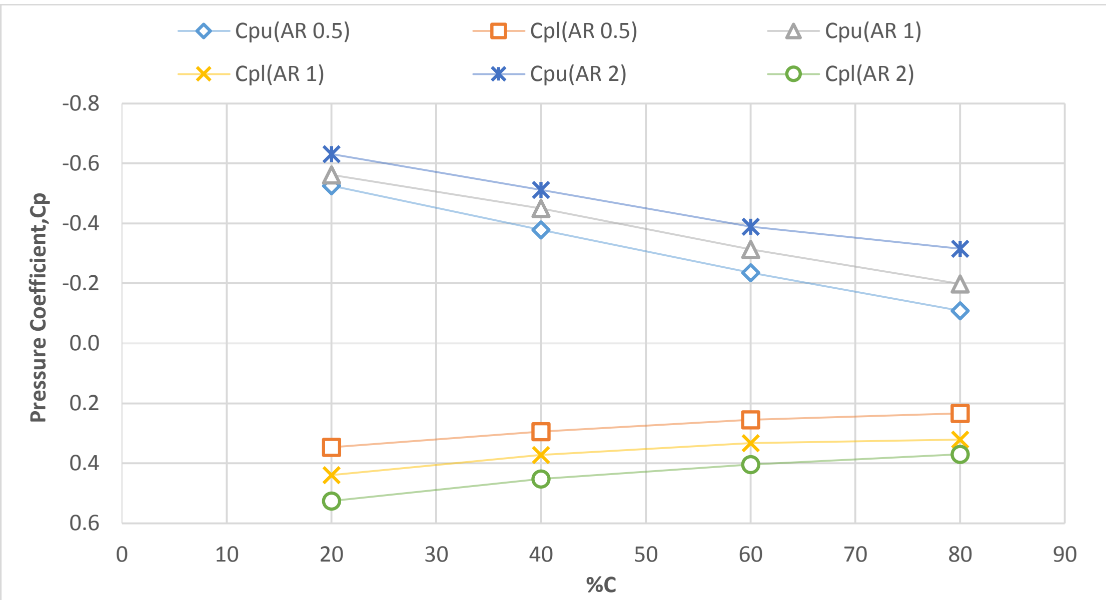

Figure 6.37: Pressure coefficient (C_p) distribution of segment A at 18^0 AOA

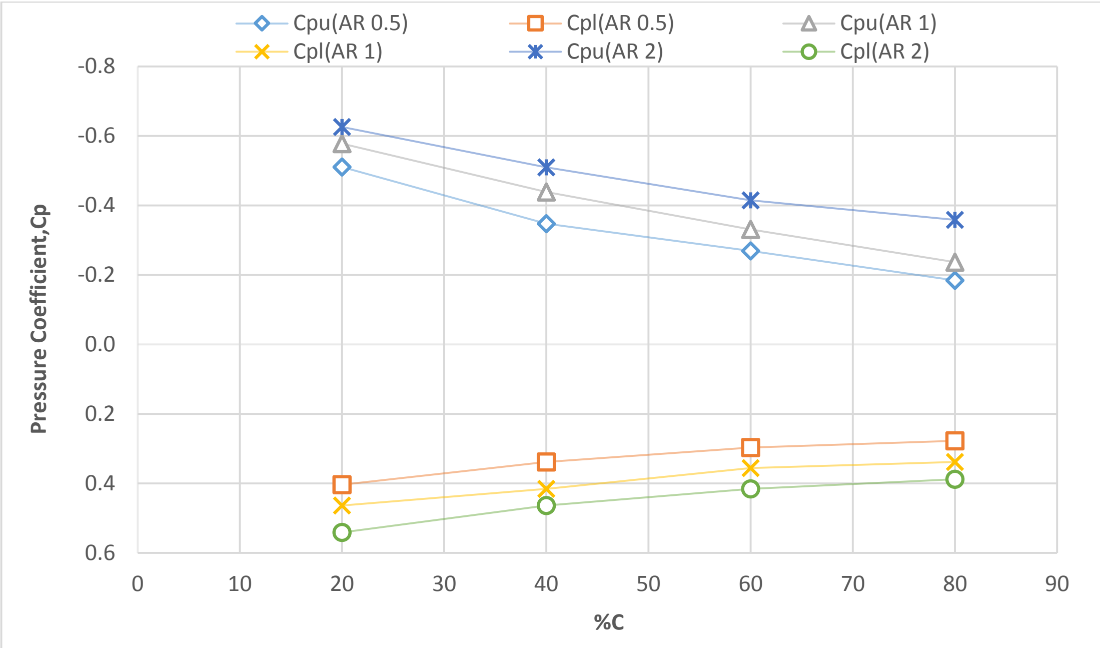

Figure 6.38: Pressure coefficient (C_p) distribution of segment B at 18^0 AOA

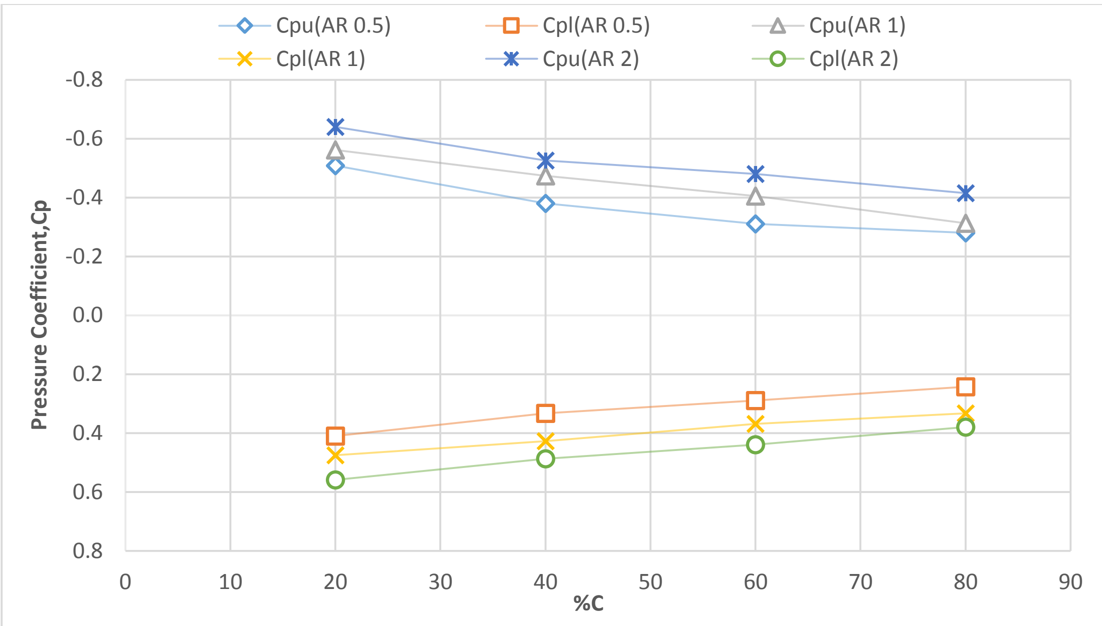

Figure 6.39: Pressure coefficient (C_p) distribution of segment C at 18^0 AOA

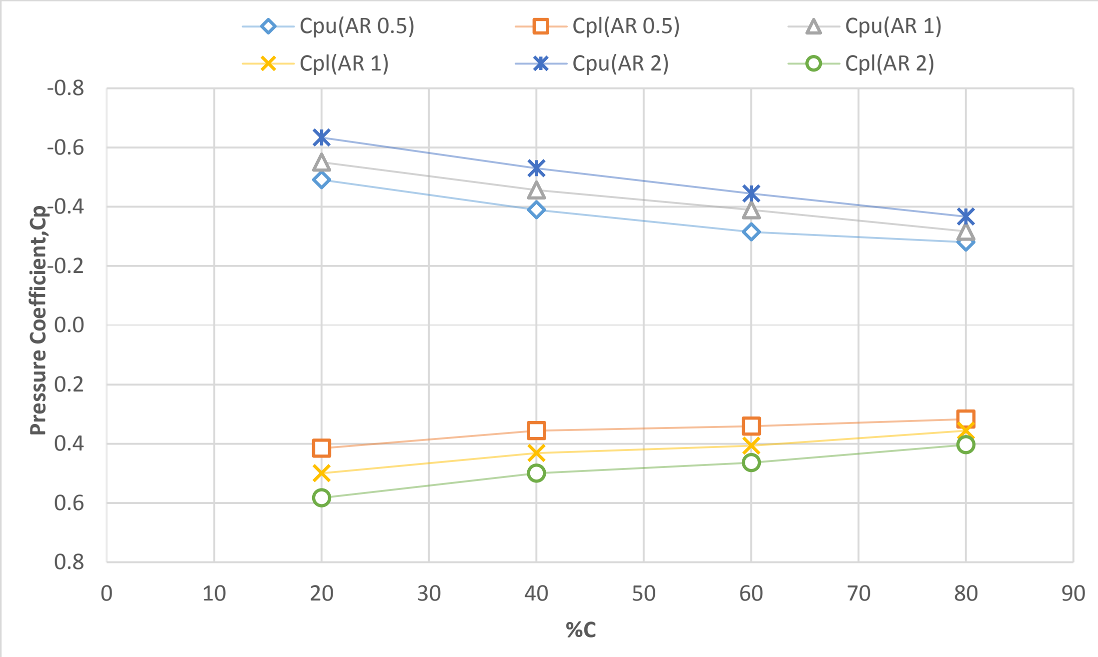

Figure 6.40: Pressure coefficient (C_p) distribution of segment D at 18^0 AOA

From Figures 6.33, 6.34, 6.35 and 6.36, it is also observed that pressure difference between upper and lower surfaces of wing models are higher in segment B and segment C compared to the pressure difference of the surfaces in segment A and segment D. Another observation from the figures is that the upper and lower surface pressures of all wing models follow almost similar pattern in four segments and also the upper surface pressure changes very slowly from 60%C to 80%C for wing models of AR 0.5.It is also seen from the four figures that the lower surface pressure is highest for wing models of AR 2 in all segments from 20%C to 40 %C.

6.2.11 Pressure distribution at 20˚ AOA

Figures 6.41, 6.42, 6.43 and 6.44 represent the surface pressure distribution in terms of pressure coefficient of four segments (A, B, C and D) of wing models at 20˚ AOA. In the figures, both upper and lower surface pressure coefficient, C_{pu} and C_{pl} are plotted along the chord length (C).For all segments at 20˚ AOA both the upper surface pressure and lower surface pressure is larger than the previous angle of attack(18˚).

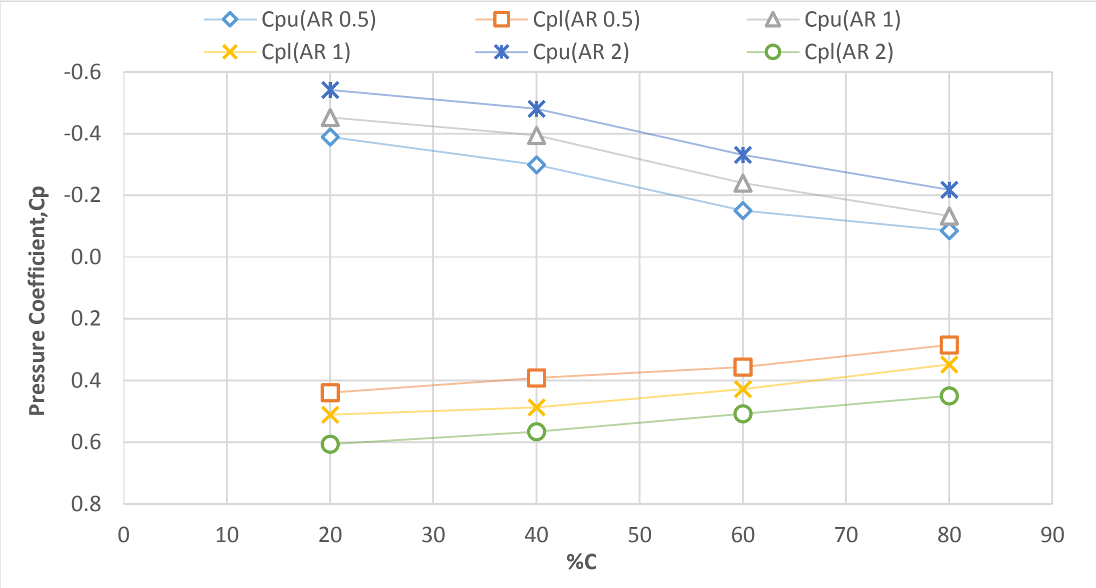

Figure 6.41: Pressure coefficient (C_p) distribution of segment A at 20^0 AOA

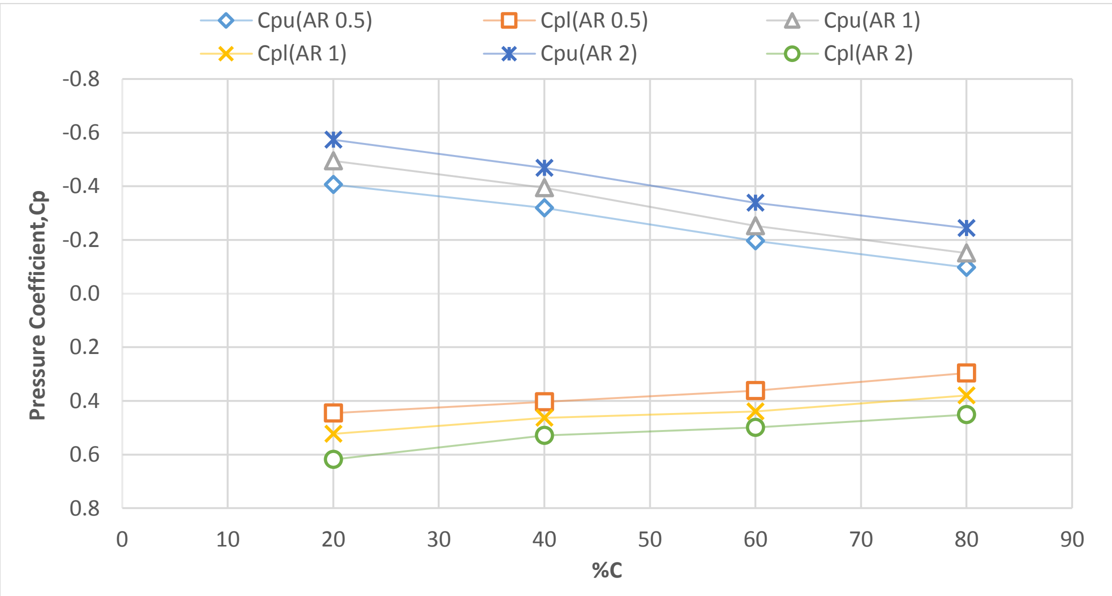

Figure 6.42: Pressure coefficient (C_p) distribution of segment B at 20^0 AOA

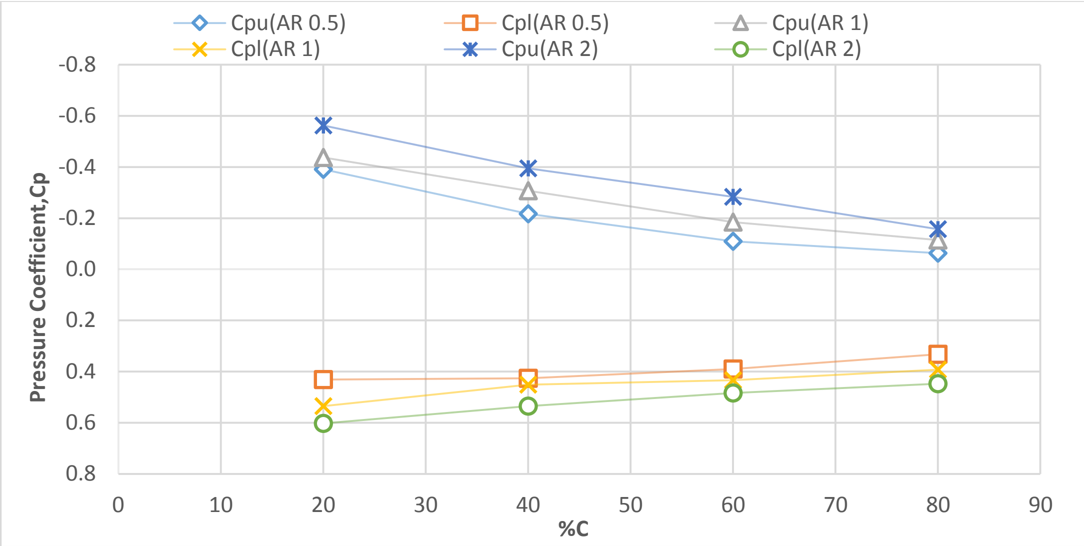

Figure 6.43: Pressure coefficient (C_p) distribution of segment C at 20^0 AOA

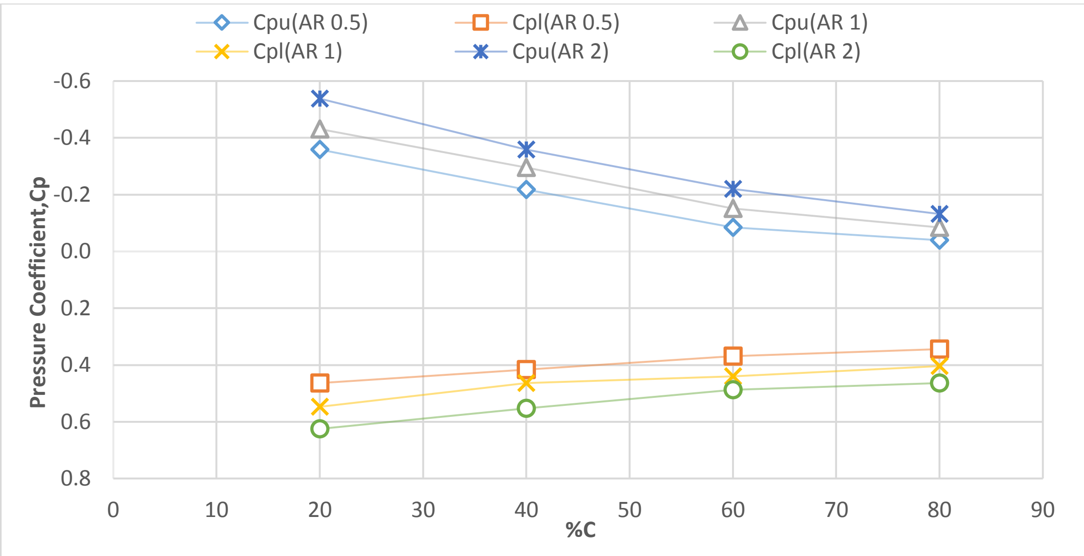

Figure 6.44: Pressure coefficient (C_p) distribution of segment D at 20^0 AOA

In comparison to the pressure difference of the surfaces of model of AR 2 is higher than model of AR 1 and model of AR 0.5. Another observation from the figures is that the lower surface pressure of all the wing models for all the segments are higher than all the previous angle of attack. From figures 6.41, 6.42, 6.43 and 6.44 it is seen that the highest pressure difference between the upper and lower surfaces is obtained for wing models of AR 2 and it is lowest for wing models of AR 0.5. For all the segments the lower surface pressure decreases from 20%C to 80%C and upper surface pressure increases from leading edge to trailing edge.

6.3 Lift Characteristics

The lift characteristics of wing models at different angles are shown in figure 6.45. The lift increases with increase in angle of attack to a maximum value. After this maximum value of angle of attack, lift decreases drastically due to flow separation over the aerofoil surface. From the figure, it is seen that the lift coefficient curve goes up from 0˚ angle of attack up to 12˚ angle of attack for all the wing models and then drops suddenly after 12˚ angle of attack. Thus, the critical angle of attack of all wing models is around 12˚ beyond which the stall happens. This condition is called stalling condition and the corresponding angle of attack is called stalling angle. The stalling angle happens to be approximately 12˚ angle of attack. The magnitude of the lift coefficient of the wing model with AR 2 is seen to be the maximum from figure 6.41. It is also observed that the lift coefficient for wing of AR 2 is much higher than other wing models. It can be concluded that the optimum angle of attack for all wing models is at around 12˚ angle of attack and at this range the ratio between the lift coefficient and the angle of attack is at its maximum. So, in order to obtain maximum lift from NACA 0012 wing, the wing needs to be positioned at around 12˚ with respect to the flight path. These statistics show the similar nature to Kopac analysis [20] and National Aerofoil Data NACA 0012 [37].

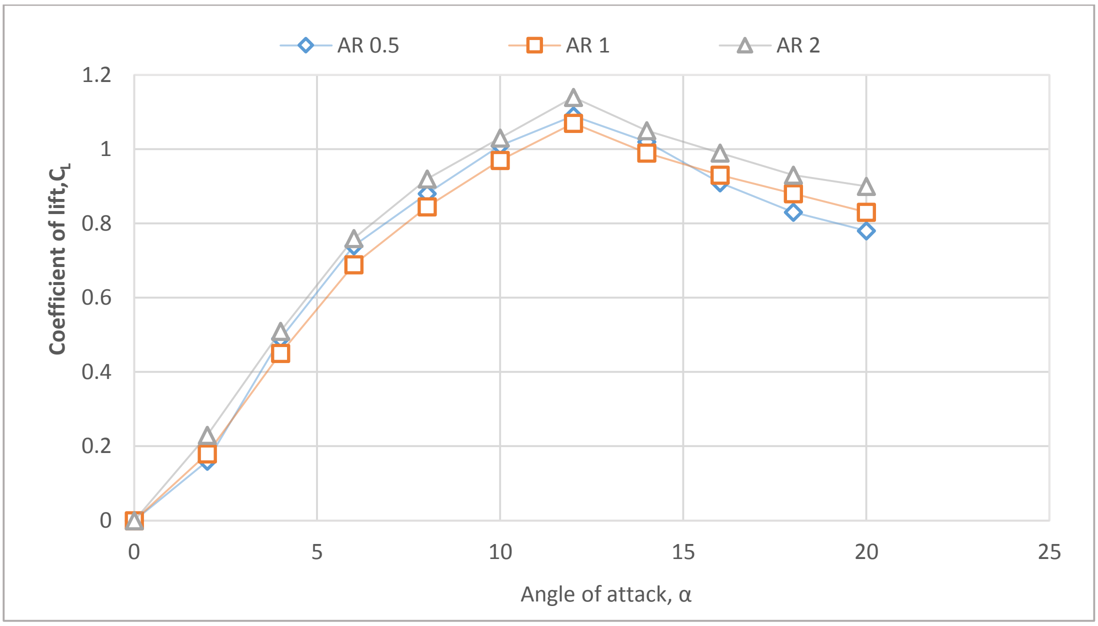

Figure 6.45: Coefficient of lift vs angle of attack

6.4 Drag Characteristics

Figure 6.46 illustrates the drag coefficients of the wing models under test for different angle of attack (AOA). It is seen from the graph that the magnitude of drag coefficient for wings of AR 0.5 are much higher than other wing models and for wing of AR 2 this value is much lower than other wing models. The drag increases with a slower rate initially from 0˚ to 8˚ angle of attack. But from 8˚ to 20˚ angle of attack significant rise in drag is observed. It is observed from the graph that the drag coefficient starts to increase suddenly after stalling angle of attack at 12˚. This sudden increase in drag coefficient occurs because the air detaches from the surface of the airfoil due to strong adverse pressure gradient after stalling angle of attack. This sudden increase of drag coefficient indicates that if the angle of attack is increased any further the drag will dominate the lift and stall will occur. These results are in terms with Kopac analysis [20] and National Aerofoil Data NACA 0012 [37].

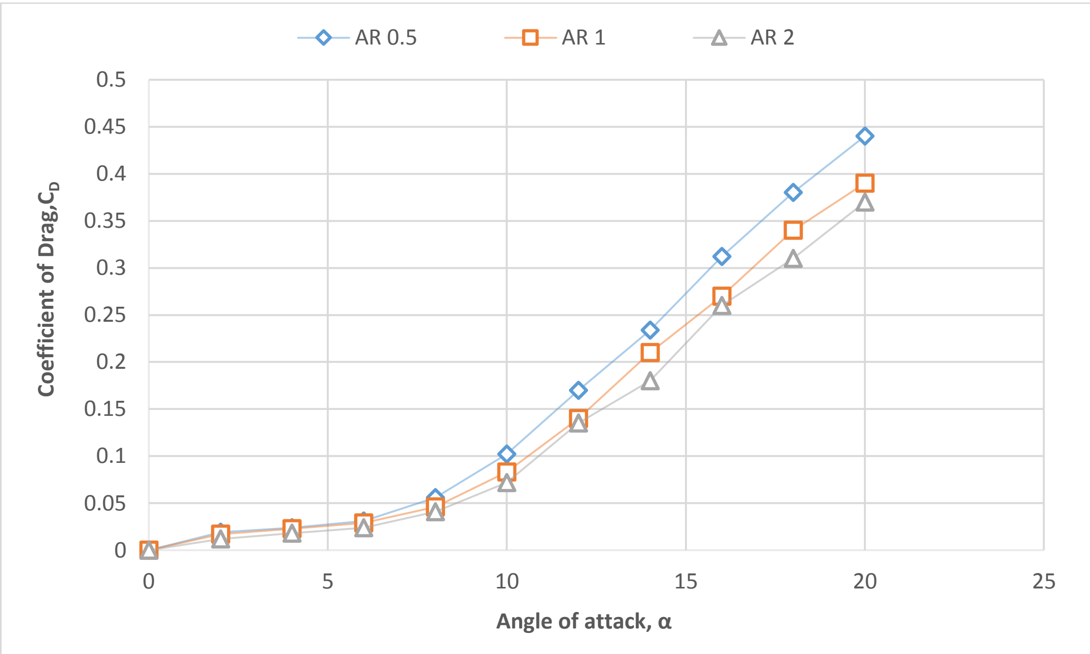

Figure 6.46: Coefficient of drag vs angle of attack

6.5 Lift Coefficient to Drag Coefficient Ratio

The magnitude of lift coefficient to drag coefficient ratio are plotted for various angle of attack in Figure 6.47. An inspection of figure 6.43 indicates that the lift coefficient to drag coefficient ratio for wing model of AR 2 is remarkably higher than other two wing models. It is also observed that the wing of AR 0.5 has the lowest lift to drag coefficient ratio compared to other wing models. It is seen from the graph that the wing of AR 2 has an increasing lift to drag coefficient ratio up to the angle of attack 6^0 attaining the maximum value of 31.67.This phenomenon is also same for other two wing models of AR 1 and AR 0.5. It can be found that the pattern of the lift to drag ratio shows similar trend with National Aerofoil Data NACA 0012 [37] and Kopac analysis [20].A rapid decrease in the lift to drag coefficient ratio occurs in the interval 6^0 to 12^0 AOA. For AOA>12^0 a variation close to horizontal line is observed for all wing models. An analysis of figure 6.43 yields the result that the wing model of AR 2 is the most efficient.

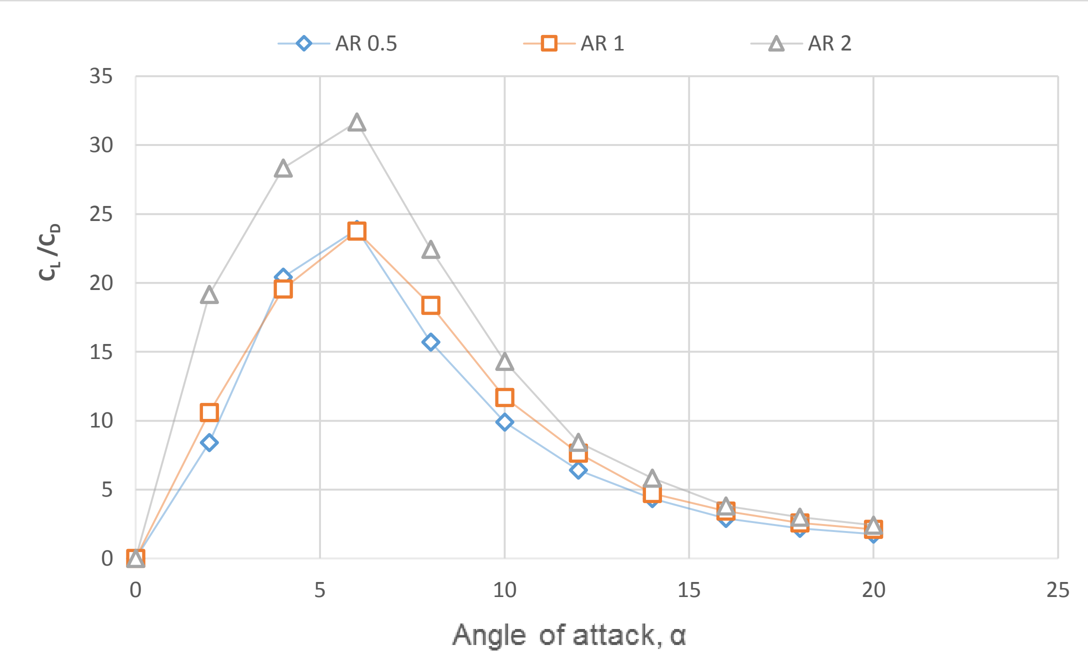

Figure 6.47: Comparison of lift to drag coefficient curve for different aspect ratios

6.6 Effect of Coefficient of Performance ($C_L^{1.5}/C_D$)

The variation of performance coefficients of wing models for different aspect ratios to the angle of attack are plotted in Figure 6.48. The performance coefficients of wing models are seen to be similar to the variation of lift coefficient to drag coefficient ratio. An analysis of figure 6.44 illustrates that performance coefficients of wing models of AR 2 is remarkably higher than other two wing models. It is also observed that the wing of AR 0.5 has the lowest performance coefficients compared to other wing models. It is also observed from the graph that all the wing models have an increasing coefficient of performance up to the angle of attack 6^0 attaining the maximum value, then a rapid decrease occurs in the interval 6^0 to 12^0 AOA. For AOA>12^0 a variation close to horizontal line is observed for all wing models. The wing model of AR 2 is seen to the best according to the coefficient of performance. It can be found that the pattern shows similar trend with Kopac analysis [20].

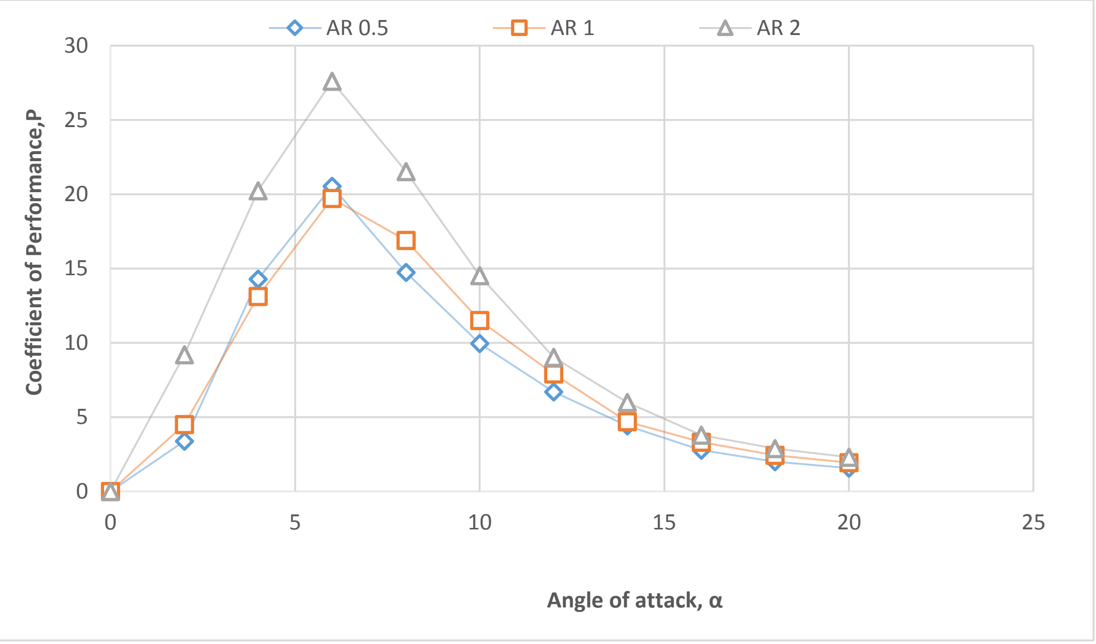

Figure 6.48: Comparison of coefficient to performance curve for different aspect ratios.

The present experimental investigation yielded the conclusion that the wing model of AR 2 attains the maximum lift to drag coefficient and also attains maximum coefficient of performance. So, according to this judgment the wing model of AR 2 is found to be the optimum.

6.7 Surface Pressure Distributions of optimum wing models with backward facing step

The pressure distributions of both upper and lower surfaces along the chord length of four segments (Segment- A, B, C and D) of the optimum wing models of AR 2 at 0^0, 2^0, 4^0, 6^0, 8^0,10^0,12^0, 14^0, 16^0, 18^0 and 20^0 angle of attack (AOA) are shown in Fig. 6.49 to 6.93. In the figures, the horizontal axis represents the percentage of the chord length (%C) and the vertical axis represents the surface pressure coefficient (Cp). The vertical axis above the zero line (horizontal axis) denotes the negative pressure coefficients or suction pressure coefficients and the vertical axis below the zero line denotes the positive pressure coefficients. All the graphs are discussed in details in the subsequent sub-paragraphs.

6.7.1 Pressure Distributions at 0˚ AOA for optimum wing model with BFS

Figures 6.49, 6.50, 6.51 and 6.52 represent the surface pressure distribution in terms of pressure coefficient of four segments (A, B, C and D) for optimum wing model with BFS at 0˚ AOA. In the figures, both upper and lower surface pressure coefficient, Cpu and Cpl are plotted along the chord length (C).

The surface pressure coefficients of segment A at 0˚ are shown in figure 6.49. It is observed from the graph that the pressure on the wing near the root is negative pressure which is very low for optimum wing model with and without BFS. Near the leading edge both the upper and the lower surfaces of the model is experiencing the same negative pressure. But after 25% C towards the trailing edge both the upper and lower surfaces pressure coefficients are increasing. It is also observed that both the lower and upper surfaces pressure increase slowly from 20% to 40% C and then increases sharply up to 80% C. After 60%C the upper surface pressures is increasing more sharply for optimum wing model without BFS than the optimum wing model with BFS. For the optimum wing models without BFS the pressure difference between the upper and lower surfaces are negligible because of symmetricity of the wing.

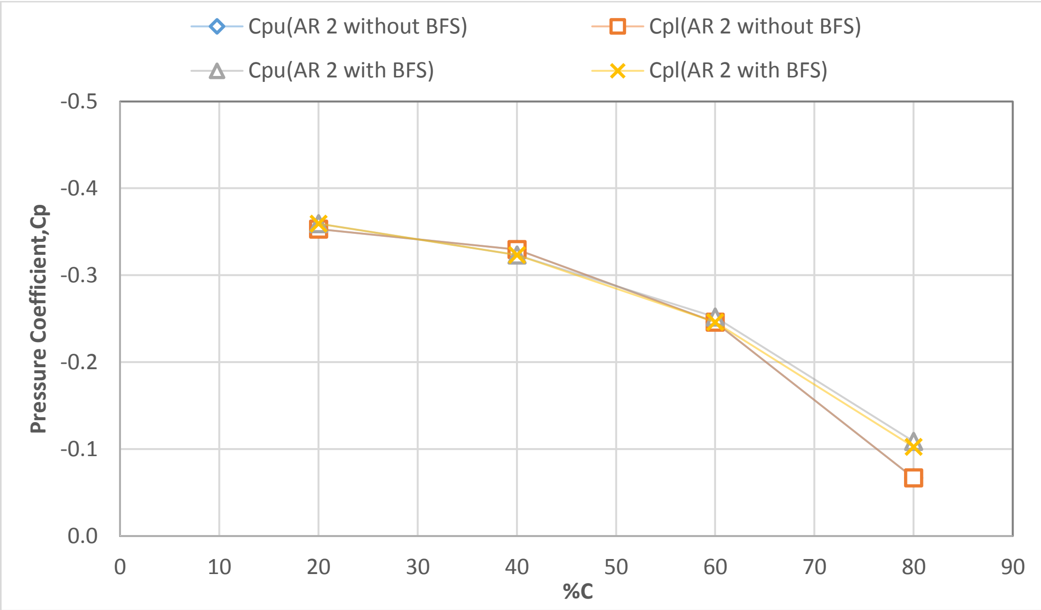

Figure 6.49: C_p distribution of segment A at 0^0 AOA

Figure 6.50 illustrates the surface pressure coefficients of segment B at 0˚ AOA. It is seen from the graph that the pressure on the wing near the root is negative pressure which is very low for the optimum wing model with and without BFS. Near the leading edge both the upper and the lower surfaces of the wing models are experiencing the same negative pressure because of symmetricity. But after 25% C towards the trailing edge both the upper and lower surfaces pressure coefficients are increasing. It is also observed that both the lower and upper surfaces pressure increase slowly from 20% to 40% C and then increases sharply up to 80% C for both wing model with and without BFS. After 60%C from the leading edge it is seen that the upper surface pressure is increasing more sharply for optimum wing model without BFS than the wing model with BFS.

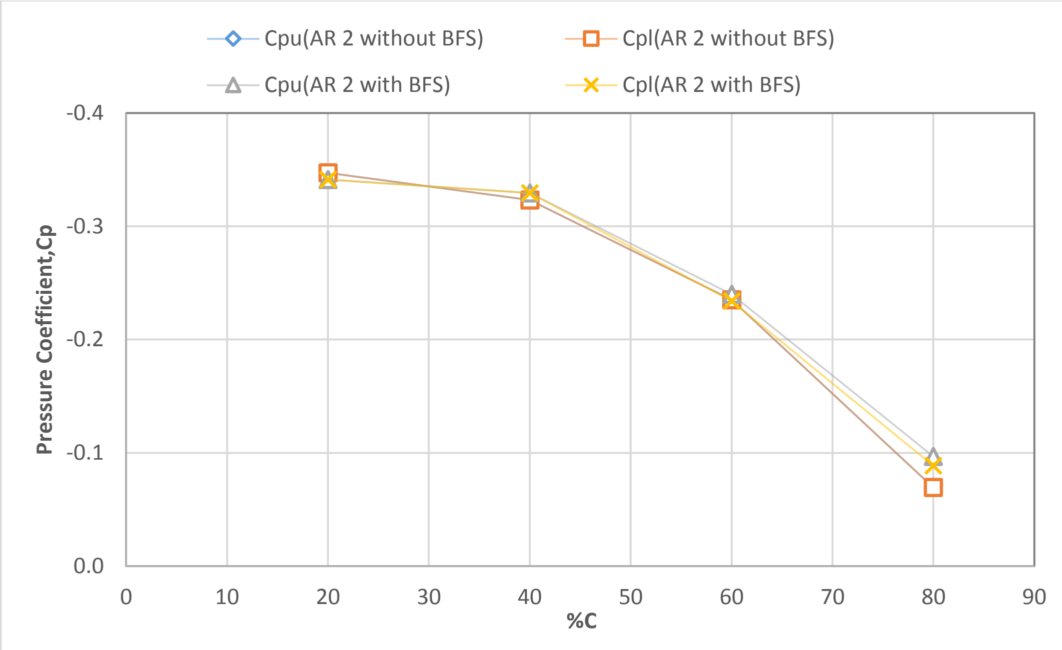

Figure 6.50: C_p distribution of segment B at 0^0 AOA

The surface pressure coefficients of segment C at 0° are shown in Figure 6.51. It is observed from the graph that the pressure on the wing near the root is negative pressure which is very low for optimum wing model with and without BFS. Near the leading edge both the upper and the lower surfaces of the model is experiencing the same negative pressure. But after 25% C towards the trailing edge both the upper and lower surfaces pressure coefficients are increasing. It is also observed that both the lower and upper surfaces pressure increase slowly from 20% to 40% C and then increases sharply up to 80% C. After 60%C the upper surface pressures is increasing more sharply for optimum wing model without BFS than the optimum wing model with BFS. It is also observed from the graph that the values of pressure coefficients of segment C is higher than the values of pressure coefficients of segment B. For the optimum wing models without BFS the pressure difference between the upper and lower surfaces are negligible because of symmetricity of the wing.

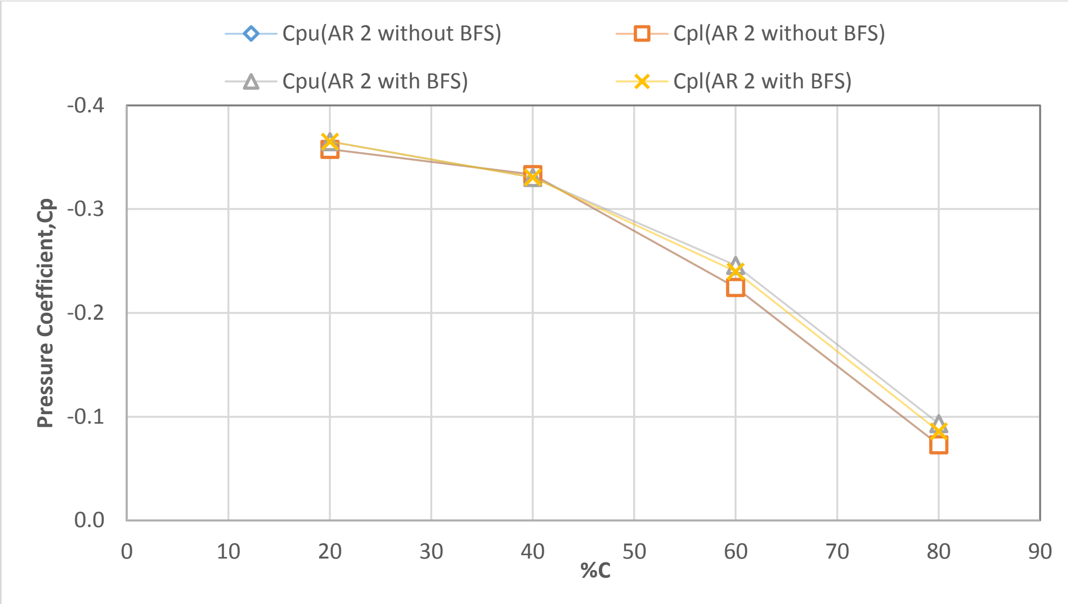

Figure 6.51: C_p distribution of segment C at 0^0 AOA

Figure 6.52 illustrates the surface pressure coefficients of segment D at 0˚ AOA. It is seen from the graph that the pressure on the wing near the root is negative pressure which is very low for the optimum wing model with and without BFS. After 25% C towards the trailing edge both the upper and lower surfaces pressure coefficients are increasing. It is also observed that both the lower and upper surfaces pressure increases slowly from 20% to 40% C and then increases sharply up to 80% C for both wing model with and without BFS. After 60%C from the leading edge it is seen that the upper surface pressure is less for the optimum wing model with BFS than the optimum wing model without BFS. . For the optimum wing models without BFS the pressure difference between the upper and lower surfaces are negligible because of symmetricity of the wing.

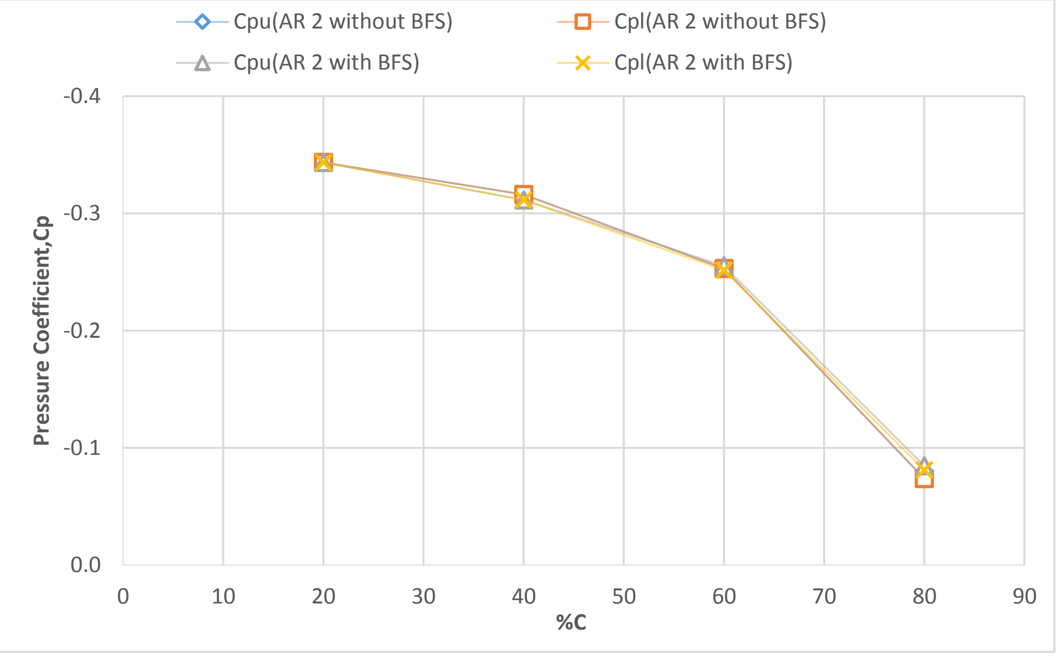

Figure 6.52: C_p distribution of segment D at 0^0 AOA

6.7.2 Pressure Distributions at 2˚ AOA for optimum wing model with BFS

Figures 6.53, 6.54, 6.55 and 6.56 represent the surface pressure distribution in terms of pressure coefficient of four segments (A, B, C and D) of wing for optimum wing model with BFS at 2˚ AOA. In the figures, both upper and lower surface pressure coefficient, Cpu and Cpl are plotted along the chord length (C).

In figure 6.53, the surface pressure distributions for segment-A of the optimum wing model with and without BFS at 2˚ AOA are shown. It is observed that upper surfaces of wing model with and without BFS are having higher negative pressure than the lower surfaces. The upper surface pressures for the optimum wing model with and without BFS increase gradually towards the trailing edge. The upper surface pressure is smaller for the optimum wing with BFS than the optimum wing without BFS. For the optimum wing model with and without BFS, the lower surface pressure decreases slowly up to the trailing edge. The pressure difference between upper and lower surfaces is slightly higher for optimum wing model with BFS than the optimum wing model without BFS. For the optimum wing model with BFS and without BFS, the difference between upper and lower surface becomes maximum at 20% C. It is seen from the graph that a slightly increase in difference between the upper and lower surfaces observed from 60%C to 80%C.

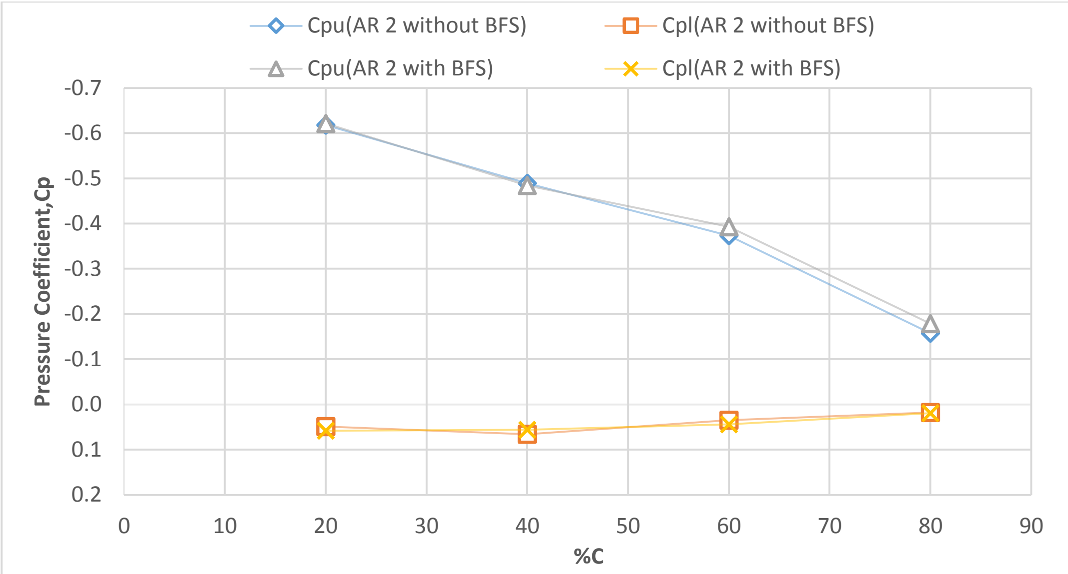

Figure 6.53: C_p distribution of segment A at 2^0AOA

The surface pressure distributions for segment-B of the optimum wing model with and without BFS at 2˚ AOA are shown in figure 6.54. From the graph it is seen that the upper surfaces of wing model with and without BFS are having higher negative pressure than the lower surfaces. The upper surface pressures increase gradually towards the trailing edge for the optimum wing model with and without BFS. The upper surface pressure is lowest for the optimum wing with BFS than the optimum wing without BFS. For the optimum wing model with and without BFS, the lower surface pressure decrease slowly from 20% C to 40% C and then decreases gradually up to the trailing edge. It is observed from the graph that a small increase in difference between the upper and lower surfaces observed from 40%C to 80%C between the optimum wing with BFS and optimum wing without. The pressure difference between upper and lower surfaces is slightly higher for optimum wing model with BFS than the optimum wing model without BFS.

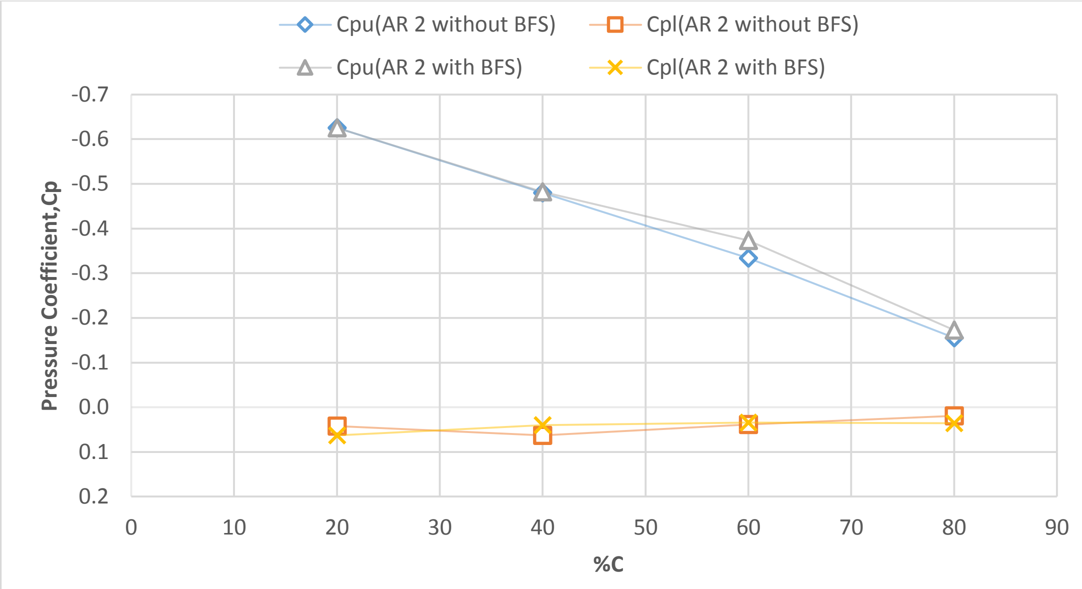

Figure 6.54: C_p distribution of segment B at 2^0AOA

In figure 6.55 the surface pressure distributions for segment-C of the optimum wing model with and without BFS at 2˚ AOA are shown. The upper surface pressures increase gradually towards the trailing edge for the optimum wing model with and without BFS. But the upper surface pressure of optimum wing with BFS is smaller than the optimum wing model without BFS. It is seen from the graph that the upper surfaces of wing model with and without BFS are having higher negative pressure than the lower surfaces. For the optimum wing model with and without BFS, the lower surface pressure decrease slowly from 20% C to 40% C and then decreases gradually up to the trailing edge. It is seen from the graph that from 40%C to 80%C a smaller increase in difference between the upper and lower surfaces observed between the optimum wing with BFS and optimum wing without.

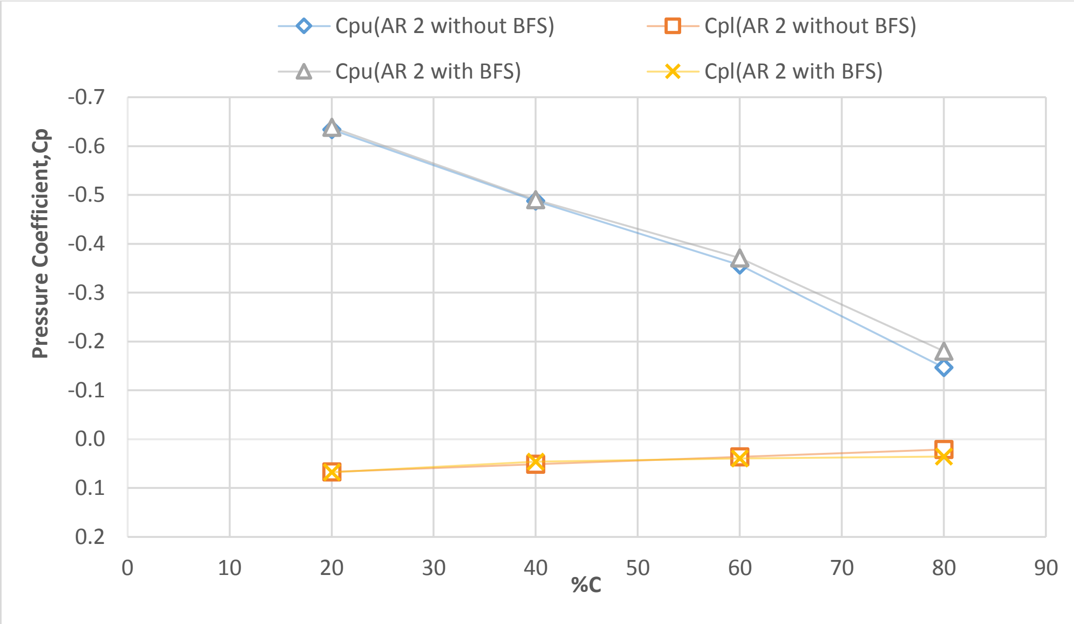

Figure 6.55: C_p distribution of segment C at 2^0 AOA

In Figure 6.56, the surface pressure distributions for segment-D of the optimum wing model with and without BFS at 2˚ AOA are shown. It is observed that upper surfaces of wing model with and without BFS are having higher negative pressure than the lower surfaces. The upper surface pressures for the optimum wing model with and without BFS increase gradually towards the trailing edge from 20%C to 80%C. The upper surface pressure is smaller for the optimum wing with BFS than the optimum wing without BFS. For the optimum wing model with and without BFS, the lower surface pressure decrease slowly from 20% C to 80% C. The pressure difference between upper and lower surfaces is slightly higher for optimum wing model with BFS than the optimum wing model without BFS. For the optimum wing model with BFS and without BFS, the difference between upper and lower surface becomes maximum at 20% C. It is seen from the graph that a slightly increase in difference between the upper and lower surfaces observed from 60%C to 80%C between the optimum wing model with BFS and the optimum wing model without BFS.

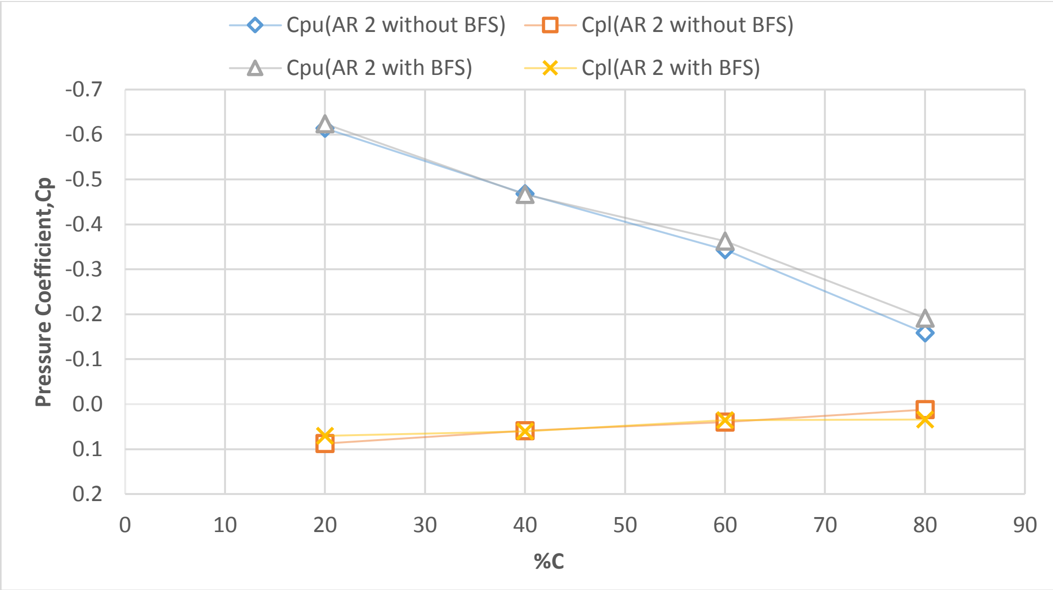

Figure 6.56: Cp distribution of segment D at 2^0 AOA

6.7.3 Pressure Distributions at 4˚ AOA of optimum wing models with BFS

Figures 6.57, 6.58, 6.59 and 6.60 represent the surface pressure distribution in terms of pressure coefficient of four segments (A, B, C and D) of optimum wing with and without BFS at 4˚ AOA. In the figures, both upper and lower surface pressure coefficient, C_{pu} and C_{pl} are plotted along the chord length (C).

From figure 6.57 it is observed that pressure difference between the upper and lower surface of optimum wing model with BFS of segment A is higher than the optimum wing model without BFS. The lower surface pressure decreases slowly from 20%C to 80%C. But it is seen that for optimum wing model the upper surface pressure is lower than the optimum wing model without BFS. It is also observed that the pressure difference between the two surfaces of optimum wing with BFS is higher than that of optimum wing model without BFS.

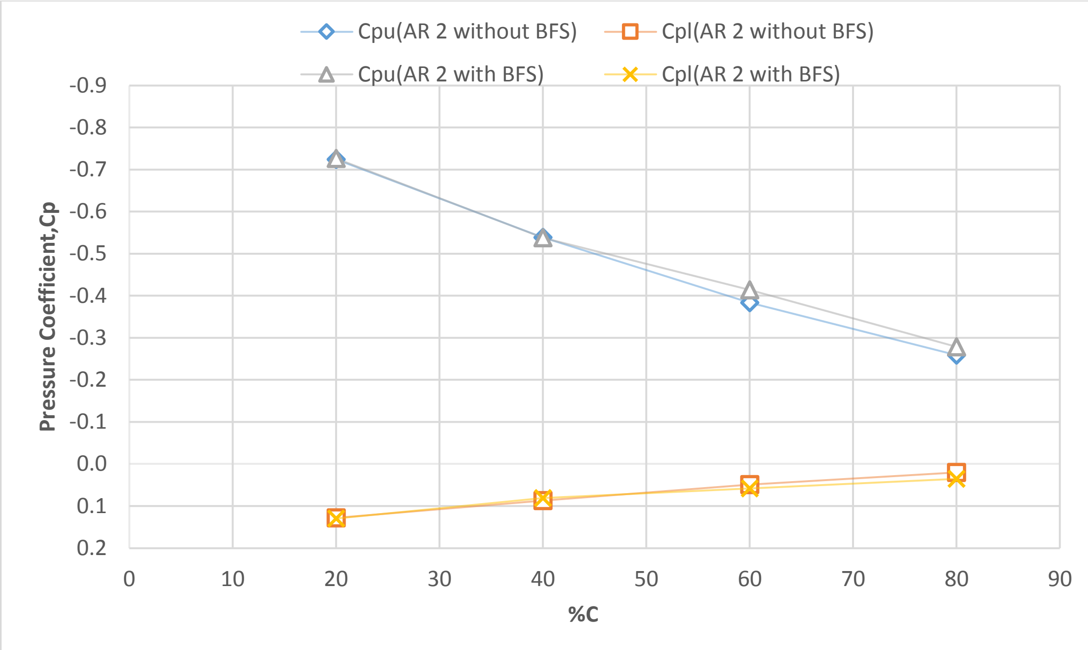

Figure 6.57: Cp distribution of segment A at 4^0 AOA

In figure 6.58, for segment B it is observed that the upper surface is having higher negative pressure than the lower surface of the respective optimum wing models. The difference between upper and lower surface pressure is observed lowest for optimum wing model without BFS. The upper surface pressure for all the wing models increases from leading edge to trailing edge. The pressure difference between upper and lower surfaces of optimum wing with BFS is higher than the optimum wing model without BFS. It also observed that for segment B the pressure difference between upper and lower surfaces are greater than segment A. The difference between upper and lower surface is highest at 20%C and it decreases from 20%C to 80%C.After 40%C the upper surface pressure of optimum wing with BFS is lower than the upper surface pressure of optimum wing model without BFS.

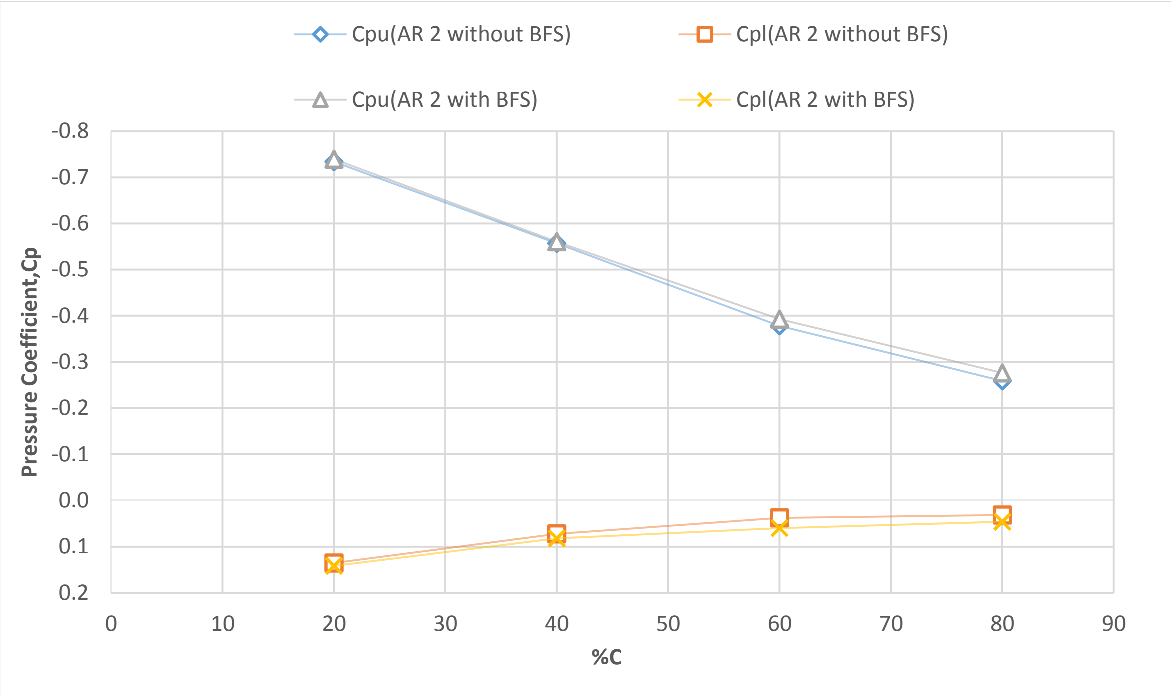

Figure 6.58: Cp distribution of segment B at 4^0 AOA

Figure 6.59 illustrates the surface pressure coefficients of segment C at 4˚ AOA for optimum wing with BFS and without BFS. It shows the similar characteristics as of segment B. But in segment C the pressure differences between the upper and lower surface for optimum wing with and without BFS are higher than the segments B's pressure differences.

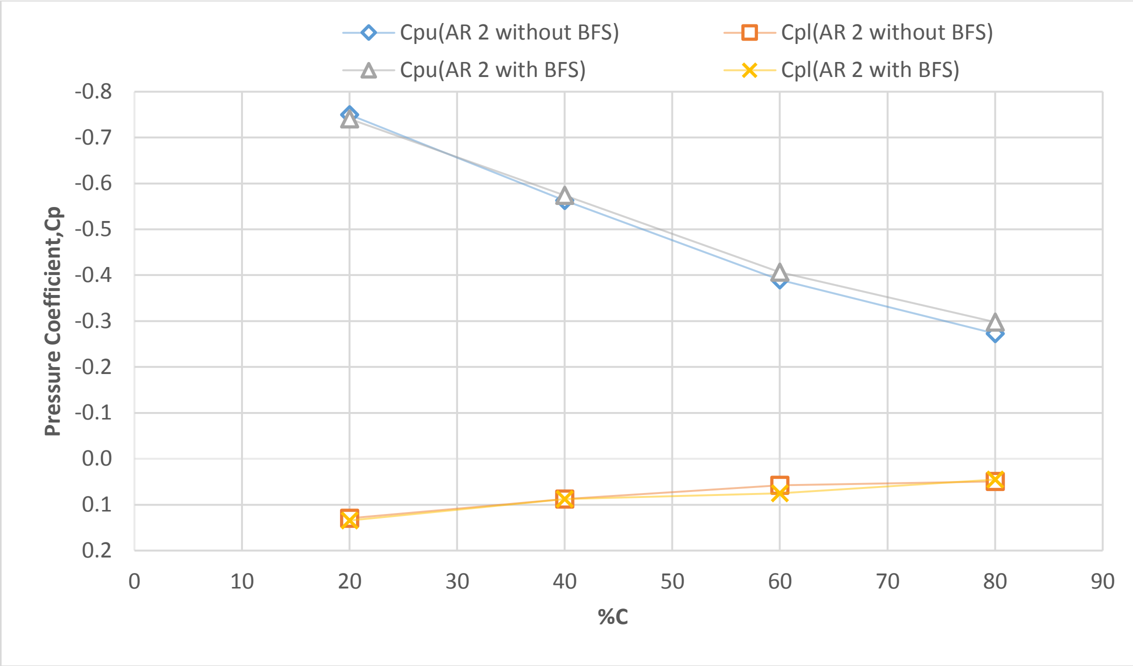

Figure 6.59: Cp distribution of segment C at 4^0 AOA

The surface pressure distributions for segment-D of optimum wing model with and without BFS at 4˚ angle of attack are shown in figure 6.60.From figure, it is observed that the difference between upper and lower surface pressures in segment-D is higher for optimum wing with BFS than the optimum wing without BFS. The difference between upper and lower surfaces become maximum at 20% C and lowest at 80%C.

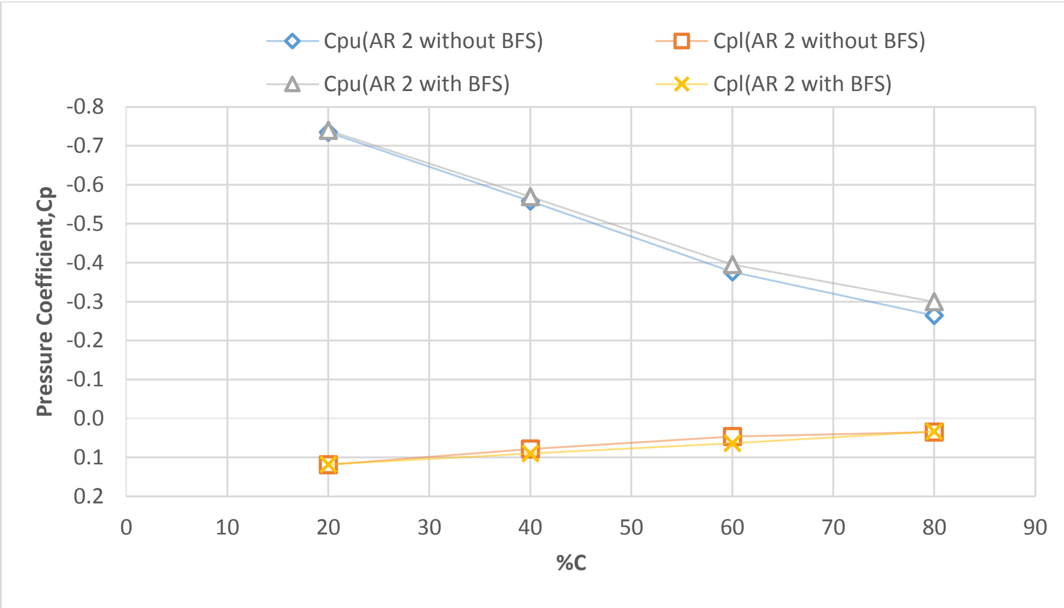

Figure 6.60: Cp distribution of segment D at 4^0 AOA

6.7.4 Pressure Distributions at 6˚ AOA for optimum wing model with BFS

Figures 6.61, 6.62, 6.63 and 6.64 represent the surface pressure distribution in terms of pressure coefficient of four segments (A, B, C and D) of optimum wing model with and without BFS at 8˚ AOA.

The surface pressure distributions for segment-A of optimum wing model with and without BFS at 6˚ angle of attack are shown in figure 6.61. From the figure it is seen that the upper surface of all wing models are having higher negative pressure than the lower surface pressure of the respective optimum wing models. The upper surface pressure increases gradually from leading edge to trailing edge. But lower surface pressure decreases slowly from leading edge to trailing edge. The upper surface pressure is observed to be lower for optimum wing model with BFS than the optimum wing model without BFS. The difference between the upper and lower surface pressure of optimum wing without BFS becomes lower than the optimum wing model with BFS. The largest difference between upper and lower surface is observed from 20% C to 40%C.

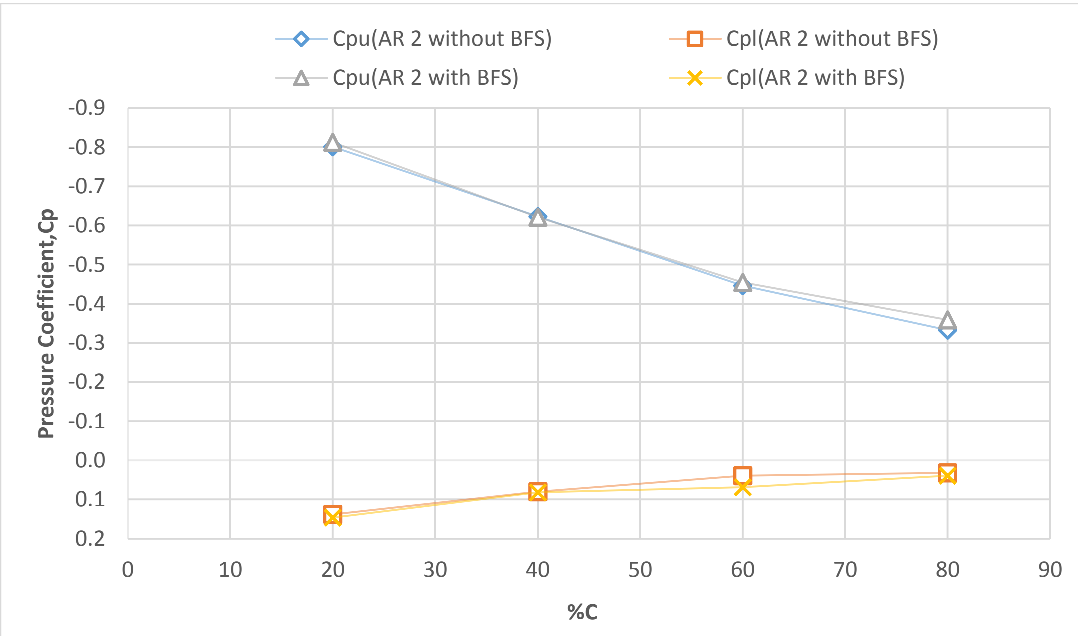

Figure 6.61: Cp distribution of segment A at 6^0 AOA

In figure 6.62, almost similar type of pressure distribution of optimum wing model for segment B are observed as in segment A. At segment B as well, the difference between upper and lower surface is observed maximum for optimum wing with BFS. It is also observed that the pressure difference between two surfaces of respective wing models is higher than that of segment A. There is slight increase of lower surface pressure is observed from the graph for the optimum wing with BFS from 40%C to 60%C. But the upper surface pressure of the optimum wing model with BFS is lower from 40%C to 60%C than the optimum wing model without BFS.

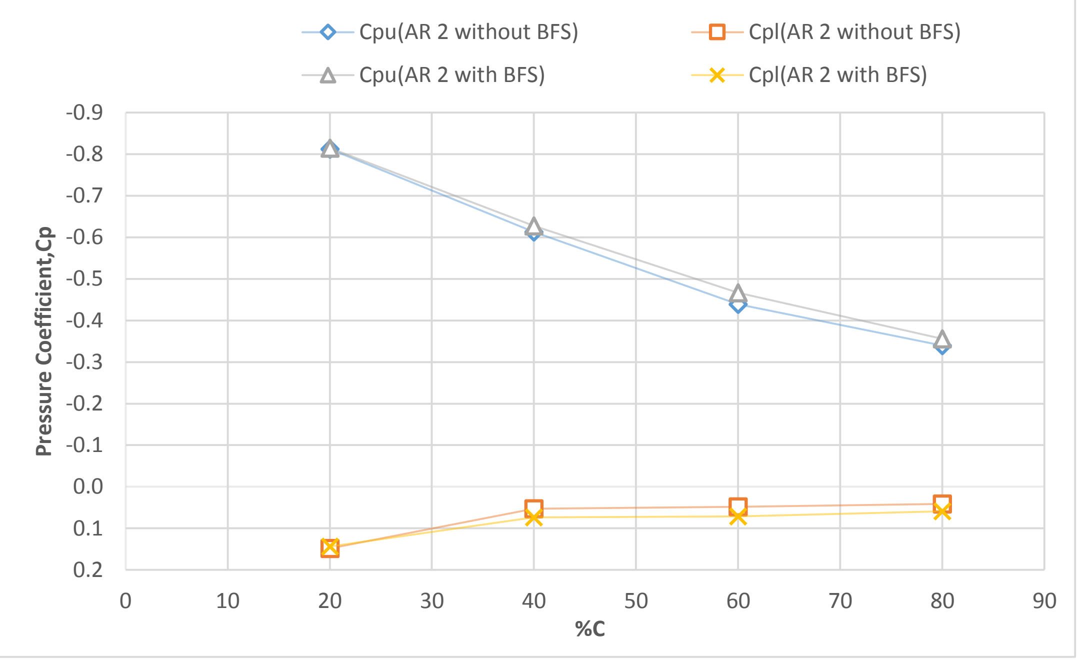

Figure 6.62: Cp distribution of segment B at 6^0 AOA

The surface pressure distributions for segment-C of optimum wing model at 6˚ angle of attack are shown in figure 6.63.From figure, it is observed that the difference between upper and lower surface pressures in segment-C is highest for optimum wing model with BFS. In segment-C, the pressure difference between two surfaces of respective wing models are higher than those of segment-B. The difference between upper and lower surfaces become maximum at 20% C and lowest at 80%C.From 40%C to 60%C upper surface pressures of optimum wing model with BFS is lower than the upper surface pressures of optimum wing model without BFS. The difference between the upper and lower surface pressure is higher for optimum wing with BFS than the optimum wing without BFS.

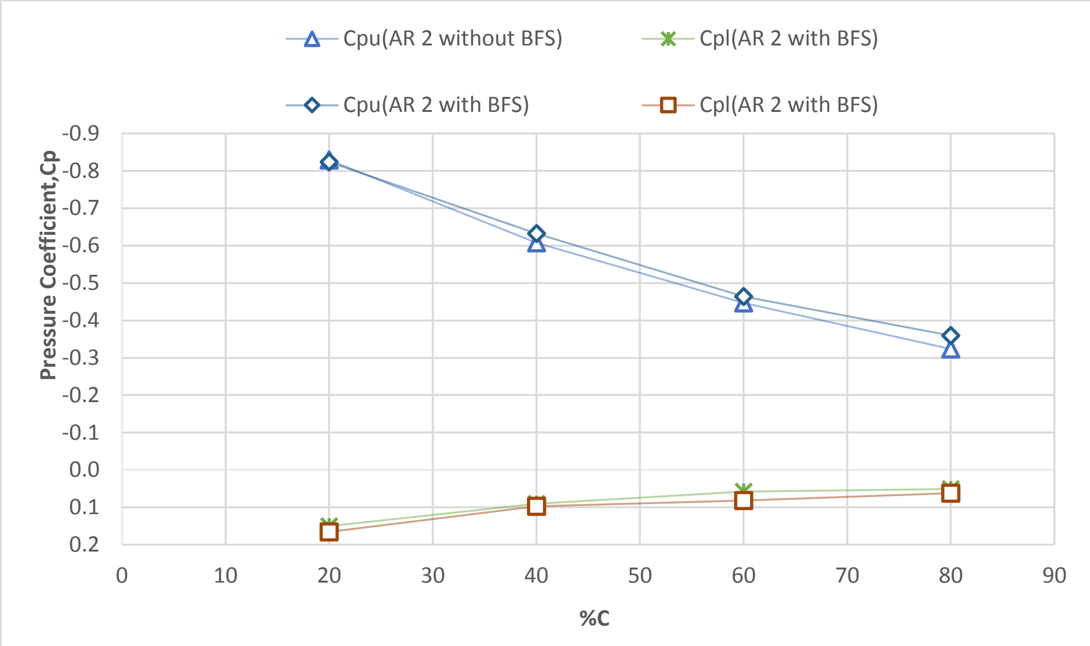

Figure 6.63: Cp distribution of segment C at 6^0 AOA

In figure 6.64, almost similar type of pressure distribution of optimum wing model for segment D are observed as in segment C. At segment D as well, the difference between upper and lower surface is observed maximum for optimum wing with BFS. The difference between upper and lower surfaces become at lowest at 80%C.From 40%C to 60%C upper surface pressures of optimum wing model with BFS is lower than the upper surface pressures of optimum wing model without BFS. The difference between the upper and lower surface pressure is higher for optimum wing with BFS than the optimum wing without BFS.

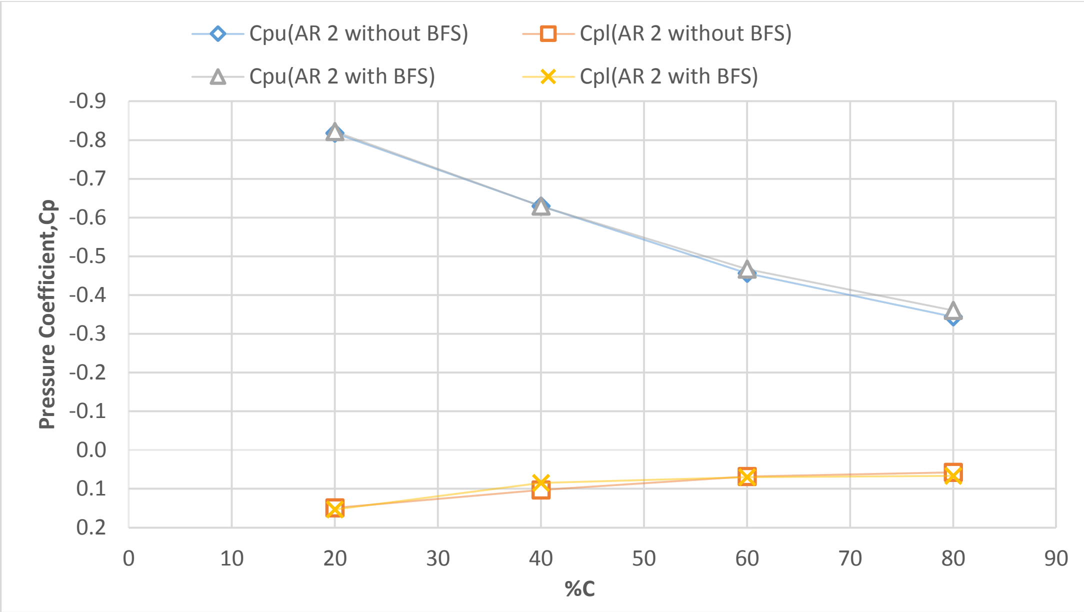

Figure 6.64: Cp distribution of segment D at 6^0 AOA

6.7.5 Pressure Distributions at 8˚ AOA for optimum wing model with BFS

Figures 6.65, 6.66, 6.67 and 6.68 represent the surface pressure distribution in terms of pressure coefficient of four segments (A, B, C and D) of optimum wing with and without BFS at 8˚ AOA.

The surface pressure distributions for segment-A of wing models at 8˚ angle of attack are shown in Figure 6.65. It is seen that the upper surface of the optimum wing model with and without BFS are having higher negative pressure than the lower surface pressure of the respective wing models. For the optimum wing model with and without BFS, upper surface pressure increases gradually from 20%C to 80%C. But lower surface pressure decreases slowly from leading edge to trailing edge. The difference between the upper and lower surface pressure of optimum wing with BFS becomes higher than the optimum wing without BFS. For the two wing models, the largest difference between upper and lower surface is observed at 20% C. The difference is decreasing gradually from leading edge to trailing edge and it is lowest at 80%C.

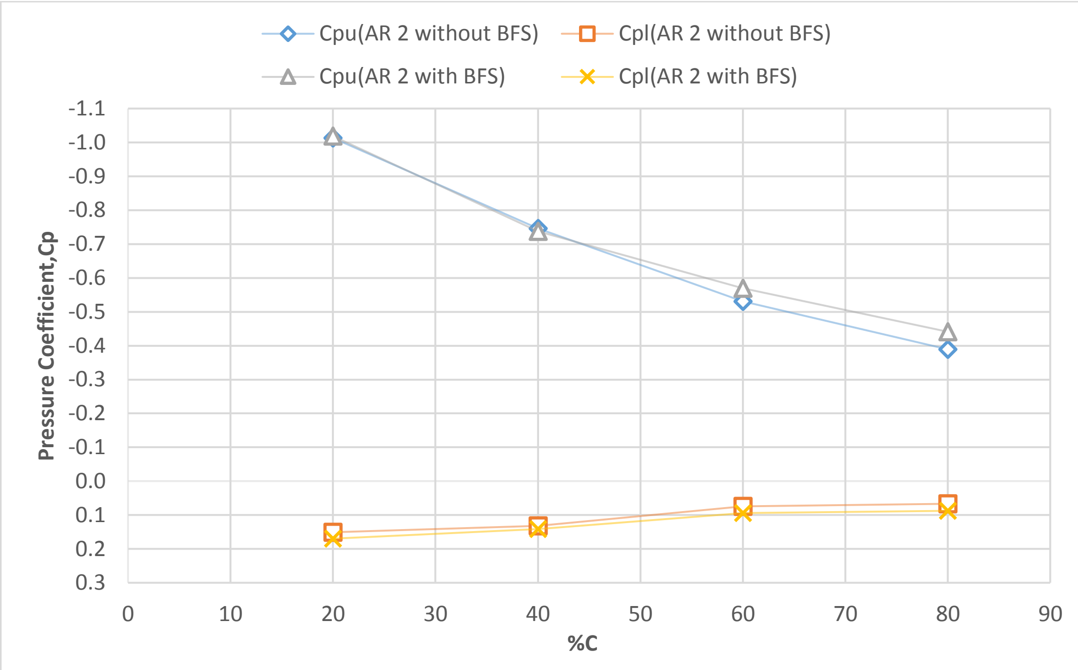

Figure 6.65: Cp distribution of segment A at 8^0 AOA

In all the other three segments(B,C,D) as shown in figure 6.66,figure 6.67 and figure 6.68 at 8° angle of attack, it is observed that the pressure difference between upper and lower surface of all wing models are higher compared to those at previous angle of attack. Among two optimum wing models with and without BFS, optimum wing model with BFS is having higher pressure difference between upper and lower surfaces in all segments. For all three figures the lower surface pressure difference decreases gradually from 20 %C to 80%C and upper surface pressure increases gradually from leading edge to trailing edge. The said difference is highest in both segment B and segment C as shown in Figures 6.62 and 6.63.It is also seen that the upper surface pressure of optimum wing model with BFS is lower than the upper surface pressure of optimum wing model without BFS from 40%C to 80%C.

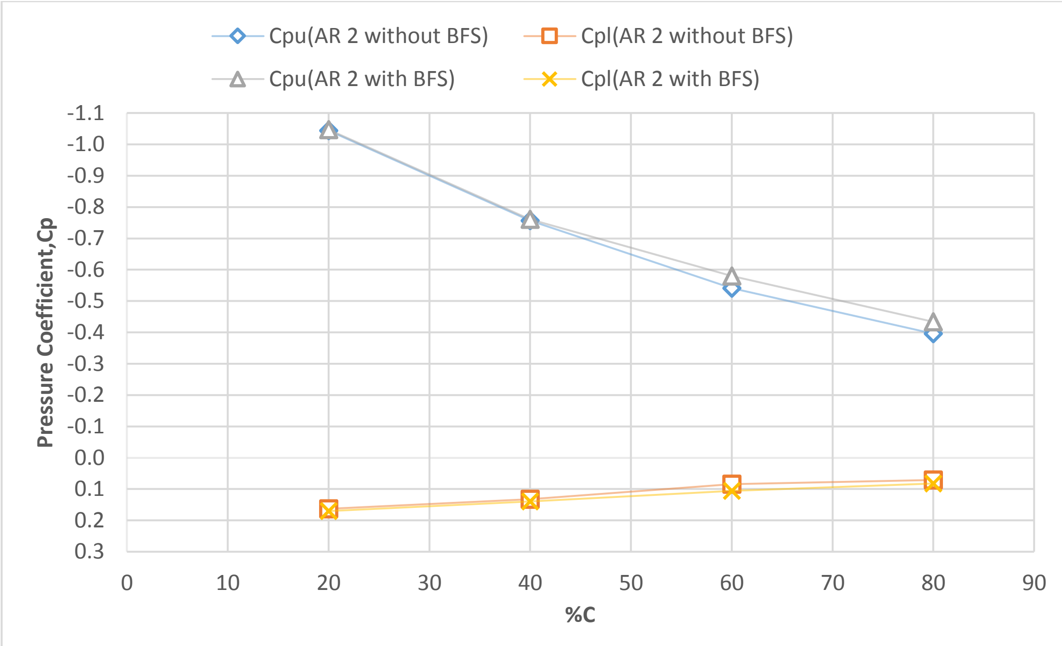

Figure 6.66: Cp distribution of segment B at 8^0 AOA

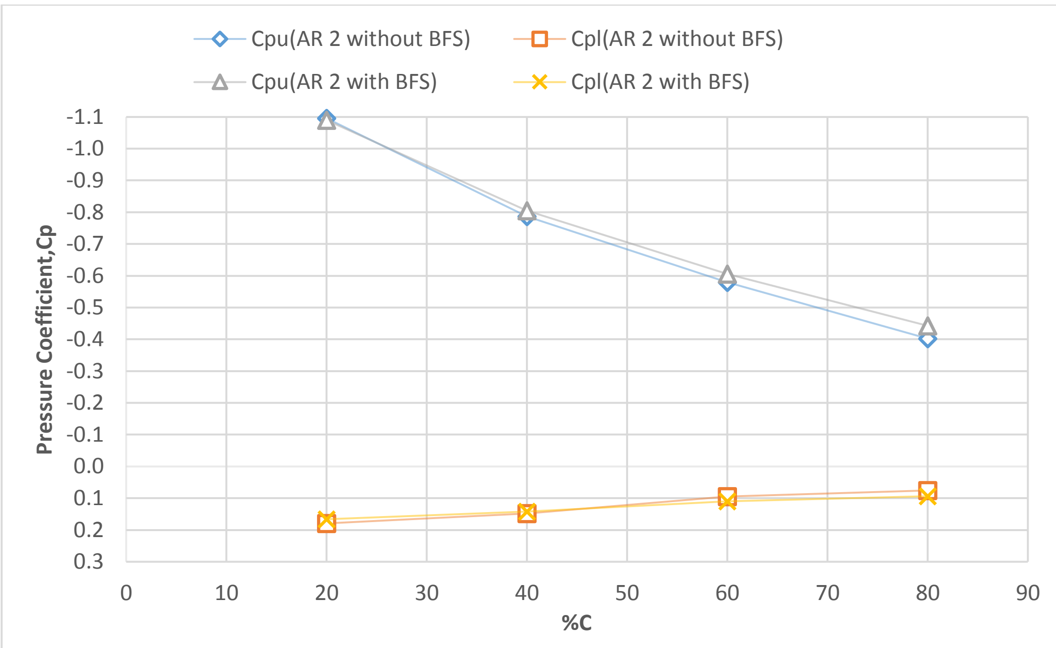

Figure 6.67: Cp distribution of segment C at 8^0 AOA

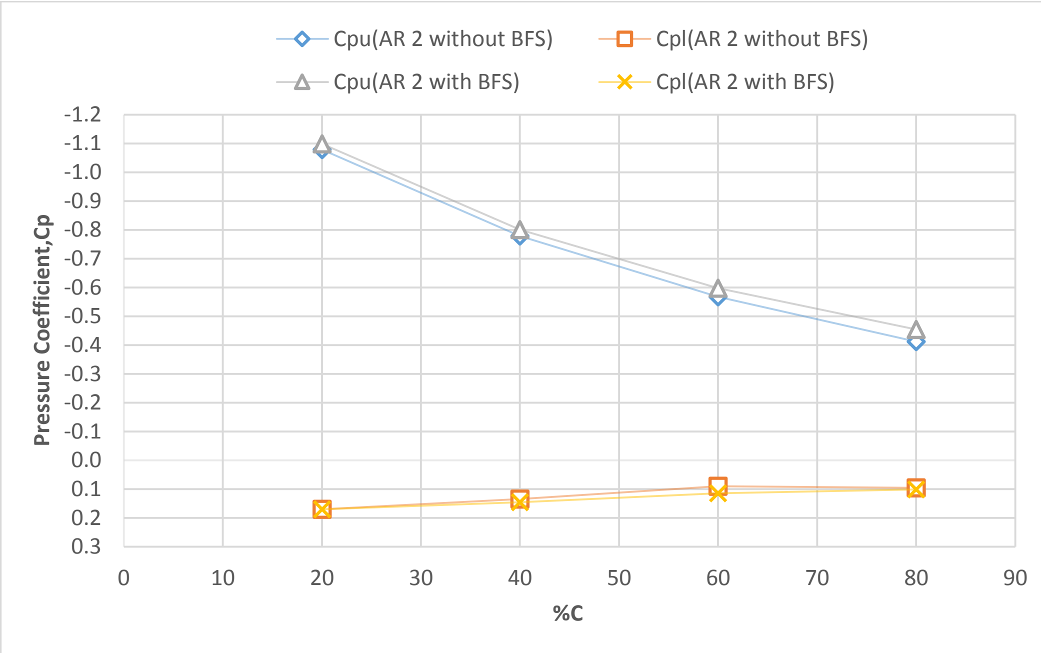

Figure 6.68: Cp distribution of segment D at 8^0 AOA

6.7.6 Pressure Distributions at 10˚ AOA of optimum wing with BFS

Figures 6.69, 6.70, 6.71 and 6.72 represent the surface pressure distribution in terms of pressure coefficient of four segments (A, B, C and D) of optimum wing model with and without BFS at 10˚ AOA.

The surface pressure distributions for segment-A of optimum wing model with and without BFS at 10˚ angle of attack are shown in figure 6.69. From the figure, it is observed that upper surfaces of the two wing models are having higher negative pressure than the lower surface pressure of the respective wing models. The lower surface pressure decreases slowly from 20% C to 80% C. The upper surface pressure increases gradually from leading edge to trailing edge. For optimum wing with BFS, upper surface pressure increases and lower surface pressure decreases from leading edge to the trailing edge. But the upper surface pressure is lower for optimum wing with BFS than the optimum wing without BFS. As a result, the difference between upper and lower surface pressure is observed maximum for optimum wing with BFS and the highest difference is achieved at 20%C.

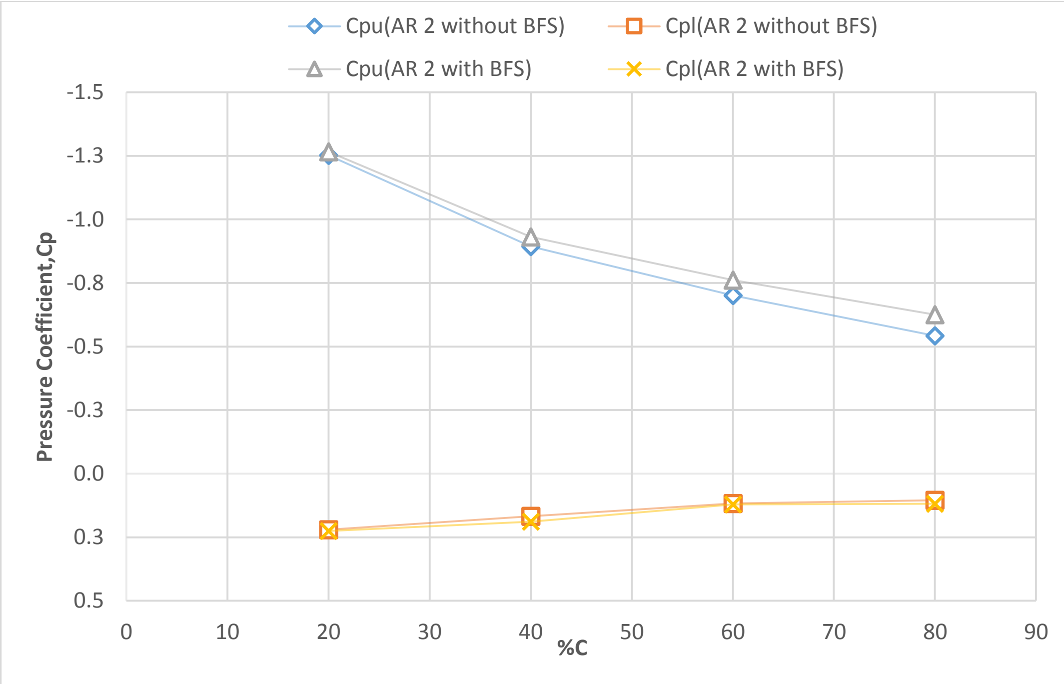

Figure 6.69: Cp distribution of segment A at 10^0 AOA

In figure 6.70, figure 6.71 and figure 6.72 almost similar type of pressure distribution of optimum wing model for the other three segments (B, C, D) are observed as in segment A. At all the three segments (B, C, D), the difference between upper and lower surface is observed maximum for optimum wing with BFS. It is also observed that the pressure difference between two surfaces of respective wing models is higher for segment B and segment C than that of segment A. There is slight increase of lower surface pressure is observed from the graph for the optimum wing with BFS from 40%C to 60%C.But the upper surface pressure of the optimum wing model with BFS is lower from 40%C to 60%C than the optimum wing model without BFS. In figure 6.68,it is seen that the lower surface pressures of the optimum wing model with BFS is higher than the lower surface pressures of the optimum wing model without BFS from 40%C to 80%C.

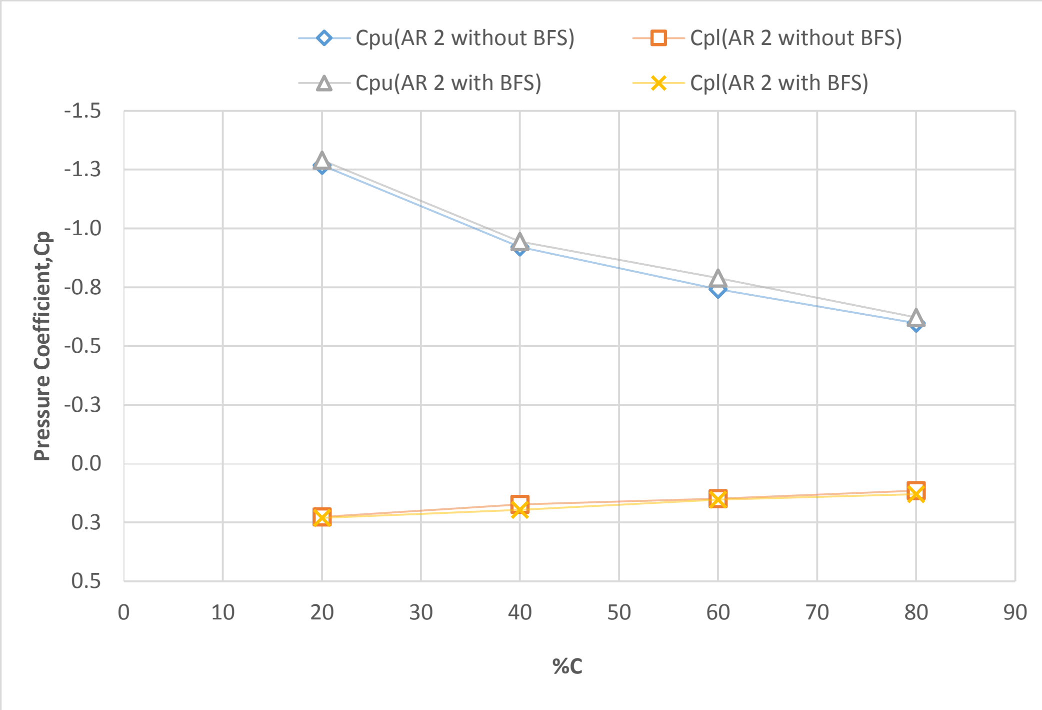

Figure 6.70: Cp distribution of segment B at 10^0 AOA

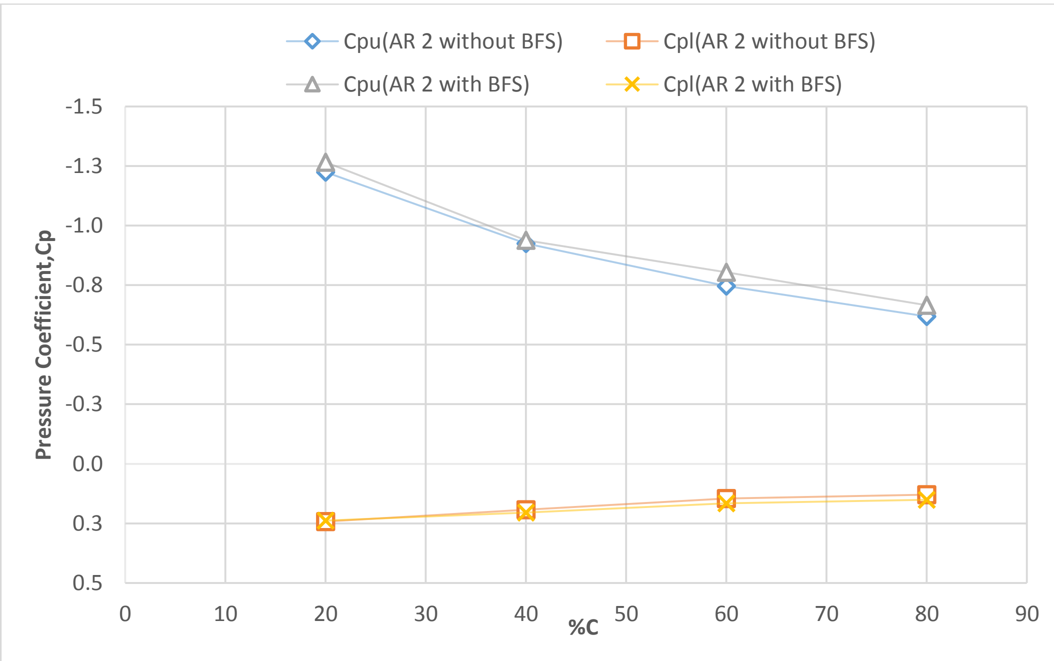

Figure 6.71: Cp distribution of segment C at 10^0 AOA

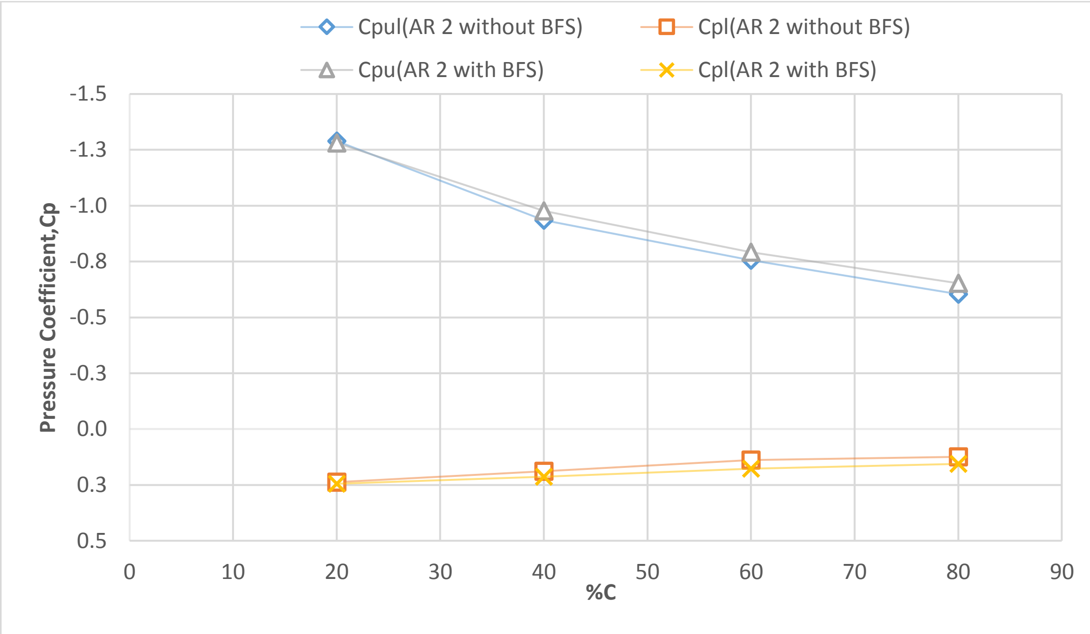

Figure 6.72: Cp distribution of segment D at 10^0 AOA

6.7.7 Pressure Distributions at 12˚ AOA of optimum wing with BFS

Figures 6.73, 6.74, 6.75 and 6.76 represent the surface pressure distribution in terms of pressure coefficient of four segments (A, B, C and D) of the optimum wing model with and without BFS at 12˚ AOA.

Pressure distribution along the chord for segment A is shown in figure 6.73. From the graph, it is observed that upper surface pressure of both the optimum wing model with and without BFS increases from 20% C to 60% C sharply, then increases slowly up to 80% C. The lower surface positive pressure gradually decreases up to from 20% C to 80% C. The largest upper and lower surface pressure difference occurs at 20% of C for both of the wing models which reduces gradually towards the trailing edge. Optimum wing with BFS has the higher surface pressure difference between upper and lower surfaces than the optimum wing model without BFS. From the graph it is seen that, for AOA 12˚ the pressure differences between upper and lower surfaces is higher than for AOA 10˚.

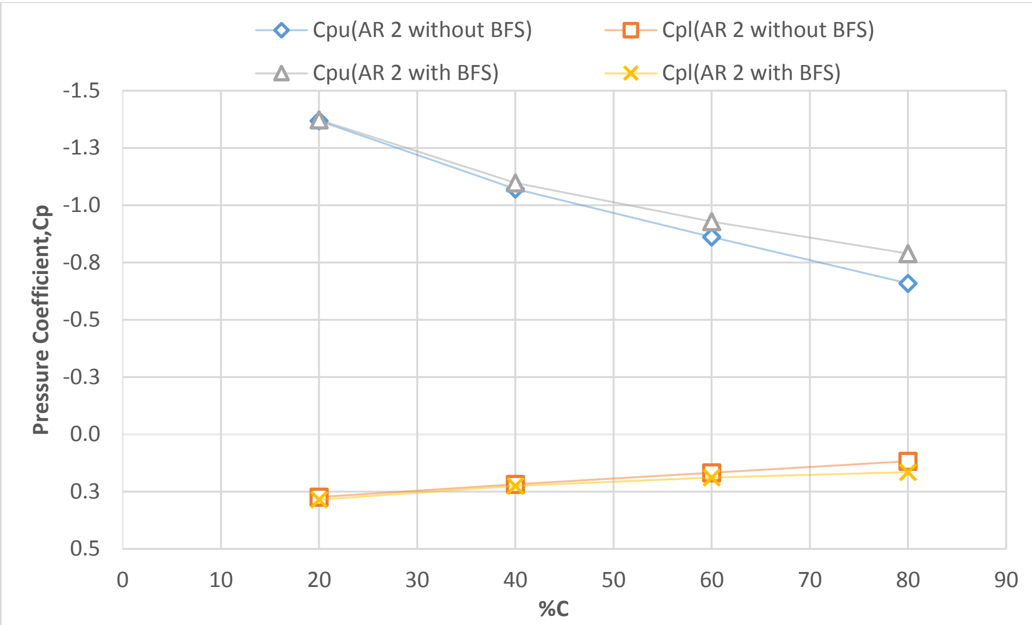

Figure 6.73: Cp distribution of segment A at 12^0 AOA

Figures 6.74 shows the surface pressure distribution of segment B for optimum wing model with and without BFS at 12˚ angle of attack. In segment B, upper surface pressure increases gradually from leading edge to trailing edge and lower surface pressure decreases gradually from leading edge to trailing edge. The difference between the upper and lower surface pressures of segment B is higher than the difference between the pressures of segment A. The highest-pressure difference is observed near the leading edge at 20 %C and smallest pressure difference is obtained at 80%C. From 40%C to 80%C the upper surface pressure of optimum wing model with BFS is lower than the optimum wing model without BFS.

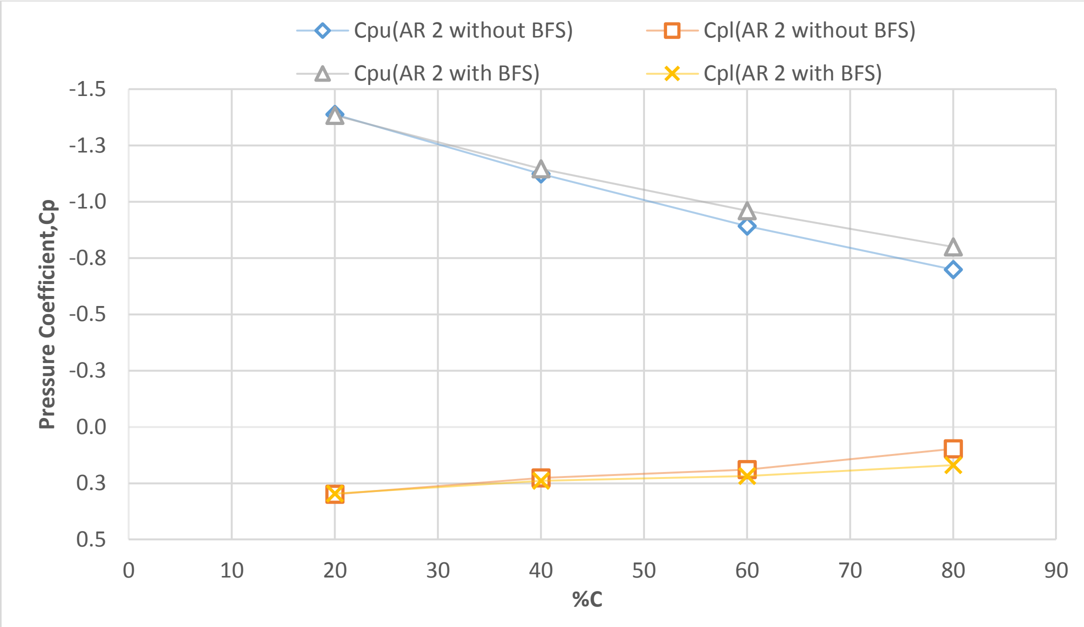

Figure 6.74: Cp distribution of segment B at 12^0 AOA

In segment C, upper surface pressure increases gradually from 20% C to 80% C for both the optimum wing model with and without BFS as shown in figure 6.75. The lower surface pressure is highest for optimum wing with BFS. From the graph it is seen that the difference between the upper and lower surface pressures of segment C is lower than the difference between the pressures of segment B. The upper surfaces pressure increases gradually form 20 %C to 80 %C and lower surface pressure decreases gradually from 20 %C to 80%C.

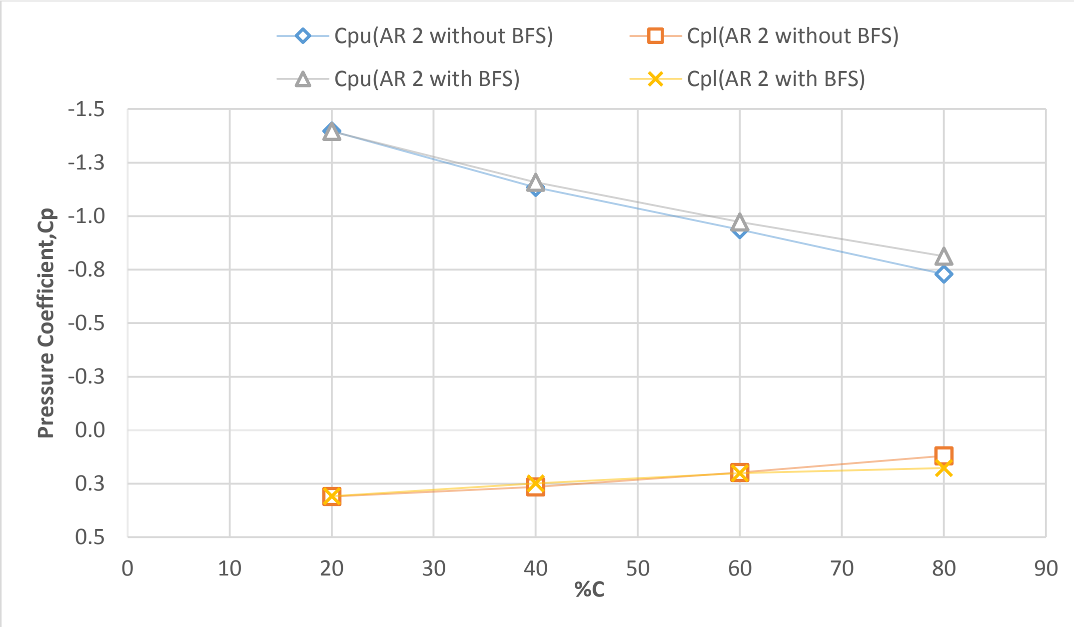

Figure 6.75: Cp distribution of segment C at 12^0 AOA

In segment D as shown in figure 6.76, upper surface pressure increases gradually and lower surface pressure decreases slowly from leading edge to trailing edge. From the figures, it is also observed that overall pressure difference between the upper and lower surface of optimum wing with BFS is higher than that of without BFS. The highest-pressure difference is achieved at 20 %C. The upper surface pressure of the optimum wing without BFS is higher than the upper surface pressure of the optimum wing with BFS. The lowest pressure difference between the upper and lower surface is obtained at 80%C.

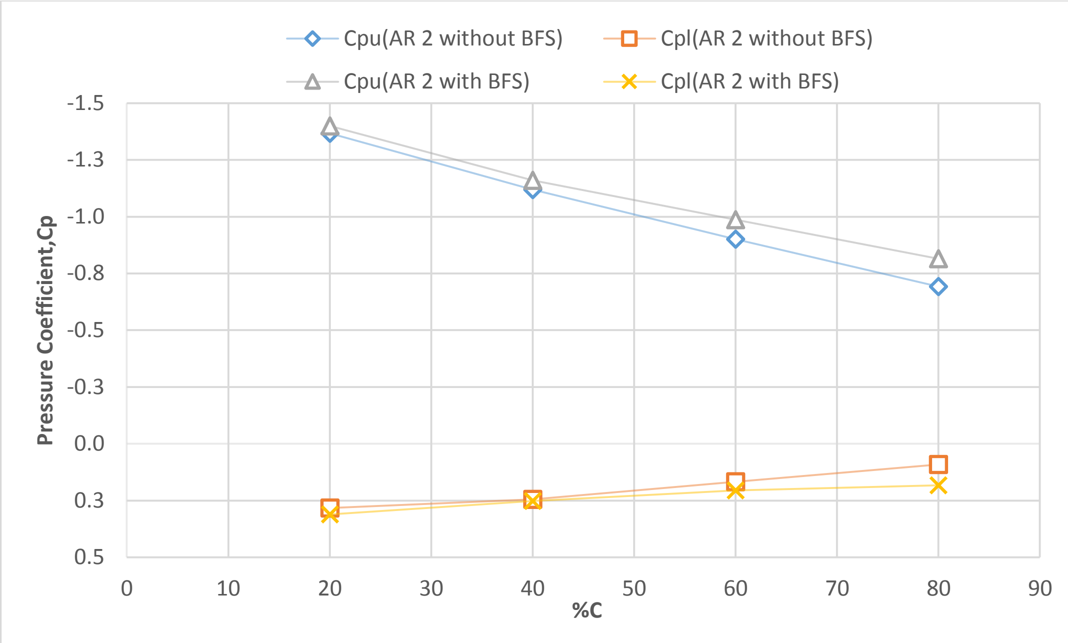

Figure 6.76: Cp distribution of segment D at 12^0 AOA

6.7.8 Pressure Distributions at 14˚ AOA of optimum wing with BFS

The surface pressure distributions along the chord length at 14˚ angle of attack for four segments of wing models are shown in Figures 6.77, 6.78, 6.79 and 6.80.

From all the four figures, it is observed that in all segments the difference between the upper surface and lower surface pressures of the optimum wing model with and without BFS are much higher than the difference between the upper surface and lower surface pressures at previous angle of attack (12˚ AOA) as shown in the previous figures. Upper surface pressures of the models tend to increase at a much slower rate compared to the upper surface pressure rise at smaller angle of attack. The surface pressure difference between upper and lower surface of wing model with and without BFS is highest at 20%C which decreases slowly up to the trailing edge in four segments. In figure 6.78 and figure 6.79 it is observed that, the overall differences between upper and lower surface pressure of the optimum wing model with and without BFS are observed maximum at segment A and segment B respectively. This phenomenon is also same for segment C and segment D as shown in figure 6.79 and figure 6.80.The upper surface pressure is much lower for the optimum wing with BFS than the optimum wing without BFS which is observed in all the four figures from

40%C to 60%C.The lower surface pressures also higher for the optimum wing with BFS than the optimum wing without BFS.

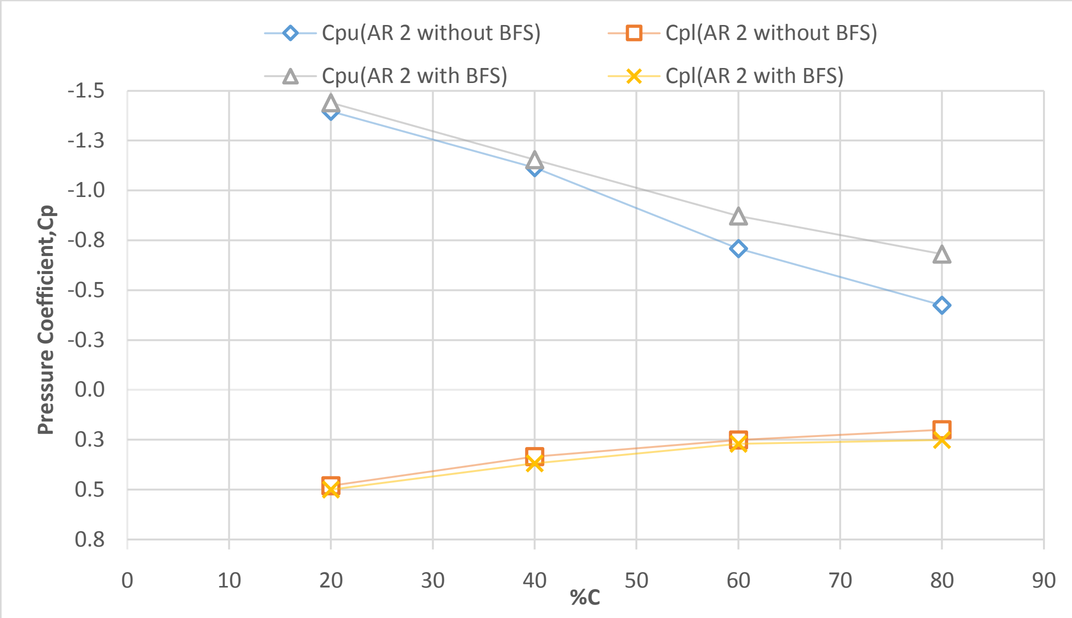

Figure 6.77: Cp distribution of segment A at 14^{0} AOA

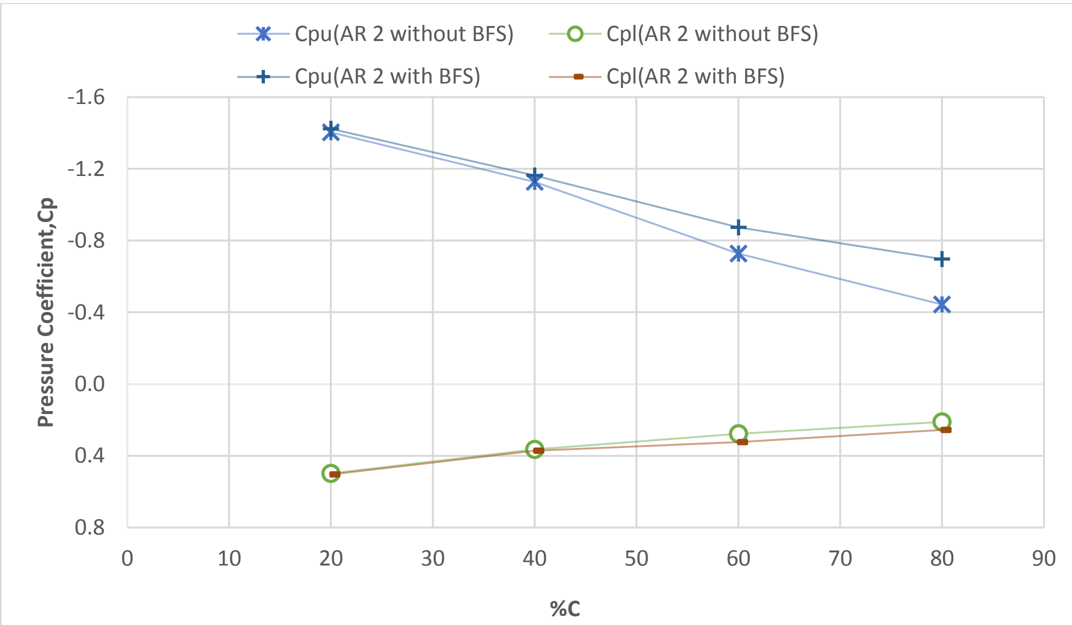

Figure 6.78: Cp distribution of segment B at 14^{0} AOA

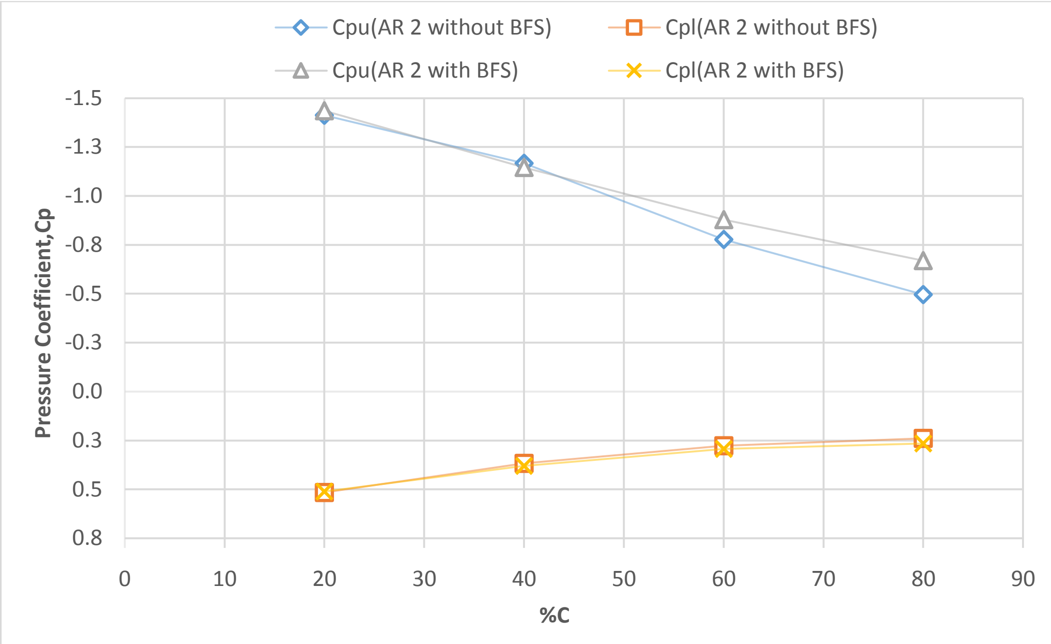

Figure 6.79: Cp distribution of segment C at 14^0 AOA

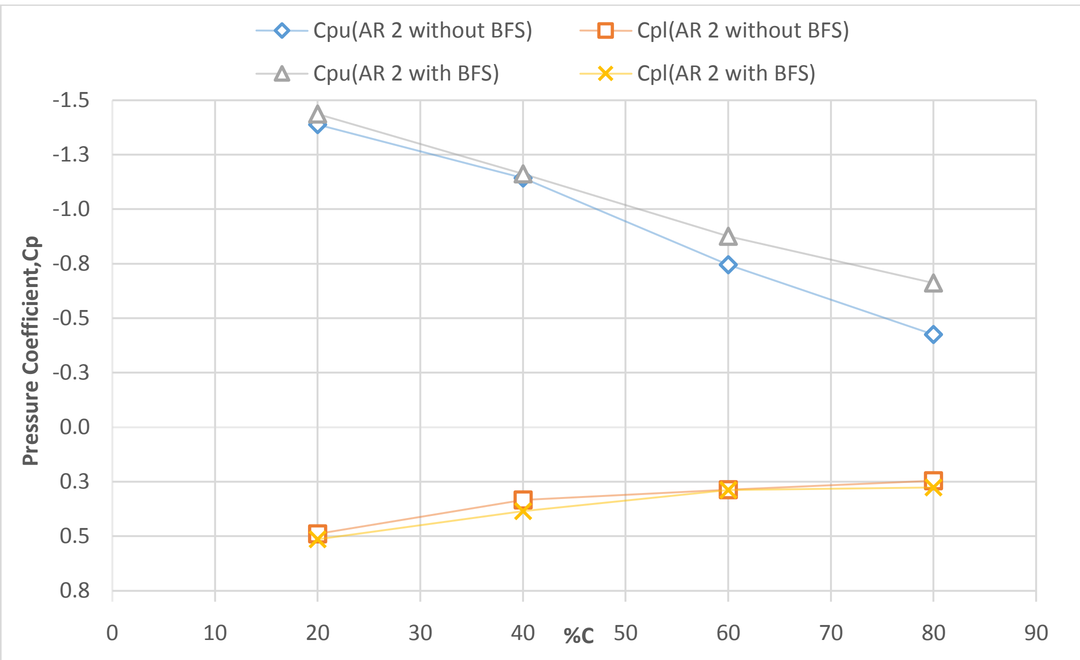

Figure 6.80: Cp distribution of segment D at 14^0 AOA

6.7.9 Pressure distribution at 16˚ AOA of optimum wing with BFS

Figures 6.81, 6.82, 6.83 and 6.84 represent the surface pressure distribution in terms of pressure coefficient of four segments (A, B, C and D) of optimum wing with and without BFS at 16˚ AOA. In the figures, both upper and lower surface pressure coefficient, C_{pu} and C_{pl} are plotted along the chord length (C).

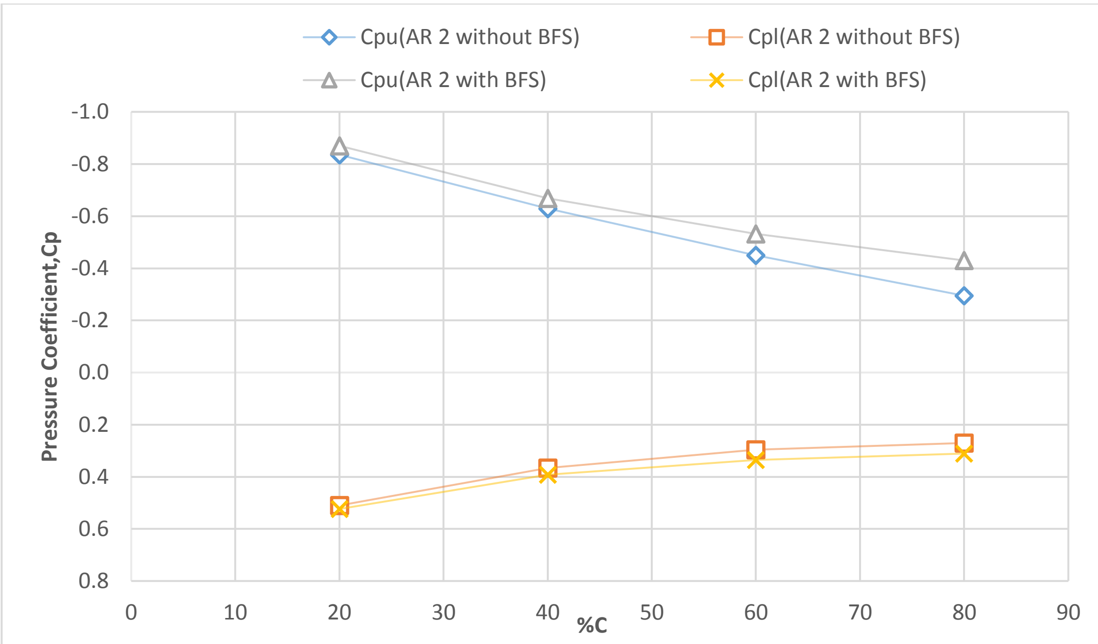

Figure 6.81: Cp distribution of segment A at 16^0 AOA

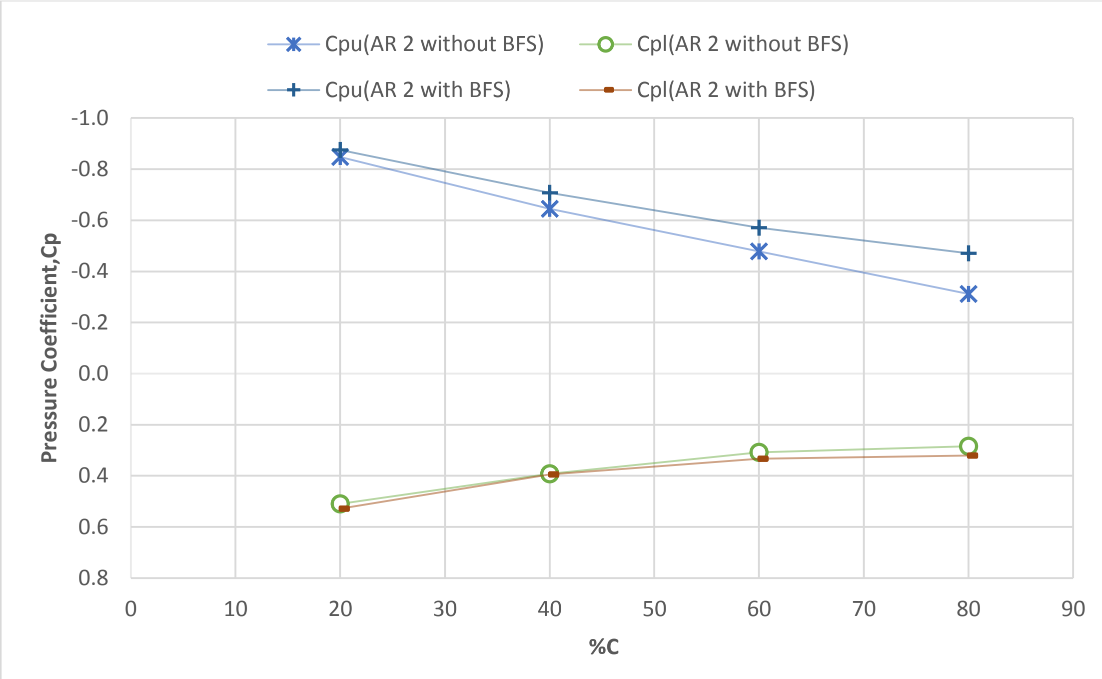

Figure 6.82: Cp distribution of segment B at 16^0 AOA

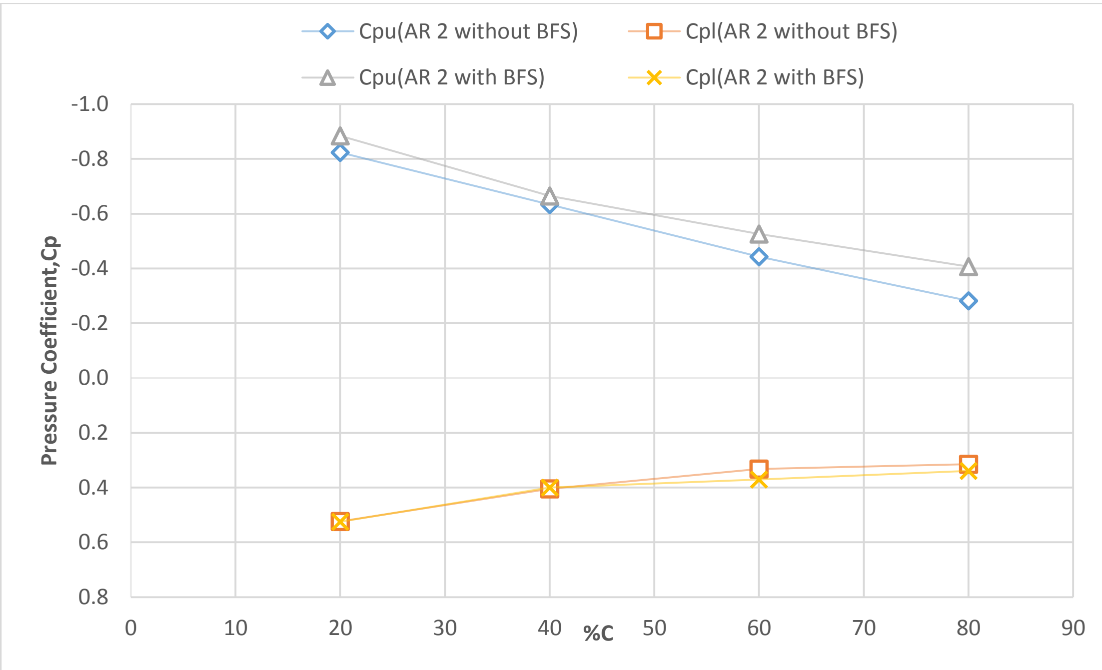

Figure 6.83: Cp distribution of segment C at 16^0 AOA

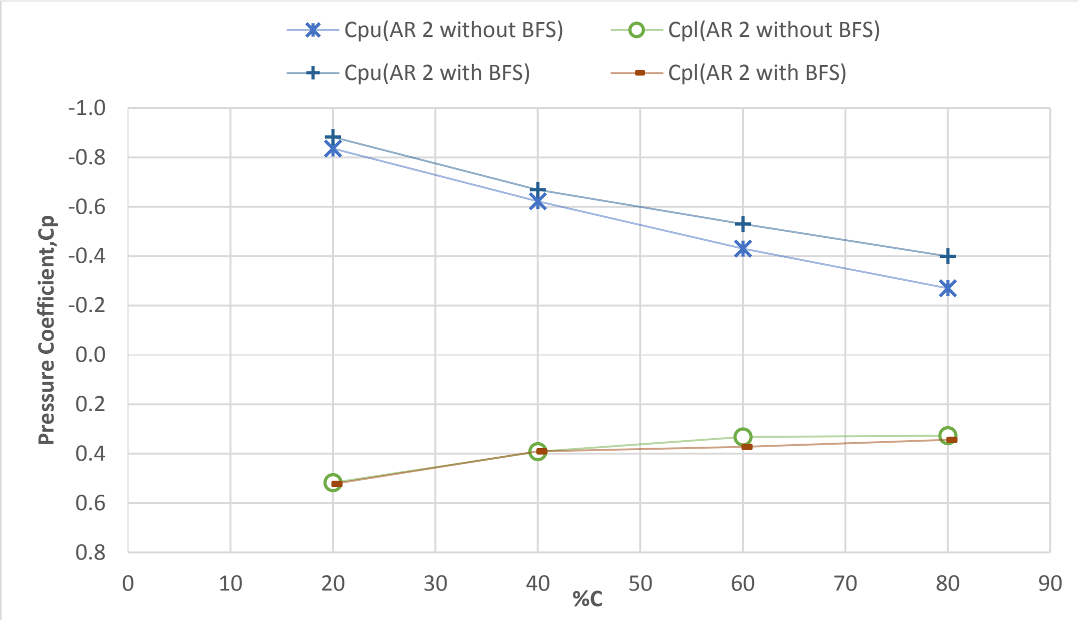

Figure 6.84: Cp distribution of segment D at 16^0 AOA

In all the four segments at 16° angle of attack, it is observed that the pressure difference between upper and lower surface of all wing models are lower compared to those at previous angle of attack. Among four wing models, wing model with BFS is having higher pressure difference between upper and lower surfaces in all segments. For both the optimum wing model with and without BFS as shown in all figures the lower surface pressure decreases gradually from 20 %C to 80%C and upper surface pressure increases gradually from leading edge to trailing edge. The said difference is highest in both segment B and segment C as shown in Figures 6.82 and 6.83. It is also seen that the lower surface pressure for all the segments is lowest for wing model without BFS and highest for wing model with BFS.

6.7.10 Pressure Distributions at 18˚ AOA of optimum wing with BFS

The surface pressure distributions along the chord length at 18˚ angle of attack for four segments (A, B, C, D) of optimum wing model with and without BFS are shown in figures 6.85, 6.86, 6.87 and 6.88.

From all the four figures, it is observed that in all segments the upper surface pressures of the wing models are much higher than the upper surface pressure at previous angle of attack (16˚ AOA) as shown in the previous figures. The surface pressure difference between upper and lower surface of wing models is highest at 20% of C which decreases slowly up to the trailing edge in four segments. In figure 6.85 and Figure 6.86 it is observed that, the overall differences between upper and lower surface pressure of optimum wing with BFS is observed maximum at segment A and segment B respectively. This phenomenon is also same for segment C and segment D as shown in figure 6.87 and figure 6.88. For optimum wing model with BFS, the upper surface pressures in all the segments as shown in the figures are lower than the optimum wing model without BFS. But the pressure differences between the upper and lower surfaces is higher for optimum wing model with BFS than the optimum wing model without BFS. From 40%C to 80%C the pressure difference shows highest value between the optimum wing model with BFS and the optimum wing model without BFS.

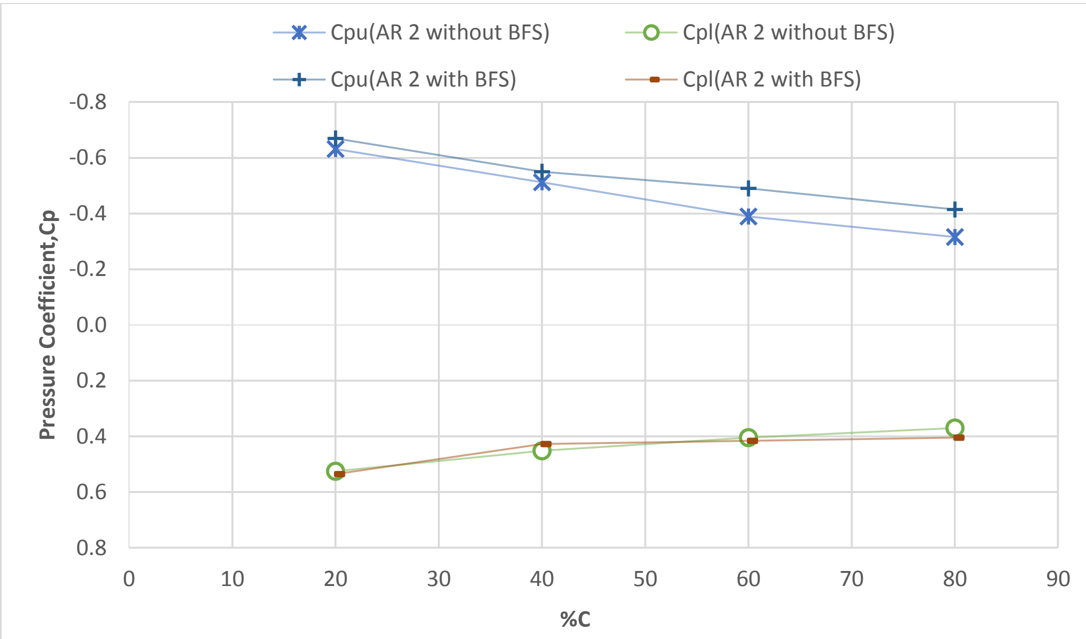

Figure 6.85: Cp distribution of segment A at 18^0 AOA

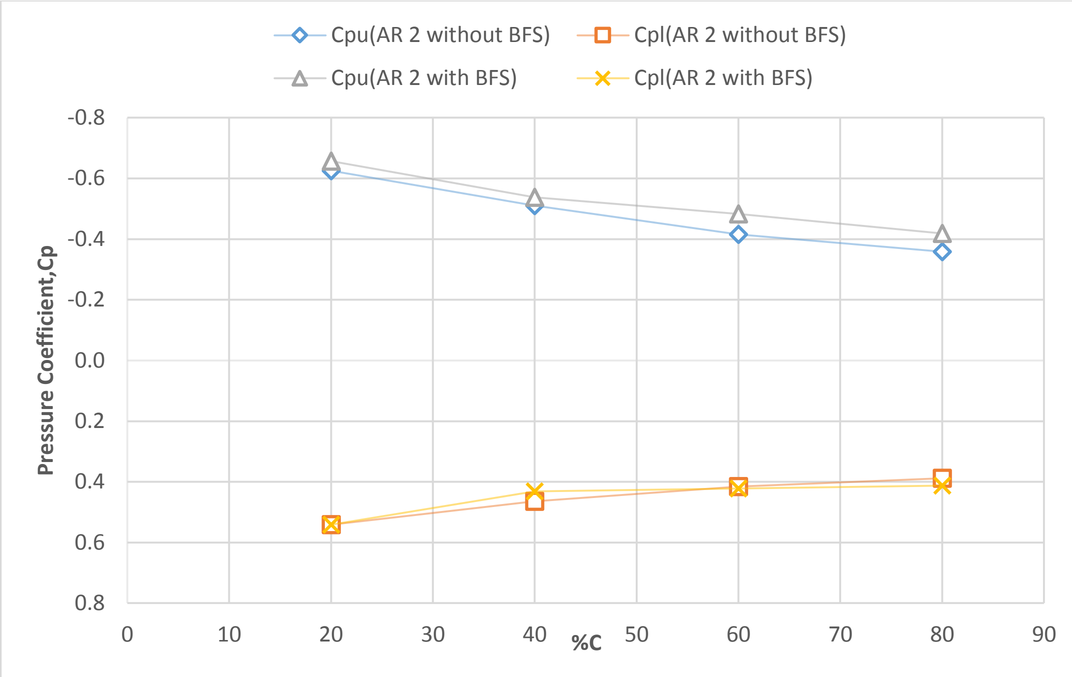

Figure 6.86: Cp distribution of segment B at 18^0 AOA

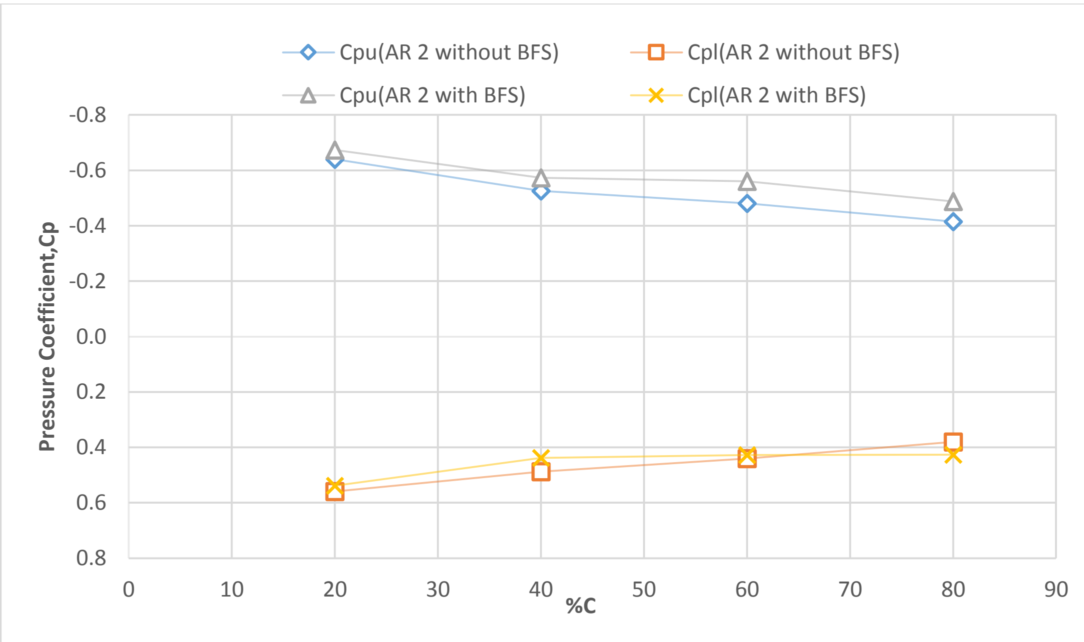

Figure 6.87: Cp distribution of segment C at 18^0 AOA

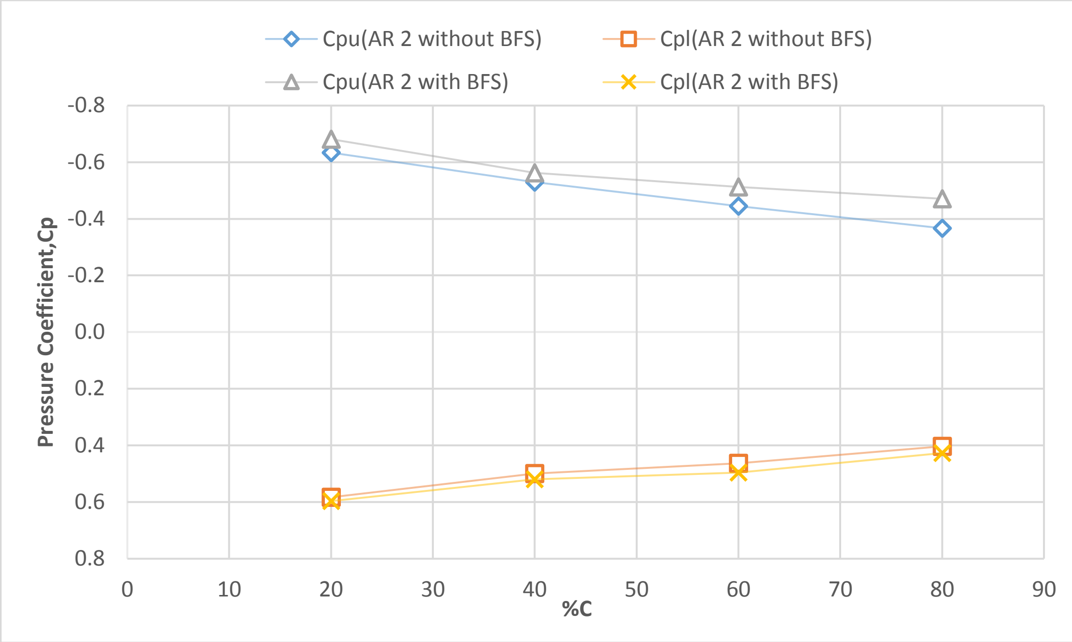

Figure 6.88: Cp distribution of segment D at 18^0 AOA

From figures 6.85, 6.86, 6.87 and 6.88, it is also observed that pressure difference between upper and lower surfaces of wing models are higher in segment B and segment C compared to the pressure difference of the surfaces in segment A. Another observation from the figures is that the upper and lower surface pressures of all wing models follow almost similar pattern in four segments and also the upper surface pressure changes very slowly from 60%C to 80%C for optimum wing model with BFS. It is also seen from the four figures that the lower surface pressure is highest for optimum wing model with BFS in all segments from 40%C to 80 %C.

6.7.11 Pressure distribution at 20˚ AOA

Figures 6.89, 6.90, 6.91 and 6.92 represent the surface pressure distribution in terms of pressure coefficient of four segments (A, B, C and D) of optimum wing model with and without BFS at 20˚ AOA. In the figures, both upper and lower surface pressure coefficient, C_{pu} and C_{pl} are plotted along the chord length (C). For all segments at 20˚ AOA both the upper surface pressure and lower surface pressure is larger than the previous angle of attack (18˚)

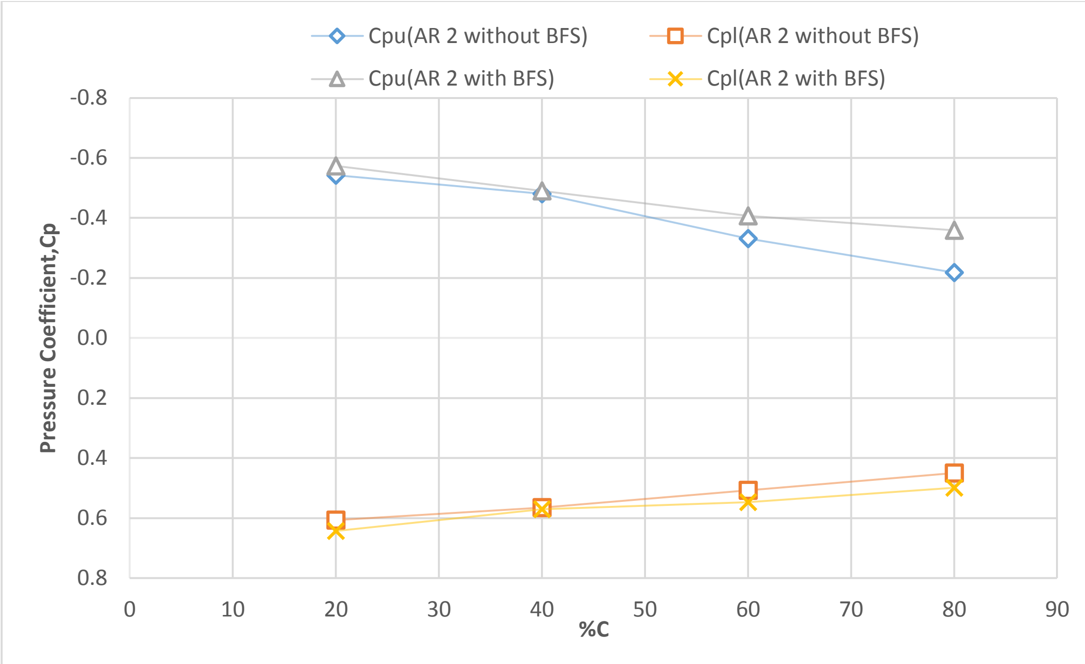

Figure 6.89: Cp distribution of segment A at 20^0 AOA

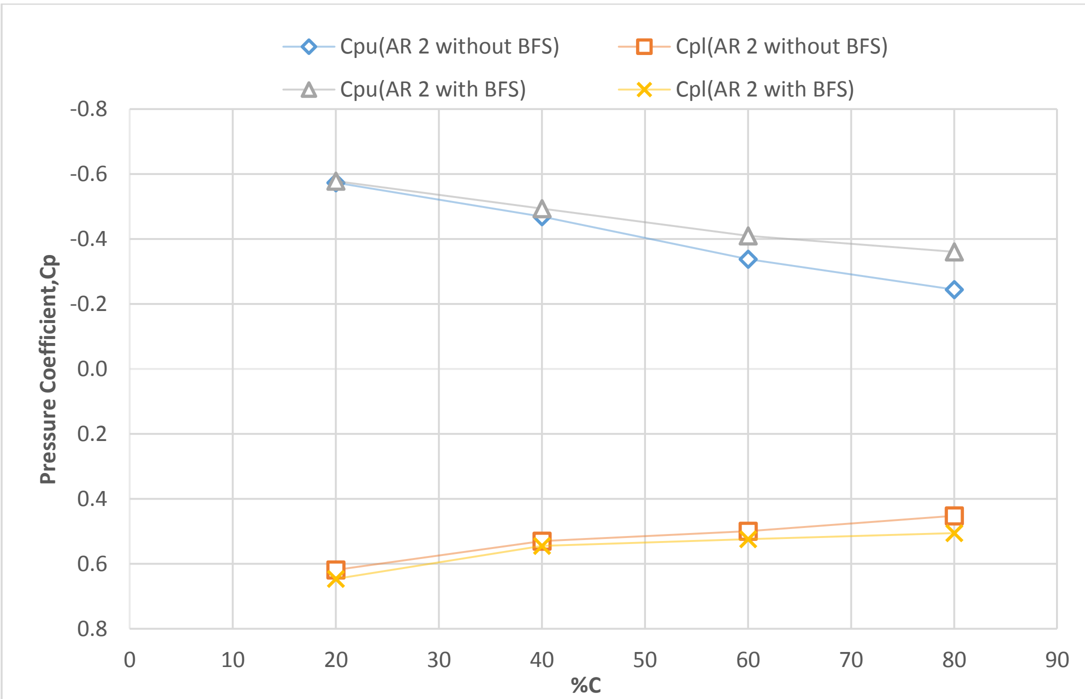

Figure 6.90: Cp distribution of segment B at 20^0 AOA

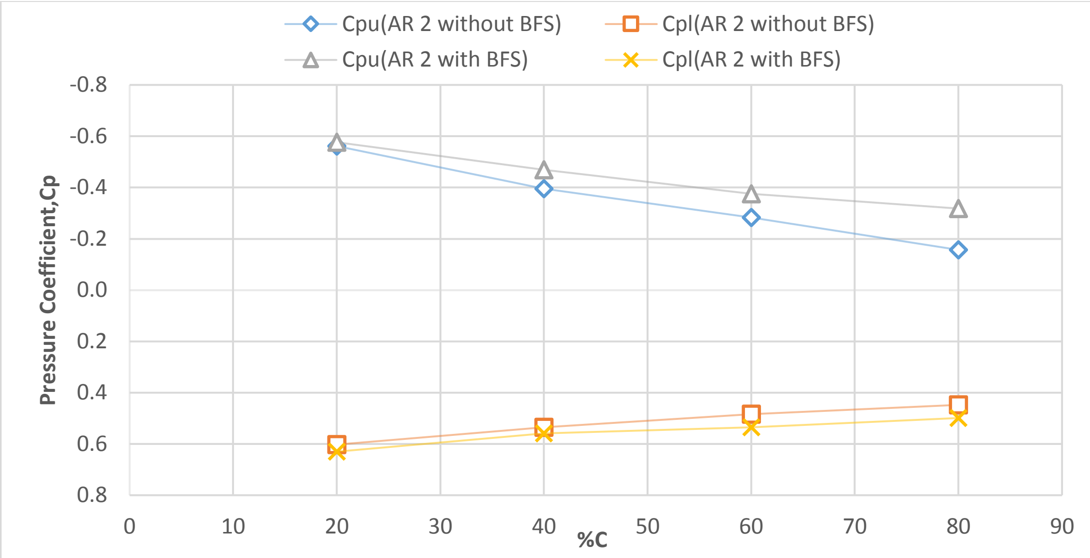

Figure 6.91: Cp distribution of segment C at 20^0 AOA

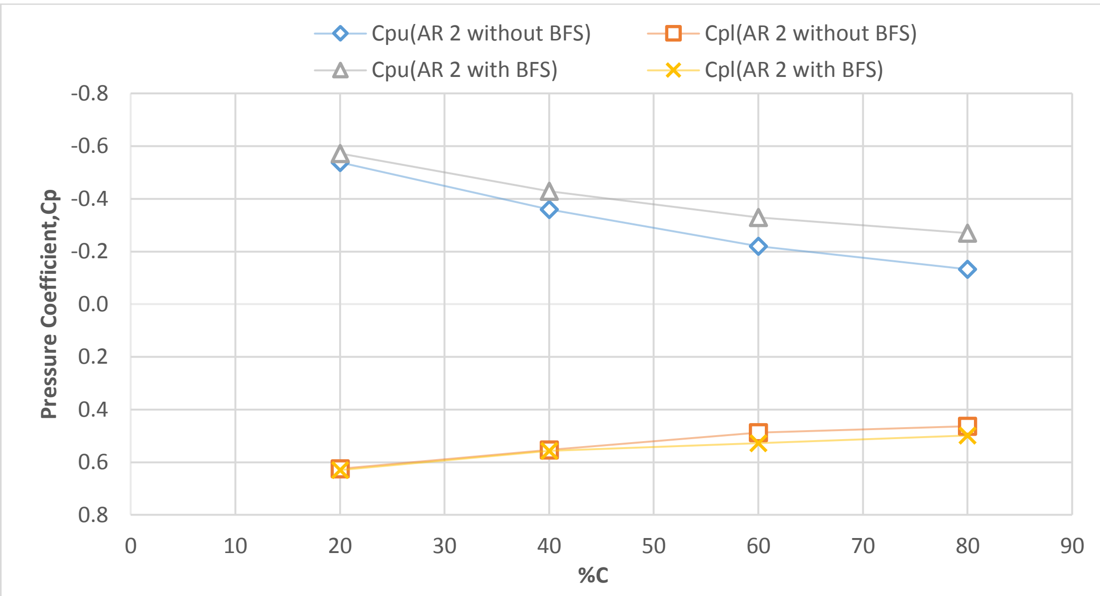

Figure 6.92: Cp distribution of segment D at 20^0 AOA

In comparison to the pressure difference of the upper and lower surfaces is higher for the optimum wing model with BFS than the optimum wing model without BFS. Another observation from the figures is that the lower surface pressure of all the wing models for all the segments are higher than all the previous angle of attack. From figures 6.85, 6.86, 6.87 and 6.88 it is seen that the highest-pressure difference between the upper and lower surfaces is obtained for optimum wing model with BFS. For all the segments the lower surface pressure decreases from 20%C to 80%C and upper surface pressure increases from leading edge to trailing edge.

6.8 Lift Characteristics of optimum wing model with BFS

The lift characteristics of optimum wing model with and without BFS at different angles are shown in figure 6.93. The lift increases with increase in angle of attack to a maximum value. After this maximum value of angle of attack, lift decreases drastically due to flow separation over the airfoil surface. From the figure, it is seen that the lift coefficient curve goes up from 0˚ angle of attack up to 12˚ angle of attack for the optimum wing model without BFS and then drops suddenly after 12˚ angle of attack. Thus, the critical angle of attack of the optimum wing model without BFS is around 12˚ beyond which the stall happens. But for the optimum wing model with BFS lift coefficient curve goes up from 0˚ angle of attack up to 14˚ angle then drops sharply after 14˚ angle of attack. So, the critical angle of attack of the optimum wing model with BFS is around 14˚ beyond which the stall happens. This condition is called stalling condition and the corresponding angle of attack is called stalling angle. The stalling angle happens to be approximately 12˚ angle of attack for wing model without BFS and14˚ with BFS. From figure 6.89, it is seen that the magnitude of the lift coefficient of the optimum wing model with BFS is higher than the optimum wing model without BFS.

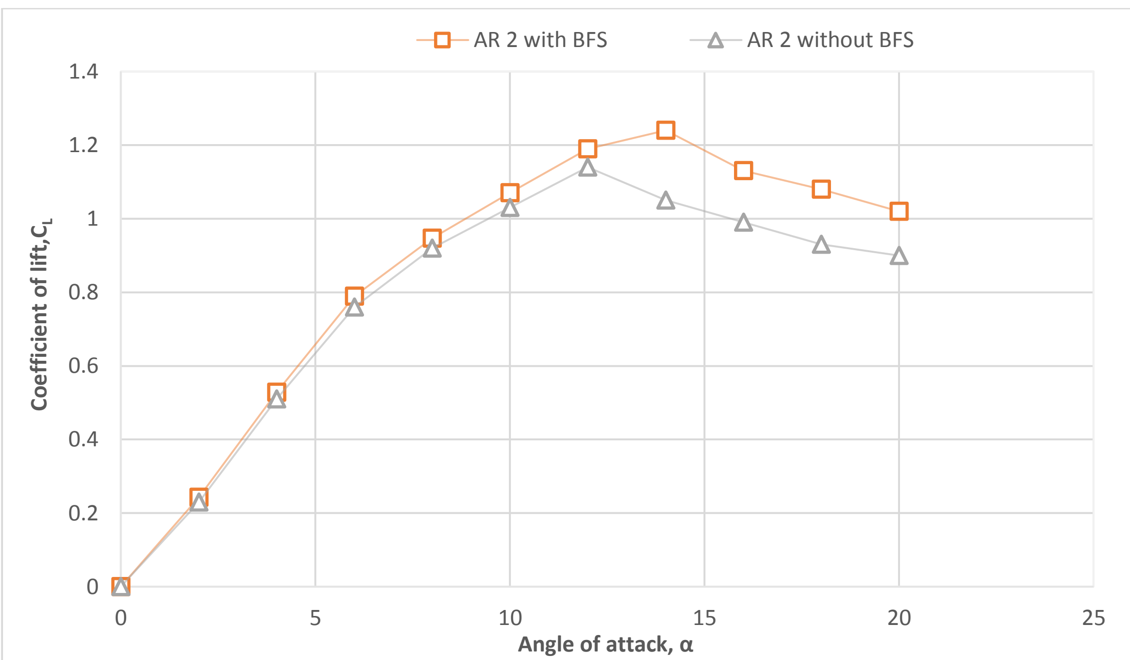

Figure 6.93: Coefficient of lift vs angle of attack for wing of AR 2(with and without BFS)

6.9 Drag Characteristics of optimum wing model with BFS

Figure 6.94 illustrates the drag coefficients of the wing models under test for the optimum wing model with and without BFS at different angle of attack (AOA). It is seen from the graph that the magnitude of drag coefficient for the optimum wing model with BFS are lower than the optimum wing model without BFS. This value is much lower at high angle of attack. The drag increases with a slower rate initially from 0˚ to 8˚ angle of attack. But from 8˚ to 20˚ angle of attack significant rise in drag is observed. It is observed from the graph that the drag coefficient starts to increase sharply after stalling angle of attack at 12˚ for the optimum wing without BFS and 14˚ for the optimum wing with BFS. This sudden increase in drag coefficient occurs because the air detaches from the surface of the airfoil due to strong adverse pressure gradient after stalling angle of attack. This sudden increase of drag coefficient indicates that if the angle of attack is increased any further the drag will dominate the lift and stall will occur. As the stalling angle of attack increases for the optimum wing model with BFS by 2˚, so by introducing BFS flow separation is controlled at higher angle of attack.

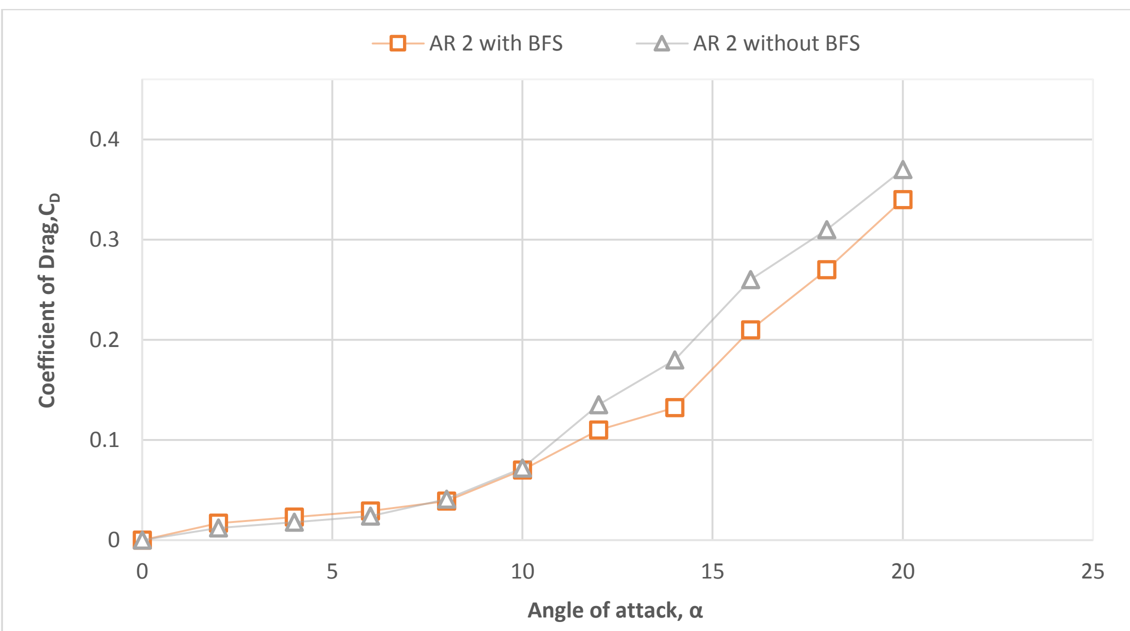

Figure 6.94: Coefficient of drag vs angle of attack for wing of AR 2(with and without BFS)

7

Chapter Seven

CONCLUSIONS AND RECOMMENDATIONS

7.1 Conclusions

Present experimental study investigates the optimum wing model from the analysis of the wing models with different aspect ratios having same wing area. After finding the optimum wing model, passive flow separation is controlled introducing backward facing step. The present investigation is carried out in the wind tunnel to make a comparative study among three different aspect ratios (AR 2, AR 1 and AR 0.5) of NACA 0012 wing. After analyzing the results, the optimum configuration is found out. At the end, the aerodynamic characteristics of airfoils with passive flow separation control is analyzed. All the data's are analyzed by plotting Coefficient of Pressure (C_P), Coefficient of lift (C_L), Coefficient of Drag (C_D), Coefficient of Lift to Drag Ratio (C_L/C_D) and Coefficient of Performance ($C_L^{1.5}/C_D$) versus angle of attack. The overall outcome of the present work can be summarized as follows:

i. It is observed that, the difference between upper and lower surface pressure on wing models of AR 2 is comparatively higher than that of other wing models at various angles of attack. This phenomenon happens because for same wing area it reduces the strength of the vortices at the wingtip by reducing the tip vortex more effectively than any other wing models.

ii. From the analysis of variation of lift coefficient with angle of attack, it is observed that the critical angle of attack for wing models of different aspect ratios remains around 12° but for the optimum wing model with backward facing step the critical angle of attack is 14°. So, stalling occurs after 12° angle of attack for all wing models except the wing models with backward facing step.

iii. The wing model of AR 2 provides the best lift characteristics among the three wing models without backward facing step. But the wing model of AR 2 with backward facing step provides higher lift at large angle of attack than the wing model of AR 2 without backward facing step.

iv. It is found that the drag is lowest for the wing model of AR 2 among the three experimental wing models. The wing model of AR 2 with backward facing step exhibits lower drag than wing model without backward facing step.

v. From the lift to drag coefficient ratio versus angle of attack curve, it is evident that the wing model of AR 2 exhibits higher lift to drag coefficient ratio than three other wing models. Also the wing with backward facing step provides larger lift to drag coefficient ratio than wing without having backward facing step.

vi. From the coefficient of performance ($C_L^{1.5}/C_D$) versus angle of attack curve, it is evident that for the wing model of AR 2 coefficient of performance is higher than three other wing models. Also the wing with backward facing step exhibits larger coefficient of performance than wing without having backward facing step.

vii. Thus, the present experimental investigation yielded the conclusion that wing models of AR 2 attains the maximum lift to drag coefficient ratio as well as the maximum coefficient of performance. So, according to these parameters the wing model of AR 2 is found to be the optimum.

viii. The results show that the passive flow separation on the optimum airfoil is controlled by delaying stalling angle of attack from 12^0 to 14^0. Introducing backward facing step on the optimum airfoil increases the lift coefficient, lift to drag coefficient ratio and coefficient of performance.

7.2 Recommendations for Future Works

The following recommendations can be made for future work in this field:

a. The coefficient of moment of the different wing models may be determined and compared with each other to analyze the aerodynamic stability characteristics of the wing models.

b. Different types of airfoils other than NACA 0012 may be used to analyze the effect of aspect ratios on the aerodynamic characteristics experimentally and then compare the experimental results with the results of simulations.

c. Different passive flow separation techniques can be applied on the optimum airfoil and compare each other to find the effective techniques of flow separation control through experiment.

d. The effect of surface roughness of the wing models on aerodynamic characteristics are required to investigate. Same wing models as present study but with different materials having low friction coefficient such as fiberglass or silver may be manufactured and examined inside wind tunnel. The results may then be compared with the present study to find the efficient materials for conducting experiments.

e. The research may be conducted at higher wind tunnel speed to analyze the variation of aerodynamic characteristics of different wing models at various air speed or Mach number.

f. Position and nature of the leading and trailing edge curve may be changed by varying the ratio of root chord to tip chord and then experimental results can be analyzed to find the aerodynamic characteristics.

g. The wing models can be incorporated with flaps at any suitable location at the leading or trailing edge to analyze and compare the different aerodynamic performances

8

REFERENCES

[1] Makwana P., B., Makadiya J., J., 'Numerical simulation of flow over airfoil and different techniques to reduce flow separation along with basic CFD model: A review study', International Journal of Engineering Research and Technology (IJERT), Vol:03, Issue:04, pp.399-404,2014.

[2] Jagannath Rajasekaran, 'On the flow characteristics behind a backward-facing step and the design of a new axisymmetric model for their study', MASc thesis, University of Toronto, 2011.

[3] Kianoosh Yousefi, S. Reza Saleh, Peyman Zahedi, 'Numerical study of flow separation control by tangential and perpendicular blowing on the NACA 0012 airfoil', International Journal of Engineering (IJE), Vol:07, Issue:01, pp.10-24,2013.

[4] Shawn Aram and Rajat Mittal, 'Computational Study of the Effect of Slot Orientation on Synthetic Jet-Based Separation Control', International Journal of Flow Control, Vol:03, No:02, pp.1-24,2012.

[5] Gad-El-Hak M., 'Flow Control: Passive, Active and Reactive Flow Management', The Aeronautical Journal, Vol:105, Issue:1045, pp.150,2000.

[6] Xingyu, Ma., 'Experimental Investigation of Coherent Structures Generated by Active and Passive Separation Control in Turbulent

Backward-Facing Step Flow', PhD Thesis, Georg-August University School of Science (GAUSS), Göttingen,2015.

[7] Shan, H., Jiang, L., Liu, C., 'Direct numerical simulation of flow separation around a NACA 0012 Airfoil', Comput Fluids 34(9):1096–1114, 2005.

[8] Hoarau, Y., Faghani, D., Braza, M., Perrin, R., Anne-Archard, D., Ruiz D., 'Direct numerical simulation of the three-dimensional transition to turbulence in the incompressible flow around a wing', Flow Turbul Combust 71(1–4):119–132,2003.

[9] Uranga, A., Persson, P., Drela, M., Peraire, J., 'Implicit large eddy simulation of transitional flows over airfoils and wings', In: 19th AIAA computational fluid dynamics, AIAA 2009-4131, San Antonio, Texas, 2009.

[10] Martinat, G., Braza, M., Hoarau,Y., Harran, G., 'Turbulence modeling of the flow past a pitching NACA 0012 Airfoil at 10^5 and 10^6 Reynolds numbers', J Fluids Struct, 24(8):1294–1303,2008.

[11] Bourdet, S., Bouhadji, A., Braza, M., Thiele, F., 'Direct numerical simulation of the three-dimensional transition to turbulence in the transonic flow around a wing', Flow Turbul Combust 71(1–4):203–220,2003.

[12] IM, HS., Zha, GC., 'Delayed detached eddy simulation of a stall flow over NACA0012 airfoil using high order schemes', In: 49th AIAA aerospace sciences meeting including the new horizons forum and aerospace exposition, AIAA 2011-1297, Orlando, Florida,2011.

[13] Yousefi, K., Saleh, R., Zahedi, P., ‘Numerical study of blowing and suction slot geometry optimization on NACA 0012 Airfoil’, Mech Sci Technol 28(4):1297–1310,2014.

[14] Yousefi, K., Saleh, R., ‘The effects of trailing edge blowing on aerodynamic characteristics of the NACA 0012 airfoil and optimization of the blowing slot geometry’, Journal of Theoretical and Applied Mechanics, 52, pp.165-179,2014.

[15] Troshin, V., Seifert, A., ‘Performance recovery of a thick turbulent airfoil using a distributed closed-loop flow control system’, Exp. Fluids 54(1), Article 1443,2013.

[16] Chapin, V.G., Benard E.,‘Active control of a stalled airfoil through steady or unsteady actuation jets’, J. Fluids Eng. 137 (9), 091103,2015.

[17] Shehata, A., S., Xiao, Q., Saqr, K., M., Naguib, A., Day, A., ‘Passive flow control for aerodynamic performance enhancement of airfoil with its application in Wells turbine–under oscillating flow condition’, Ocean Engineering ,136, pp.31-53,2017.

[18] Huang, L., Huang, PG., Le., Beau, RP., ‘Numerical study of blowing and suction control mechanism on NACA 0012 Airfoil’, Journal of Aircraft, vol: 41(5):1005–1013,2014.

[19] Ismat Ara, ‘An Experimental study on the aerodynamic performance of winglets with curved edge wing of NACA 4412’, M.Sc. Thesis, Bangladesh University of Engineering & Technology (BUET), Dhaka,2018.

[20] Kopac, M., Yilmaz, M., Gultop, T., ‘An Investigation of the Effect of Aspect Ratio on the Airfoil Performance’, American Journal of Applied Sciences 2(2):545-549,2005.

[21] Rosas, C.R., ‘Numerical Simulation of Flow Separation Control by Oscillator Fluid Injection’, A&M University, Texas,2005.

[22] Akcayoz, E., Tuncer, I.H., ‘Numerical Investigation of Flow Control over an Airfoil Using Synthetic Jets and its Optimization’, International Aerospace Conference, Turkey,2009.

[23] Kim, S.H., Kim, C., ‘Separation control on NACA23012 using synthetic jet’, Aerosp.Sci. Technol. 13 (4), 172–182,2009.

[24] Rumsey, C.L., Nishino, T., ‘Numerical study comparing RANS and LES approaches on a circulation control airfoil’, Int. J. Heat Fluid Flow 32 (5), 847–864,2011.

[25] Genc, M.S., Keynak, U., Yapici, H., ‘Performance of transition model for predicting low reynolds aerofoil flows without/with single and simultaneous blowing and suction’, Eur.J. Mech. B/Fluids 30 (2), 218–235,2011.

[26] Yagiz, B., Kandil, O., Pehlivanoglu, Y.V., ‘Drag minimization using active and passiveflow control techniques’,Aerosp. Sci. Technol. 17 (1), 21–31,2012.

[27] Hua Shan, Li Jiang, Chaoqun Liu, ‘Numerical Study of Passive and Active Flow Separation Control over a NACA0012 Airfoil’, Technical Report 2007-03, University of Texas at Arlington,2007.

[28] Patel, Karna S., ‘CFD Analysis of an Aerofoil’, International Journal of Engineering Research 3.3 :154-158,2014.

[29] Kevadiya, Mayurkumar, ‘CFD Analysis of Pressure Coefficient for NACA 4412’, International Journal of Engineering Trends and Technology, Chennai 4.5: 2041-2043,2013.

[30] Novel Kumar Sahu, Mr. Shadab Imam, ‘Analysis of Transonic Flow over an Airfoil NACA0012 using CFD’, International Journal of Innovative Science, Engineering & Technology, Vol. 2 Issue 4, pp.80-86,2015.

[31] Mainuddin, M., and Ali, M.A.T., ‘Experimental Investigation of Lift to Drag Ratio between Volumetric Equivalent Fuselages’, Proceedings of the 4th BSME-ASME International Conference on Thermal Engineering, Dhaka, Bangladesh, pp. 383-390,2008.

[32] Anderson, J.D., ‘Fundamentals of Aerodynamics’, McGraw-Hill Series in Aeronautical and Aerospace Engineering, 3rd Edition, pp. 15-22,2010.

[33] Nazmul M. and Ali M., ‘An Experimental Investigation on the Aerodynamic Characteristics of NACA 4412 Aerofoil with Curved-Edge Planform’, M.Sc. Thesis, Mechanical Engineering, BUET, Dhaka-1000, Bangladesh,2015.

[34] Kermode, A., C., ‘Flight without Formula’, Pitman,8th edition,1970.

[35] Eppler, R., ‘Airfoil Design and Data’, Springer-Verlag, Berlin,1990.

[36] Abbott, I. H. Von Doenhoff, A.E.V., and Stivers, L. S., ‘Summary of Aerofoil Data’, NACA Report No. 824,1945.

[37] National Aerofoil Data NACA 0012, Onine data, http://airfoiltools.com/airfoil/details?airfoil=naca 0012-il

[38] Pinkerton, R. M., 'The variation with Reynolds Number of pressure distribution over an airfoil section', National Advisory Committee for Aeronautics, Report No. 613, pp. 65-84.

[39] Agarwal, S. and Kumar, P., 'Investigation of Flow Field over NACA4412 with a Vortex Generator', Journal of Advanced Research in Applied Mechanics & Computational Fluid Dynamics, Vol. 01, pp. 1-12,2014

[40] Clancy, L., J., 'Aerodynamics', John Wiley, New York,1975.

[41] White, F., M., 'Fluid Mechanics', McGraw-Hill series in Mechanical Engineering, 4th Edition, pp.524-527,1999.

[42] Anderson, J.D., 'Introduction to Flight', McGraw-Hill Series in Aeronautical and Aerospace Engineering, 6th Edition, pp. 326-328,2010.

[43] Cimbala, J.M., 'Experimental Uncertainty Analysis', Online Edition, pp.1-4,2013.

[44] Alam, G. M. J., 'Interference Effect and Flow Pattern of Four Biplane Configurations using NACA 0024 Profile', Proceedings of The International Conference on Mechanical Engineering, Dhaka Bangladesh,2011.

[45] Ramesh, P., 'Numerical and Experimental investigation of the effect of geometry modification on the Aerodynamic characteristics of a NACA 64 (2)-415 wing', M.Sc. Thesis, Royal Institute of Technology, Stockholm, Sweden,2013.

[46] Abbott, I., H., Doenhoff, A., E., V., 'Theory of Wing Sections including a Summary of Aerofoil Data', Dover Publications, New York,1990.

[47] Devenport, W., J., Schetz, J., A., 'The Investigation of an Inboard-Winglet Application to a Roadable Aircraft', M.Sc. In Aerospace Engineering Thesis, Virginia polytechnic Institute and State University, pp. 24-26,2002.

[48] Laurence, K., L., Jr., Poteat, M., I., 'Aerodynamic Characteristics of several NACA airfoil sections at seven Reynolds number from 0.7×10^6 to 9×10^6', Langley Memorial Aeronautical Laboratory,1948.

APPENDIX-I

Table 1: Calculated Values of Pressure Coefficient at 0° Angle of Attack

Segment	%C	Wing model of AR 0.5		Wing model of AR 1		Wing model of AR 2	
		Cpu	Cpl	Cpu	Cpl	Cpu	Cpl
Segment-A	20	-0.323403609	-0.323403609	-0.335328395	-0.335328395	-0.353215575	-0.353215575
	40	-0.311478822	-0.311478822	-0.323403609	-0.323403609	-0.329366002	-0.329366002
	60	-0.239930104	-0.239930104	-0.251854891	-0.251854891	-0.245892498	-0.245892498
	80	-0.06105831	-0.06105831	-0.072983096	-0.072983096	-0.067020703	-0.067020703
Segment-B	20	-0.317441216	-0.317441216	-0.329366002	-0.329366002	-0.347253181	-0.347253181
	40	-0.323403609	-0.323403609	-0.331750959	-0.331750959	-0.323403609	-0.323403609
	60	-0.228005318	-0.228005318	-0.245892498	-0.245892498	-0.23516019	-0.23516019
	80	-0.072983096	-0.072983096	-0.078945489	-0.078945489	-0.06940566	-0.06940566
Segment-C	20	-0.228983481	-0.228983481	-0.21478457	-0.21478457	-0.228374936	-0.228374931
	40	-0.19321278	-0.19321278	-0.189835769	-0.189835769	-0.202037483	-0.202037483
	60	-0.151671962	-0.151671962	-0.148914253	-0.148914253	-0.157826592	-0.157826592
	80	-0.076204941	-0.076204941	-0.032839484	-0.032839484	-0.048998312	-0.048998312
Segment-D	20	-0.303131472	-0.303131472	-0.325788566	-0.325788566	-0.343675745	-0.343675745
	40	-0.297169079	-0.297169079	-0.300746515	-0.300746515	-0.316248737	-0.316248737
	60	-0.224427882	-0.224427882	-0.237545147	-0.237545147	-0.253047369	-0.253047369
	80	-0.067020703	-0.067020703	-0.059865831	-0.059865831	-0.073903438	-0.073903438

`

Table 2: Calculated Values of Pressure Coefficient at 2° Angle of Attack							
Segment	**%C**	**Wing model of AR 0.5**		**Wing model of AR 1**		**Wing model of AR 2**	
		Cpu	**Cpl**	**Cpu**	**Cpl**	**Cpu**	**Cpl**
Segment-A	20	-0.5483514110	0.0512340	-0.5832140	0.06231740	-0.61782310	0.04879231
	40	-0.4471389040	0.0416724	-0.4757832	0.04346781	-0.48893210	0.06567213
	60	-0.3100600000	0.0232123	-0.34137821	0.02397841	-0.37347682	0.03456819
	80	-0.1117847260	0.0111270	-0.14127810	0.02784351	-0.15782561	0.01754282
Segment-B	20	-0.5493510230	0.0491125	-0.5897732	0.05957934	-0.62546500	0.04179231
	40	-0.4400381040	0.0391675	-0.4527657	0.04246322	-0.47968930	0.06267654
	60	-0.2723879600	0.0196873	-0.30931210	0.02799780	-0.33378921	0.03850202
	80	-0.1217921020	0.0099341	-0.14167110	0.02678921	-0.15556910	0.01912671
Segment-C	20	-0.5523415670	0.05026713	-0.59362871	0.06378218	-0.63839265	0.05672912
	40	-0.4627189020	0.0485214	-0.48345219	0.04763218	-0.49735421	0.05119200
	60	-0.2762451910	0.0267310	-0.33658719	0.03562781	-0.36426398	0.02637190
	80	-0.1376290340	0.0178290	-0.15893213	0.04536728	-0.16682923	0.02117830
Segment-D	20	-0.5173785620	0.0578125	-0.5679778	0.06875763	-0.61385363	0.08733534
	40	-0.4019489234	0.0376193	-0.4461323	0.04891431	-0.46832130	0.05938672
	60	-0.2631978110	0.0127739	-0.30935420	0.02989742	-0.34376718	0.03971957
	80	-0.1189756410	0.0098418	-0.14934516	0.01977417	-0.15857823	0.01234616

Table 3: Calculated Values of Pressure Coefficient at 4° Angle of Attack

Segment	%C	Wing model of AR 0.5		Wing model of AR 1		Wing model of AR 2	
		Cpu	Cpl	Cpu	Cpl	Cpu	Cpl
Segment-A	20	-0.6643234562	0.0895125	-0.6954721	0.09917576	-0.72378387	0.12787334
	40	-0.4819489752	0.0787619	-0.5161323	0.04891431	-0.53832130	0.08720193
	60	-0.3398238110	0.0482573	-0.35935420	0.02452970	-0.38376718	0.04935621
	80	-0.2189756410	0.0384672	-0.19934516	0.01998342	-0.25857823	0.02034234
Segment-B	20	-0.6783976200	0.0929515	-0.6992891	0.08191752	-0.73398230	0.13562130
	40	-0.4786234210	0.0623870	-0.4993061	0.05132671	-0.55721200	0.07242230
	60	-0.3168730900	0.0382542	-0.33993217	0.01294100	-0.37820720	0.03785310
	80	-0.1985372900	0.0314357	-0.21996531	0.00993811	-0.25875312	0.03178230
Segment-C	20	-0.6817823100	0.0887531	-0.7082671	0.08112367	-0.74934210	0.12934210
	40	-0.4587451200	0.0578215	-0.5219093	0.06782310	-0.56278310	0.08782413
	60	-0.3394376100	0.0411242	-0.35993420	0.01899361	-0.38952100	0.05785310
	80	-0.2265892130	0.0298144	-0.23775250	0.01157840	-0.27238700	0.04967192
Segment-D	20	-0.6738923902	0.0789342	-0.69945729	0.07345262	-0.73458721	0.11893552
	40	-0.4456728190	0.0672393	-0.53679812	0.05789213	-0.55783921	0.07832561
	60	-0.3162581900	0.0377652	-0.3342519	0.03627816	-0.37629182	0.04672992
	80	-0.2017664840	0.0235894	-0.2156389	0.02537789	-0.26453810	0.03478910

Table 4: Calculated Values of Pressure Coefficient at 6° Angle of Attack							
Segment	**%C**	**Wing model of AR 0.5**		**Wing model of AR 1**		**Wing model of AR 2**	
		Cpu	**Cpl**	**Cpu**	**Cpl**	**Cpu**	**Cpl**
Segment-A	20	-0.6923571300	0.0911845	-0.72999323	0.11397210	-0.80102999	0.13826871
	40	-0.5289120370	0.0511942	-0.56592700	0.06729282	-0.62319123	0.07982625
	60	-0.3728015800	0.0298111	-0.41322514	0.03261411	-0.44598395	0.03937987
	80	-0.2589298760	0.0211020	-0.29238700	0.01018350	-0.33238700	0.03193220
Segment-B	20	-0.6998732100	0.0993418	-0.73123761	0.12343970	-0.81245102	0.14823422
	40	-0.5312864300	0.0678291	-0.56126359	0.07729282	-0.61261892	0.05291982
	60	-0.3687213500	0.0321937	-0.40894210	0.04266571	-0.43892593	0.04829379
	80	-0.2534671986	0.0318391	-0.28278309	0.03048200	-0.33983410	0.04157190
Segment-C	20	-0.7112356920	0.0989934	-0.73892121	0.11983234	-0.82891245	0.15012738
	40	-0.5389128000	0.0411238	-0.56892110	0.08012729	-0.60782150	0.09031622
	60	-0.3701020370	0.0231892	-0.41254167	0.04992127	-0.44671092	0.05802829
	80	-0.2479203467	0.0299183	-0.27820122	0.04892010	-0.32398498	0.05115728
Segment-D	20	-0.7011236	0.0899899	-0.72678911	0.10152893	-0.81780989	0.14903012
	40	-0.5278189	0.0597211	-0.57213912	0.09032043	-0.62974097	0.10270310
	60	-0.3623411	0.0376512	-0.42354198	0.04672309	-0.45596236	0.06802829
	80	-0.2893452	0.0312564	-0.31877220	0.04018294	-0.34339850	0.05783215

Table 5: Calculated Values of Pressure Coefficient at 8° Angle of Attack							
Segment	**%C**	**Wing model of AR 0.5**		**Wing model of AR 1**		**Wing model of AR 2**	
		Cpu	**Cpl**	**Cpu**	**Cpl**	**Cpu**	**Cpl**
Segment-A	20	-0.8313661	0.1099271	-0.90382326	0.10271827	-1.01303620	0.15098290
	40	-0.6163283	0.0912567	-0.68822671	0.08926322	-0.74645267	0.13182218
	60	-0.4337189	0.0674673	-0.47821893	0.04782723	-0.53125618	0.07398724
	80	-0.2839228	0.0492109	-0.34792639	0.03899283	-0.38924163	0.06709221
Segment-B	20	-0.8411236	0.1012764	-0.91326453	0.11271524	-1.04378090	0.16294120
	40	-0.6237289	0.0934530	-0.69827213	0.09632316	-0.75649741	0.13218270
	60	-0.4482220	0.0575761	-0.48893544	0.03672345	-0.54125962	0.08398028
	80	-0.2928439	0.0408931	-0.35638772	0.03928301	-0.39643398	0.07092783
Segment-C	20	-0.8567112	0.1126784	-0.97832438	0.13809457	-1.09562929	0.17920023
	40	-0.6311563	0.0998231	-0.72909373	0.11820946	-0.78649741	0.14782218
	60	-0.4567290	0.0628190	-0.50278345	0.08902672	-0.57912596	0.09439802
	80	-0.3012674	0.0508679	-0.36820631	0.07893200	-0.40264340	0.07562912
Segment-D	20	-0.8498256	0.1283649	-0.99878324	0.14192388	-1.07823450	0.16952398
	40	-0.6412738	0.1020374	-0.70128245	0.12783905	-0.77829164	0.13465892
	60	-0.4673092	0.0773971	-0.51201450	0.07452710	-0.56721912	0.09007243
	80	-0.3328177	0.0672109	-0.35987831	0.06392893	-0.41264345	0.09567291

Table 6: Calculated Values of Pressure Coefficient at 10° Angle of Attack							
Segment	**%C**	**Wing model of AR 0.5**		**Wing model of AR 1**		**Wing model of AR 2**	
		Cpu	**Cpl**	**Cpu**	**Cpl**	**Cpu**	**Cpl**
Segment-A	20	-0.9872983	0.1486782	-1.17829300	0.16730192	-1.25232457	0.21997655
	40	-0.7452611	0.1173892	-0.83452890	0.14759783	-0.89356210	0.16732454
	60	-0.5523159	0.0745278	-0.65234190	0.11892341	-0.70153427	0.11670075
	80	-0.3782013	0.0683902	-0.46459823	0.08968233	-0.54271930	0.10456281
Segment-B	20	-0.9972568	0.1498329	-1.19245820	0.16927301	-1.26793652	0.22679343
	40	-0.7572895	0.1234168	-0.85423451	0.14783759	-0.92143536	0.17387325
	60	-0.5683158	0.0678923	-0.65823765	0.12893781	-0.74153427	0.14889967
	80	-0.4538538	0.0567892	-0.53894592	0.09823197	-0.59727193	0.11455600
Segment-C	20	-0.9845255	0.1456789	-1.17013422	0.18657321	-1.22456310	0.24211679
	40	-0.7536271	0.1206527	-0.85467742	0.16789067	-0.92445679	0.19218561
	60	-0.5502368	0.0801278	-0.64782516	0.12986436	-0.74569615	0.14527810
	80	-0.4434216	0.0556782	-0.52567562	0.10045654	-0.61893456	0.12893451
Segment-D	20	-1.0845255	0.1589833	-1.20167322	0.17192543	-1.28963210	0.23679343
	40	-0.7897290	0.1301234	-0.86742335	0.15679781	-0.93471435	0.18783810
	60	-0.6023683	0.0701278	-0.66782821	0.13468931	-0.75615342	0.13834210
	80	-0.4892382	0.0673824	-0.54567822	0.10236823	-0.60345727	0.12434510

Table 7: Calculated Values of Pressure Coefficient at 12° Angle of Attack							
Segment	**%C**	**Wing model of AR 0.5**		**Wing model of AR 1**		**Wing model of AR 2**	
		Cpu	**Cpl**	**Cpu**	**Cpl**	**Cpu**	**Cpl**
Segment-A	20	-1.1845678	0.1812898	-1.28167822	0.21189452	-1.36796781	0.27386790
	40	-0.8897457	0.1456873	-0.96774233	0.18729679	-1.07147143	0.21783780
	60	-0.6873571	0.0934789	-0.77827821	0.14624312	-0.86153421	0.16789281
	80	-0.5112780	0.0678921	-0.58956785	0.09343879	-0.65823410	0.11782813
Segment-B	20	-1.2074568	0.1991728	-1.31216200	0.24173452	-1.38764900	0.29873215
	40	-0.9049745	0.1789257	-1.00687742	0.14782730	-1.12365910	0.22687832
	60	-0.7197357	0.1033478	-0.79123828	0.12362472	-0.89157652	0.18978234
	80	-0.5131898	0.0568274	-0.56529569	0.06934388	-0.69852131	0.09727822
Segment-C	20	-1.2276718	0.2078991	-1.34567912	0.24173452	-1.39682341	0.30912874
	40	-0.9238915	0.1698269	-1.03873271	0.21782730	-1.13452992	0.26539168
	60	-0.7389297	0.1287134	-0.82123672	0.14523625	-0.93678219	0.19823518
	80	-0.5377931	0.0789682	-0.61963530	0.06934388	-0.72985213	0.11927727
Segment-D	20	-1.2034761	0.1987378	-1.33217892	0.23216791	-1.36672991	0.28311281
	40	-0.9193891	0.1782916	-1.01267810	0.20279729	-1.11845212	0.24563934
	60	-0.7167222	0.1399871	-0.80672810	0.17852364	-0.90136782	0.16798231
	80	-0.5268071	0.0686825	-0.58923193	0.05934380	-0.69278522	0.09126723

Table 8: Calculated Values of Pressure Coefficient at 14° Angle of Attack							
Segment	**%C**	**Wing model of AR 0.5**		**Wing model of AR 1**		**Wing model of AR 2**	
		Cpu	**Cpl**	**Cpu**	**Cpl**	**Cpu**	**Cpl**
Segment-A	20	-1.1327567	0.2238930	-1.26456702	0.35493451	-1.39682341	0.48126732
	40	-0.8024891	0.1834902	-0.98723567	0.26735672	-1.11452992	0.33539168
	60	-0.4978933	0.1356710	-0.59281902	0.18952672	-0.70836782	0.25182352
	80	-0.2993774	0.0989687	-0.37899635	0.16589432	-0.42398524	0.19927727
Segment-B	20	-1.1472757	0.2338930	-1.27456702	0.36579046	-1.40268234	0.49451267
	40	-0.8224891	0.1834902	-0.98976422	0.27835635	-1.15457321	0.35629054
	60	-0.5097893	0.1656710	-0.58978281	0.19953452	-0.76573837	0.26732918
	80	-0.2879377	0.1089687	-0.39823462	0.17835845	-0.46398638	0.21783424
Segment-C	20	-1.1478527	0.2365433	-1.28291023	0.37231893	-1.41236780	0.51562376
	40	-0.8334563	0.1899012	-0.99823618	0.29532132	-1.16732929	0.36739158
	60	-0.5078349	0.1672917	-0.64328192	0.21354671	-0.77802613	0.27780923
	80	-0.2998167	0.1219830	-0.40025431	0.18931562	-0.49539203	0.23993675
Segment-D	20	-1.1378290	0.2427819	-1.23452790	0.32341763	-1.38872670	0.48990234
	40	-0.8034923	0.1733563	-0.94352923	0.28342580	-1.14253790	0.33345211
	60	-0.4897898	0.1645267	-0.61982134	0.20963789	-0.74538279	0.28734129
	80	-0.2578190	0.1172839	-0.33992531	0.15341891	-0.42441603	0.24528926

Table 9: Calculated Values of Pressure Coefficient at 16° Angle of Attack							
Segment	**%C**	**Wing model of AR 0.5**		**Wing model of AR 1**		**Wing model of AR 2**	
		Cpu	**Cpl**	**Cpu**	**Cpl**	**Cpu**	**Cpl**
Segment-A	20	-0.716921557	0.297437417	-0.788470275	0.383587844	-0.836169421	0.509476049
	40	-0.517297626	0.225888699	-0.569222412	0.293963913	-0.628846344	0.365512631
	60	-0.312607028	0.202039126	-0.368381387	0.27011434	-0.449280053	0.295888699
	80	-0.172983096	0.186264767	-0.206832669	0.218189554	-0.294907882	0.27011434
Segment-B	20	-0.728846344	0.29668528	-0.794432669	0.392083571	-0.848094207	0.509133143
	40	-0.526124976	0.237061349	-0.599974549	0.308610066	-0.64537284	0.392083571
	60	-0.359177968	0.207249383	-0.393403609	0.264760494	-0.478425831	0.308610066
	80	-0.180306173	0.195324596	-0.239930104	0.225136562	-0.311478822	0.284760494
Segment-C	20	-0.74077113	0.29668528	-0.788470275	0.404008357	-0.824244634	0.52325622
	40	-0.51420019	0.248986135	-0.573824122	0.332459639	-0.633448053	0.404008357
	60	-0.28302754	0.225136562	-0.347253181	0.278610066	-0.442651472	0.332459639
	80	-0.168381387	0.20128699	-0.224155745	0.237061349	-0.281666857	0.31457246
Segment-D	20	-0.752695916	0.282835708	-0.794432669	0.415933143	-0.836169421	0.517293827
	40	-0.508049763	0.22128699	-0.561899335	0.344384425	-0.621523267	0.392083571
	60	-0.306877113	0.205324596	-0.373403609	0.280053485	-0.430726686	0.332459639
	80	-0.192230959	0.177437417	-0.228005318	0.260910921	-0.26974207	0.326497246

Table 10: Calculated Values of Pressure Coefficient at 18° Angle of Attack							
Segment	**%C**	**Wing model of AR 0.5**		**Wing model of AR 1**		**Wing model of AR 2**	
		Cpu	**Cpl**	**Cpu**	**Cpl**	**Cpu**	**Cpl**
Segment-A	20	-0.526124976	0.346497246	-0.561899335	0.439782716	-0.631523267	0.525181007
	40	-0.378801899	0.294760494	-0.450350617	0.372083571	-0.511899335	0.451707502
	60	-0.235328395	0.255136562	-0.31302754	0.332459639	-0.388801899	0.404008357
	80	-0.108757455	0.233211776	-0.198381387	0.320534853	-0.315704463	0.370346819
Segment-B	20	-0.510420019	0.404008357	-0.578049763	0.463632289	-0.625748908	0.5411434
	40	-0.346877113	0.338610066	-0.438425831	0.415933143	-0.509974549	0.463632289
	60	-0.269366002	0.297061349	-0.331102754	0.356309212	-0.414952327	0.415933143
	80	-0.184531814	0.277249383	-0.236832669	0.338422032	-0.358005318	0.388233998
Segment-C	20	-0.508049763	0.40997075	-0.561899335	0.475557075	-0.639598481	0.559030579
	40	-0.380726686	0.332459639	-0.47420019	0.42785793	-0.525748908	0.487481861
	60	-0.311102754	0.288986135	-0.404952327	0.368233998	-0.480726686	0.439782716
	80	-0.280306173	0.243211776	-0.312607028	0.332459639	-0.415489079	0.380158784
Segment-D	20	-0.490420019	0.415933143	-0.549974549	0.499406648	-0.633448053	0.582880152
	40	-0.388801899	0.356309212	-0.456124976	0.431707502	-0.529598481	0.499406648
	60	-0.315328395	0.340534853	-0.388801899	0.406400836	-0.44420019	0.463632289
	80	-0.280682241	0.317061349	-0.3164566	0.356309212	-0.366292498	0.404008357

Table 11: Calculated Values of Pressure Coefficient at 20° Angle of Attack							
Segment	**%C**	**Wing model of AR 0.5**		**Wing model of AR 1**		**Wing model of AR 2**	
		Cpu	**Cpl**	**Cpu**	**Cpl**	**Cpu**	**Cpl**
Segment-A	20	-0.388989934	0.439782716	-0.452839506	0.511331434	-0.541899335	0.606729725
	40	-0.299554036	0.392083571	-0.394952327	0.487481861	-0.480804976	0.565622032
	60	-0.150415575	0.356309212	-0.239554036	0.42785793	-0.330726686	0.507481861
	80	-0.084907882	0.284760494	-0.132607028	0.348233998	-0.218381387	0.449782716
Segment-B	20	-0.406877113	0.445745109	-0.494764292	0.52325622	-0.573824122	0.618654511
	40	-0.319177968	0.404008357	-0.394952327	0.463632289	-0.468801899	0.529218613
	60	-0.1964566	0.362271605	-0.252230959	0.439782716	-0.338018993	0.499406648
	80	-0.096832669	0.29668528	-0.150682241	0.380158784	-0.244531814	0.451707502
Segment-C	20	-0.391102754	0.431707502	-0.436877113	0.535181007	-0.561899335	0.602692118
	40	-0.217253181	0.425933143	-0.307253181	0.451707502	-0.394952327	0.535181007
	60	-0.108757455	0.390158784	-0.184531814	0.433820323	-0.283403609	0.483632289
	80	-0.062983096	0.332459639	-0.114907882	0.392083571	-0.1564566	0.44785793
Segment-D	20	-0.359177968	0.463632289	-0.430726686	0.547105793	-0.538049763	0.624616904
	40	-0.217253181	0.415933143	-0.295140361	0.463632289	-0.359177968	0.553068186
	60	-0.084907882	0.368233998	-0.150682241	0.439782716	-0.220306173	0.487481861
	80	-0.039133523	0.344384425	-0.084907882	0.404008357	-0.132607028	0.463632289

Table 12: Calculated Values of Pressure Coefficient at 0° Angle of Attack With BFS			
Segment	%C	Optimum Wing model With BFS	
		Cpu	Cpl
Segment-A	20	-0.359177968	-0.359177968
	40	-0.323403609	-0.323403609
	60	-0.251854891	-0.245892498
	80	-0.108757455	-0.102795062
Segment-B	20	-0.341290788	-0.341290788
	40	-0.329366002	-0.329366002
	60	-0.239930104	-0.233967711
	80	-0.096832669	-0.088485318
Segment-C	20	-0.365140361	-0.365140361
	40	-0.330558481	-0.330558481
	60	-0.245892498	-0.239930104
	80	-0.093255233	-0.086100361
Segment-D	20	-0.343675745	-0.343675745
	40	-0.311478822	-0.311478822
	60	-0.255432327	-0.251854891
	80	-0.084907882	-0.081330446

Table 13: Calculated Values of Pressure Coefficient at 2° Angle of Attack With BFS			
Segment	%C	Optimum Wing model With BFS	
		Cpu	Cpl
Segment-A	20	-0.621523267	0.058189554
	40	-0.484388224	0.056264767
	60	-0.39302754	0.044339981
	80	-0.178381387	0.019452802
Segment-B	20	-0.625100703	0.062959468
	40	-0.482003267	0.040302374
	60	-0.37302754	0.034339981
	80	-0.172607028	0.035992631
Segment-C	20	-0.638217968	0.067729383
	40	-0.490350617	0.046264767
	60	-0.371102754	0.039109896
	80	-0.180306173	0.03553246
Segment-D	20	-0.623908224	0.07011434
	40	-0.466501045	0.060574511
	60	-0.36302754	0.03553246
	80	-0.191226515	0.034339981

Table 14: Calculated Values of Pressure Coefficient at 4° Angle of Attack With BFS			
Segment	**%C**	**Optimum Wing model With BFS**	
		Cpu	**Cpl**
Segment-A	20	-0.726461387	0.129738272
	40	-0.538049763	0.080846648
	60	-0.413759848	0.058189554
	80	-0.278549592	0.03553246
Segment-B	20	-0.739578651	0.141663058
	40	-0.560706857	0.082039126
	60	-0.39302754	0.06011434
	80	-0.276164634	0.046264767
Segment-C	20	-0.74077113	0.134508186
	40	-0.573824122	0.088001519
	60	-0.406877113	0.074884255
	80	-0.29762925	0.045072289
Segment-D	20	-0.739578651	0.117813485
	40	-0.569054207	0.090386477
	60	-0.394952327	0.064151947
	80	-0.299554036	0.033147502

Table 15: Calculated Values of Pressure Coefficient at 6° Angle of Attack With BFS			
Segment	**%C**	**Optimum Wing model With BFS**	
		Cpu	**Cpl**
Segment-A	20	-0.812319848	0.146432972
	40	-0.621523267	0.082039126
	60	-0.454576258	0.068921861
	80	-0.359177968	0.039109896
Segment-B	20	-0.814704805	0.143587844
	40	-0.62748566	0.073963913
	60	-0.466501045	0.071306819
	80	-0.355600532	0.058649725
Segment-C	20	-0.824244634	0.165512631
	40	-0.632255575	0.097541349
	60	-0.464116087	0.082039126
	80	-0.359177968	0.06176699
Segment-D	20	-0.821859677	0.153587844
	40	-0.629870617	0.084424084
	60	-0.466501045	0.07011434
	80	-0.360370446	0.066264767

Table 16: Calculated Values of Pressure Coefficient at 8° Angle of Attack With BFS

Segment	%C	Optimum Wing model With BFS	
		Cpu	Cpl
Segment-A	20	-1.018618651	0.169090066
	40	-0.737193694	0.141663058
	60	-0.549974549	0.093963913
	80	-0.411374891	0.087269212
Segment-B	20	-1.047238139	0.170282545
	40	-0.761043267	0.139278101
	60	-0.580246686	0.105888699
	80	-0.434031985	0.082039126
Segment-C	20	-1.089162925	0.166705109
	40	-0.804620703	0.141663058
	60	-0.605748908	0.109466135
	80	-0.442651472	0.093963913
Segment-D	20	-1.09851472	0.170282545
	40	-0.800395062	0.145240494
	60	-0.597673694	0.114236049
	80	-0.454576258	0.101118784

Table 17: Calculated Values of Pressure Coefficient at 10° Angle of Attack With BFS

Segment	%C	Optimum Wing model With BFS	
		Cpu	Cpl
Segment-A	20	-1.265461728	0.225136562
	40	-0.931567711	0.189362203
	60	-0.76077113	0.121390921
	80	-0.625748908	0.117813485
Segment-B	20	-1.289311301	0.229906477
	40	-0.943492498	0.196517075
	60	-0.788470275	0.153587844
	80	-0.621523267	0.129738272
Segment-C	20	-1.265733865	0.238253827
	40	-0.938722583	0.204864425
	60	-0.803700361	0.165512631
	80	-0.665560874	0.151663058
Segment-D	20	-1.280963951	0.24421622
	40	-0.976337626	0.213211776
	60	-0.791315404	0.177437417
	80	-0.653448053	0.155972802

Table 18: Calculated Values of Pressure Coefficient at 12° Angle of Attack With BFS

Segment	%C	Optimum Wing model With BFS	
		Cpu	Cpl
Segment-A	20	-1.372784805	0.284760494
	40	-1.09734207	0.225136562
	60	-0.927718139	0.189362203
	80	-0.788470275	0.165512631
Segment-B	20	-1.383517113	0.29668528
	40	-1.146213865	0.239446306
	60	-0.960103096	0.217709554
	80	-0.800395062	0.170282545
Segment-C	20	-1.396634378	0.308610066
	40	-1.158138651	0.248986135
	60	-0.973492498	0.20128699
	80	-0.812319848	0.177437417
Segment-D	20	-1.400211814	0.310995024
	40	-1.160523609	0.252563571
	60	-0.987069934	0.204864425
	80	-0.814704805	0.18339981

Table 19: Calculated Values of Pressure Coefficient at 14° Angle of Attack With BFS

Segment	%C	Optimum Wing model With BFS	
		Cpu	Cpl
Segment-A	20	-1.440483951	0.499406648
	40	-1.153536942	0.368233998
	60	-0.87194378	0.270910921
	80	-0.680395062	0.251286990
Segment-B	20	-1.422868908	0.504176562
	40	-1.161884292	0.371811434
	60	-0.873136258	0.324488357
	80	-0.696357455	0.256056904
Segment-C	20	-1.434793694	0.511331434
	40	-1.146213865	0.380158784
	60	-0.879098651	0.292835708
	80	-0.669222412	0.265136562
Segment-D	20	-1.435986173	0.513716391
	40	-1.162636429	0.384928699
	60	-0.875521216	0.287605622
	80	-0.660875062	0.277061349

Table 20: Calculated Values of Pressure Coefficient at 16° Angle of Attack With BFS			
Segment	**%C**	**Optimum Wing model With BFS**	
		Cpu	**Cpl**
Segment-A	20	-0.870563267	0.523256220
	40	-0.668470275	0.392083571
	60	-0.531523267	0.334760494
	80	-0.430726686	0.311183058
Segment-B	20	-0.875793352	0.528026135
	40	-0.707005661	0.394468528
	60	-0.570959848	0.332459639
	80	-0.470454549	0.320534853
Segment-C	20	-0.883868566	0.524448699
	40	-0.664620703	0.400430921
	60	-0.525748908	0.371267160
	80	-0.406877113	0.339342374
Segment-D	20	-0.882676087	0.522063742
	40	-0.669222412	0.390891092
	60	-0.529974549	0.372459639
	80	-0.399722241	0.343191947

Table 21: Calculated Values of Pressure Coefficient at 18° Angle of Attack With BFS			
Segment	**%C**	**Optimum Wing model With BFS**	
		Cpu	**Cpl**
Segment-A	20	-0.670077113	0.535181007
	40	-0.550537284	0.42785793
	60	-0.490350617	0.415933143
	80	-0.414952327	0.404008357
Segment-B	20	-0.657297626	0.541143401
	40	-0.538049763	0.431435366
	60	-0.483195745	0.421895537
	80	-0.418801899	0.412355708
Segment-C	20	-0.673260019	0.538758443
	40	-0.572819677	0.437397759
	60	-0.560810788	0.427857931
	80	-0.487609421	0.425933143
Segment-D	20	-0.681147198	0.597105793
	40	-0.561899335	0.519782716
	60	-0.512275404	0.496665451
	80	-0.470726686	0.427857932

Table 22: Calculated Values of Pressure Coefficient at 20° Angle of Attack With BFS			
Segment	%C	Optimum Wing model With BFS	
		Cpu	Cpl
Segment-A	20	-0.573824122	0.642504084
	40	-0.490350617	0.570955366
	60	-0.406877113	0.547105793
	80	-0.359177968	0.499406648
Segment-B	20	-0.578594036	0.646081519
	40	-0.493928053	0.544532802
	60	-0.410454549	0.524260665
	80	-0.360370446	0.505369041
Segment-C	20	-0.576209079	0.630579297
	40	-0.469154309	0.559030579
	60	-0.375684634	0.535181007
	80	-0.317985489	0.499406648
Segment-D	20	-0.572631643	0.629386819
	40	-0.429158139	0.556645622
	60	-0.329722241	0.528026135
	80	-0.269638139	0.498214169

APPENDIX-II

UNCERTAINTY ANALYSIS

Experimental uncertainty analysis by Cimbala [43] provides a method for predicting the uncertainty of a variable based on its component uncertainty. Furthermore, unless otherwise specified, each of these uncertainties has a confidence level of 95%.

In this investigation, values of pressure coefficients on each surface points are calculated from the respective multi-tube manometer readings obtained during wind tunnel test. The coefficient of lift and coefficient of drag is estimated from the surface pressure coefficients. As such, the uncertainty started from the initial measurement of manometer height and it propagates with the values of Cp, C_L and C_D. The uncertainty in Cp, C_L and C_D can be estimated if their components individual uncertainty is known.

The equation of Cp can be rewritten in terms of all its components from equation (4.2) as follows:

$$C_p = \frac{\rho_{water} \times g \times \Delta H_{Multitubemanometer}}{\frac{1}{2}\rho_{air} \times U_\alpha^2} = f(g, \rho_{water}, \rho_{air}, U_\alpha^2, \Delta H_{Multitubemanometer})$$

Due to temperature rise during the experiment, the density of air is changed. So, uncertainty of 0.019 may be assumed as the uncertainty between the air density at 30° C and 35° C). Uncertainty in the measurement of height from the multi-tube manometer may be assumed 0.0015 (as the reading vary ± 1.5 mm or 0.0015 m from the actual reading. The uncertainty in other components of Cp can be neglected. So,

$$u_{\rho_{air}} = 0.019$$

$$u_{\Delta H} = 0.0015$$

The expected uncertainty in C_P can be estimated from the following formula:

$$U_{C_p} = \pm\sqrt{(u_{\rho_{air}} \frac{\partial C_p}{\partial \rho_{air}})^2 + (u_{\Delta H} \frac{\partial C_p}{\partial \Delta H})^2} \qquad (1)$$

Let us consider the case of segment-A of wing with blended winglet at 0° AOA. There, at 20% chord on the upper surface, ΔH = -27 mm, ρ = 1.649 kg/m^3 and corresponding C_P = 0.3233. So, from equation (1),

$$\frac{\partial C_p}{\partial \rho_{air}} = -\frac{C_p}{\rho_{air}} = -\frac{0.3233}{1.1649} = -0.2776$$

$$\frac{\partial C_p}{\partial \Delta H} = \frac{C_p}{\Delta H} = \frac{0.3233}{0.027} = 11.97$$

Putting the above two values and the component uncertainties in equation (1), we get the uncertainty of C_P as:

$$U_{C_p} = \pm\sqrt{(0.019 \times -0.2776)^2 + (0.0015 \times 11.97)^2} = \pm 0.01871$$

So, the uncertainty in C_P is 1.87%. Similarly, from the respective equation of C_L and C_D, their corresponding uncertainty can be calculated considering the uncertainty of respective C_P.

Comparison of C_P distribution curve for different aspect ratios with National Airfoil Data NACA 0012 Wing [37] at 10^0AOA

Figure 6.95 shows a comparison of pressure coefficient distribution curve for different aspect ratios with national airfoil data NACA 0012 wing [37] at 10^0AOA.From the figure it is seen that all the wing models pressure coefficient values show little deviation from the available national airfoil data for NACA 0012 wing [37].At 20%C comparing the values of wing model of AR 2 and standard national airfoil data for NACA 0012 wing the calculated value of error is 1.9% at upper surface. All other values at different position also shows nearly similar value of error. Almost all the wing model with different aspect ratios show the similar characteristics as that of standard national airfoil data for NACA 0012 wing.

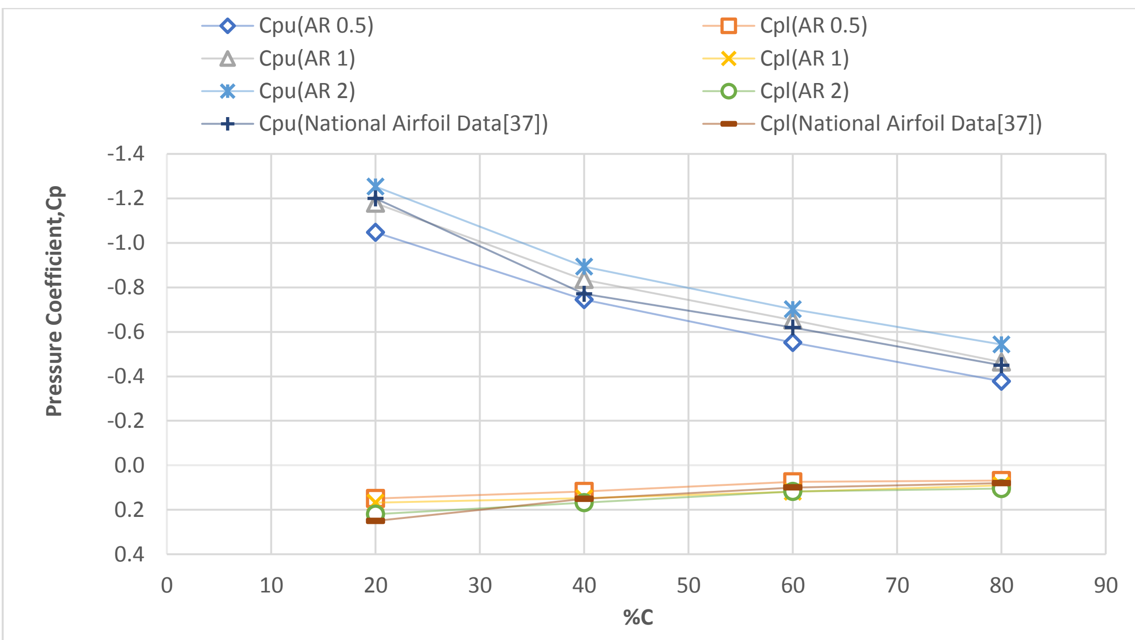

Figure 6.95: Comparison of C_P distribution for different AR's with National Airfoil Data NACA 0012[37] at 10^0AOA